



Slovak Biophysical Symposium

Book of Abstracts

**Herľany
September 12 – 15, 2004**

Editors
FABRICOVÁ Gabriela
MIŠKOVSKÝ Pavol

Organisers

Slovak Biophysical Society

&

Department of Biophysics
Faculty of Science, P. J. Šafárik University

Program Committee

CHORVÁT Dušan
HIANIK Tibor
JAKUŠ Ján
MIŠKOVSKÝ Pavol

Organising Committee

FABRICOVÁ Gabriela
HAVRILOVÁ Valéria
JANCURA Daniel
JURAŠEKOVÁ Zuzana
MIŠKOVSKÝ Pavol
STEHLÍKOVÁ MÁRIA

Chairman

MIŠKOVSKÝ Pavol

Address

Department of Biophysics
Faculty of Science
University of P. J. Šafárik
Jesenná 5
041 54 Košice

Tel:+421 55 622 19 26

Conference e-mail

sbs@seneca.science.upjs.sk

Conference web site

<http://seneca.science.upjs.sk/~sbs/>

CONTENTS**PROGRAM**

MONDAY, SEPTEMBER 13	9
TUESDAY, SEPTEMBER 14	11
WEDNESDAY, SEPTEMBER 15	12

ABSTRACTS

PLENARY LECTURES	15
LECTURES	25
MONDAY	25
TUESDAY	43
WEDNESDAY	48
POSTER SESSION	56
LIST OF PARTICIPANTS	81
AUTHOR INDEX	87



PROGRAM

7:30-8:30

BREAKFAST

8:45-9:00

OPENING

Chairmann: P. Miškovský

9:00-9:30

PLENARY LECTURE

Multispectral confocal imaging of fluorescent labels with closely overlapping emission spectra
D. CHORVÁT, JR.

9:35-9:55

LECTURE

Spectrally and spatially resolved intrinsic fluorescence of isolated rat left ventricular Cardiomyocytes
J. KIRCHNEROVÁ

10:00-10:20

LECTURE

Modulation of cellular autofluorescence by cyanide and photobleaching in relation to changes in contractility of single rat cardiomyocytes
M. CAGALINEC

10:25-10:45

COFFEE BREAK

Chairmann: M. Bánó

10:45-11:05

LECTURE

Optical characterization of polyelectrolyte microcapsules used for encapsulation of biological substances
J. PODSKOČOVÁ

11:10-11:30

LECTURE

Non-contact scanning, reverse engineering and physical modelling of human face
J. ČARNICKÝ

11:35-11:55

LECTURE

Fusion of DECARTO and cardiac imaging techniques
A. MATEAŠIK

12:00-13:00

LUNCH

Chairmann: D. Chorvát

13:00-13:20

LECTURE

Photodynamic therapy of cancer in the light of new molecular knowledge: mechanism of antitumor action of naturally occurring hydroxyquinone photosensitizers
P. MIŠKOVSKÝ

13:25-13:45

LECTURE

Serum proteins as delivery systems of photosensitizers for photodynamic therapy

D. JANCURA

13:50-14:10

LECTURE

Raman spectroscopy study of interactions of hypericin and its model compounds with serum albumins

G. FABRICIOVÁ

14:15-14:35

LECTURE

Study of interaction of hypericin with low - density lipoproteins

S. KAŠČÁKOVÁ

14:40-15:00

COFFEE BREAK

Chairmann: D. Chorvát, Jr.

15:00-15:20

LECTURE

Effect of hypericin on intracellular localization of PKC and its influence on apoptosis in U-87 MG human malignant glioma cells

S. KOČANOVÁ

15:25-15:45

LECTURE

Hypericin in photodynamic therapy of malignant tumours: In vivo experimental study

I. ČAVARGA

15:50-16:10

LECTURE

Molecular interaction model for the C1B domain of protein kinase C in the complex with its activator phorbol myristate 13-acetate in water solution and lipid bilayer

J. HRITZ

16:15-18:00

MEETING OF SLOVAK BIOPHYSICAL SOCIETY

18:00-

CONFERENCE BANQUET - GRIL PARTY

7:30-8:30

BREAKFAST

Chairmann: J. Jakuš

8:40-9:10

PLENARY LECTURE

Fractal fluctuations of resting current in isolated ventricular myocytes

P. NOVÁK

9:15-9:45

PLENARY LECTURE

Calcium signaling in cardiac muscle cells

I. ZÁHRADNÍK

9:50-10:10

LECTURE

Chloride channels of inner mitochondrial membrane

Z. VAREČKOVÁ

10:15-10:35

COFFEE BREAK

Chairmann: I. Zahradník

10:35-11:05

PLENARY LECTURE

Neuronal control of breathing, coughing and related airway reflexes: novel findings and our experience

J. JAKUŠ

11:10-11:30

LECTURE

Diabetes induced changes in biophysical properties of rat heart mitochondrial membranes

D. HABODÁSZOVÁ

11:35-11:55

LECTURE

Capillary microcirculation in rat mesentery studied by real-time videomicroscopy

P. MUSIL

12:00-13:00

LUNCH

13:00-15:00

POSTER SESSION

15:15-

EXCURSION TO VINIČKY (TOKAJ WINE REGION)

7:30-8:30

BREAKFAST

Chairmann: D. Jancura

8:40-9:10

PLENARY LECTURE

Influence of hydration on hydrostatic and hydrodynamic parameters of proteins: MC modelling

M. BÁNO

9:15-9:45

PLENARY LECTURE

Computational biophysics and bioinformatics – new possibilities and new challenges

J. ULIČNÝ

9:50-10:10

LECTURE

Frequent walking downstairs may induce coxarthrosis

M. DANIEL

10:15-10:35

COFFEE BREAK

Chairmann: J. Uličný

10:35-10:55

LECTURE

Design of the articular cartilage in the human hip joint is optimized to sustain load

M. DANIEL

11:00-11:20

LECTURE

3D visualization of mouse aorta by dual-wavelength optical coherence tomography

J. SMOLKA

11:25-11:45

LECTURE

Structural and functional changes in cytochrome c oxidase induced by high hydrostatic pressure

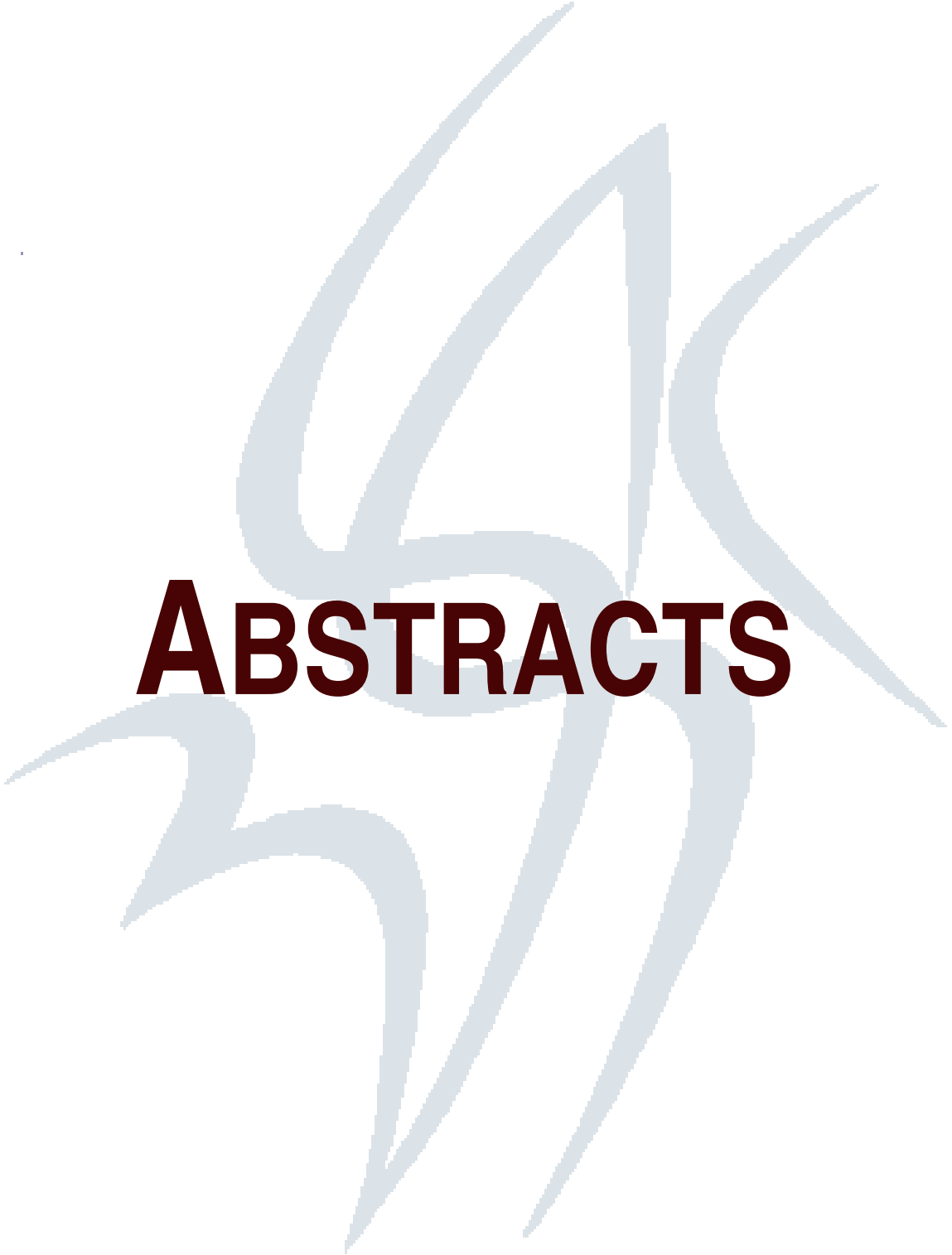
J. STANIČOVÁ

11:50-12:00

CLOSING OF SLOVAK BIOPHYSICAL SYMPOSIUM

12:00-13:00

LUNCH



ABSTRACTS

Multispectral confocal imaging of fluorescent labels with closely overlapping emission spectra

D. CHORVÁT, JR.¹, A. MATEAŠIK¹ AND A. CHORVÁTOVÁ²

¹ International Laser Centre, Ilkovičova 3, 812 19 Bratislava, Slovakia

² Research Centre, Sainte-Justine Hospital, Montreal, Canada

e-mail: dusan@ilc.sk

Introduction: Understanding complex physiological processes and structures requires simultaneous detection of variety of different parameters. Multiple fluorescence labeling is therefore essential for such simultaneous study of various structural and/or functional features directly in living cells. However, separation of several dyes with overlapping fluorescence emission spectra is usually limited only to a bandpass-filter-based detection. In order to achieve an appropriate simultaneous visualization of high number of different fluorescent dyes, we applied a new approach of their separation via spectral fingerprinting method based on linear unmixing algorithm.

Aim: Our aim is to use multi-spectral confocal fluorescence detection and application of linear unmixing algorithms for spectral separation of samples labelled with multiple fluorescent dyes with closely overlapping emission spectra.

Material and Methods: A polyelectrolyte microcapsules [1] were labelled with rhodamine 123 and fluorescein. Fluorescence emission was measured by laser scanning multi-spectral confocal microscope LSM510 META on Axiovert 200 (Zeiss) using 40x/1.2W C-Apochromat objective and 488 nm laser excitation. We used 16 channels of the META detector in the range of 509-650 nm, the spectral bandwidth of each channel was 10.7 nm.

1. Acquisition.

Lambda stacks, two or three-dimensional image stacks of raw data with X, Y and lambda (λ) coordinates, were taken from polyelectrolyte microcapsule wall (Fig. 1). Each individual image thus obtained in lambda stack represented a spectrally defined band of the emission signal (detected by one element of the META detector). Using this approach, we used two-passes of eight spectral channels detected simultaneously for each scan.

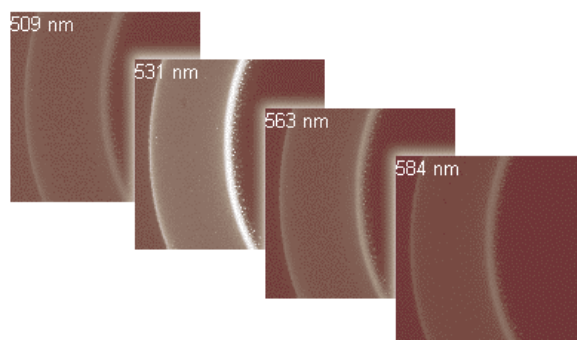


Fig. 1 Lambda stack - representative images of microcapsule wall at selected wavelengths.

2. Definition of Reference Spectra

Reference spectra, corresponding to the emission spectra of individual fluorochromes were recorded under the same conditions as present in the sample. The spectra were acquired by the acquisition of lambda stacks of two samples, each of which has been labeled with a single dye. Each sample thus provided a single reference spectrum; all together they created a spectral database (Fig. 2). Reference spectra were necessary for further spectral separation of signals from different fluorescence labels.

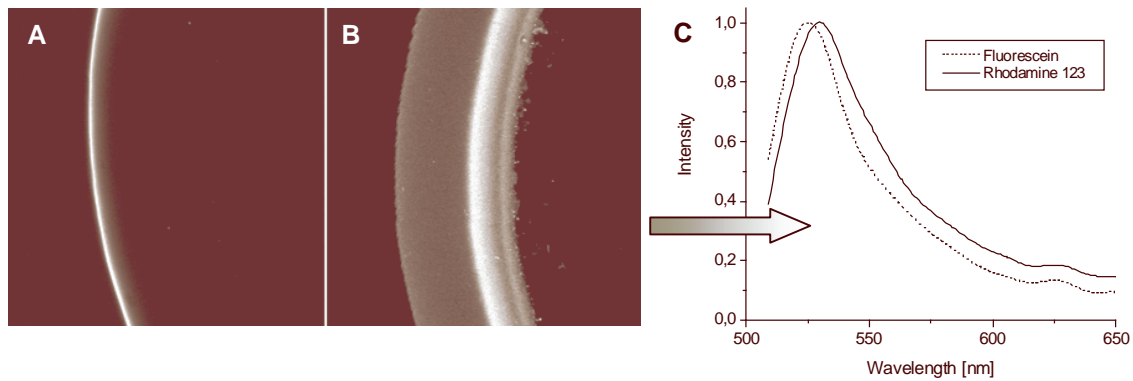


Fig. 2 Acquisition of reference spectra from a sample containing fluorescein(A) and rhodamine 123(B). C) - Spectral database with individual spectra (both lines are given in spline representation from 16 measured channels).

3. Spectral Separation

To achieve spectral separation of individual fluorescent labels, we applied the linear unmixing software function, based on algorithm [2] which computes the intensities of the emission signal of the dyes according to the equation

$$S(\lambda)_{sum} = I_1 \times S(\lambda)_1 + I_2 \times S(\lambda)_2$$

for each pixel of the lambda stacks of the sample (Fig. 3A). With the known reference spectra (Fig.2C), the equation was solved to find the intensities on separate fluorescein / rhodamine channels. The result was presented by means of a multichannel image, with each channel representing one dye (Fig.3B, 3C). Obtained spatial patterns correspond well to the microcapsule image measured by individual labelling (Fig. 2A, 2B).

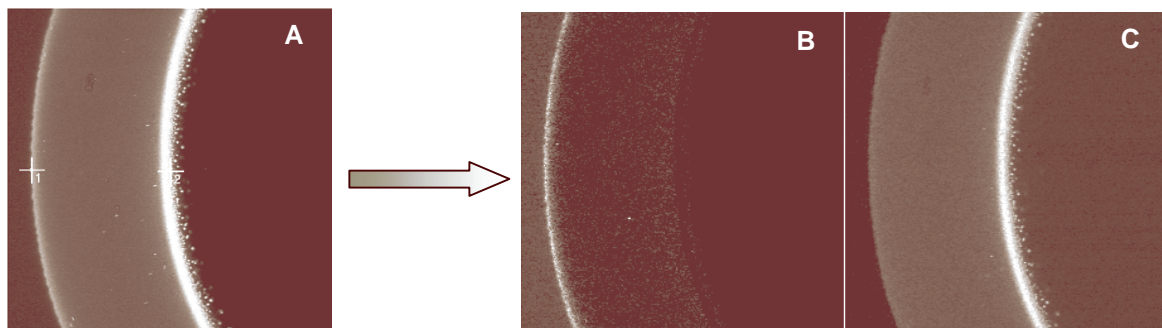


Fig. 3 Spectral unmixing of dual-labelled capsule. (A) Summary Lambda Stack image. Spectrally unmixed image of fluorescein (B) and rhodamine 123(C) content.

Conclusion: We have demonstrated successful application of the spectral fingerprinting method to separate fluorescence signals of rhodamine 123 and fluorescein, with closely overlapping spectra ($\Delta \lambda_{max}$ of fluorescence ~ 5 nm). The results constitute an important background for future study of simultaneous imaging with multiple fluorescent dyes and/or analysis of autofluorescence signal in living cells.

Acknowledgement

This work was supported by Collaborative Linkage Grant LST.CLG.979836 from NATO, and by Slovak Science and Technology Assistance Agency under the contract No. APVT-20-016002.

References

- [1] Lacík I., Briššová M., Anilkumar A.V., Powers A.C., Wang T.G. *J. Biomed. Mater. Res.* **1998**, 39, 52.
- [2] Dickinson, M.E., Bearman, G., Tilie, S., Lansford, R. and Fraser, S.E. *Biotechniques* **2001**, 31, 1272-1278.

Fractal fluctuations of resting current in isolated ventricular myocytes

P. NOVÁK AND I. ZAHRADNÍK

Institute of Molecular Physiology and Genetics, Slovak Academy of Sciences, Vlárská 5, 833 34 Bratislava, Slovakia

Analysis of long-term ECG recordings from healthy human subjects revealed irregular fluctuations in the heart rate, which exhibit correlations over wide range of time scales from seconds to several hours [1]. As a result of long-range correlations, healthy heart rate fluctuations are scale-invariant, and exhibit self-similarity – a property typical for fractal objects and processes. Clinical studies proved that self-similarity of heartbeat time series quantified by detrended fluctuation analysis (DFA) exhibit significant changes in aging and heart disease and may serve for prediction of risk of sudden cardiac death [1]. It is believed that fractal dynamics of heartbeat results from non-linear neural control of the heart. On the other hand, fractal dynamics was observed also in spontaneous beating of cultured ventricular myocytes in absence of neural control [2]. There are several evidences that even isolated cells exhibit fractal dynamics [3], however, very little is known about myocytes.

In this study we focused on the dynamics of resting current of freshly isolated rat ventricular myocytes. Resting current of myocytes was measured in the whole-cell patch-clamp configuration at the holding potential of -70mV under control conditions with blocked voltage gated Na^+ and K^+ channels, with Na^+ replaced by NMDG^+ . Digitized current records (131072 samples at 5 kHz) were analyzed using power spectral analysis and detrended fluctuation analysis. In detrended fluctuation analysis the recorded membrane current is first integrated, then divided in boxes of n samples and average fluctuation $F(n)$ over the local trend is calculated in each box [4]. The algorithm is repeated for different box sizes, to obtain relationship in the form of power-law: $F(n) = F_0 \cdot n^\beta$. Self-similarity parameter β is equal to the slope of the line in plot of $\log[F(n)]$ against $\log[n]$.

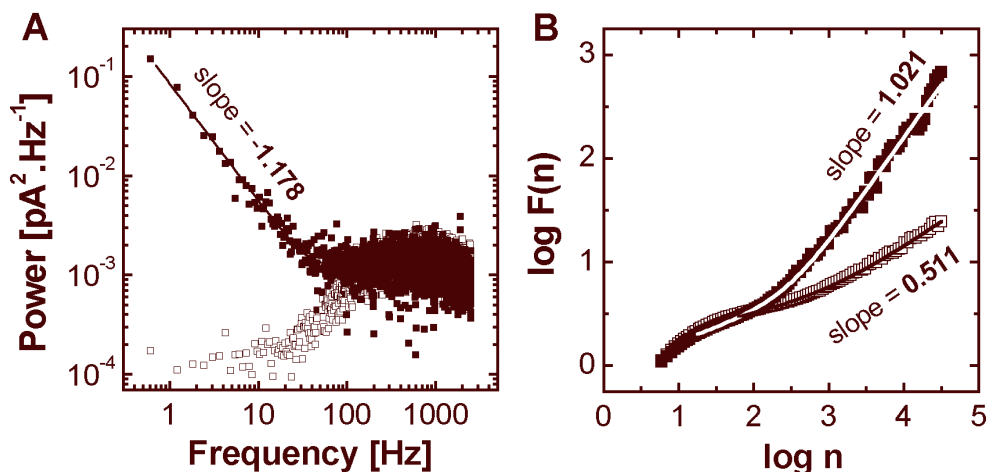


Fig 1 **A** Power spectrum of resting membrane current recorded from isolated rat ventricular myocyte with resting potential -70 mV (filled squares). The low-frequency component was fitted by power-law function: $A \cdot f^\alpha$, where $A = 0.085\text{ pA}^2$, $\alpha = -1.18$ and f is the frequency (solid line). Power spectrum of model cell consisting of passive electrical components is shown for comparison (empty squares). **B** Detrended fluctuation analysis performed on the same data files as in **A**. The self-similarity parameter β (the slope) of data from myocyte (filled squares) at high box size n was close to 1 (fractal noise), while in model cell (empty squares) it was only 0.5 (corresponding to uncorrelated white noise).

Spectral analysis of resting current recorded from isolated myocytes with high resting potential (-71.3 ± 1 mV, mean \pm S.E., $n = 6$) in control conditions revealed power-law relationship between power spectral density and frequency dominating at low frequencies as illustrated in Figure 1A. Detrended fluctuation analysis proved that the low frequency component has properties of fractal noise with the self-similarity parameter close to 1, similar to healthy human heartbeat. Fractal noise dominated at time scales longer than 60 ms. This component was not observed in currents recorded from the model cell constructed using the series resistance of $5 \text{ M}\Omega$, membrane resistance of $500 \text{ M}\Omega$ and membrane capacitance of 120 pF . As illustrated in Figure 1A, the model cell did not provide $1/f$ component in current fluctuation and at the same time its self-similarity parameter was close to 0.5 (Figure 1B). This suggests that fractal character of the current noise observed in myocytes does not originate from their passive electrical characteristics.

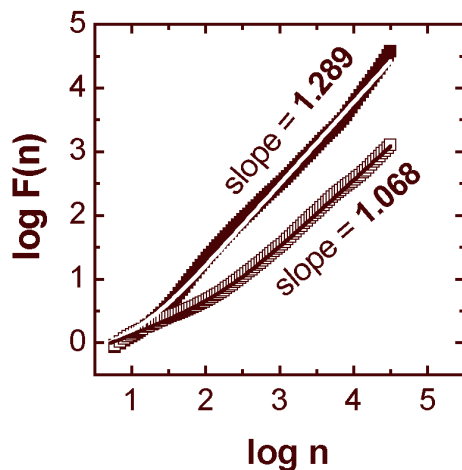


Fig. 2 The self-similarity parameter of resting current recorded from myocyte with resting potential of -15 mV in control conditions (filled squares) was higher ($\beta = 1.289$) than in normally polarized myocytes. After replacement of Na^+ by NMDG^+ (empty squares), the self-similarity parameter decreased to value close to 1 typical for normally polarized myocytes in control conditions.

We have observed that current fluctuations differed among myocytes of different metabolic state. Myocytes showing less polarized resting potential (-18.3 ± 1.7 mV, $n = 6$) displayed significantly higher values of the self-similarity parameter ($\beta \approx 1.24$, Figure 2), close to the heartbeat values reported in subjects with heart failure. Experiments performed on myocytes with extracellular solutions with Na^+ replaced by NMDG^+ (Figure 2) showed substantial decrease in the self-similarity parameter towards values observed in highly polarized myocytes. This observation can be understood as under our experimental conditions modification of the self-similarity parameter was related to influx of sodium ions. This spontaneously active sodium conductance was substantially smaller in myocytes with high membrane potential than in myocytes with low membrane potential. It means, considering trans-membrane concentration gradient of sodium ions that increased sodium conductance was also responsible for depolarization of myocytes.

We conclude that fractal dynamics of resting sodium conductance may participate in fractal behavior observed in spontaneously beating cultured ventricular myocytes or even in the whole heart.

Acknowledgement

This work was supported by the research grant from the Slovak Grant Agency Vega 2/4153/24.

References

- [1] Goldberger AL, Amaral LA, Hausdorff JM, Ivanov PC, Peng CK, Stanley HE, *Proc Natl Acad Sci* 99 (2002), 2466-2472.
- [2] Kucera JP, Heuschkel O, Renaud P, Rohr S., *Circulation Research* 86 (2000), 1140-1145.
- [3] Hoop B, Peng CK., *J Membrane Biol* 177 (2000), 177-185.
- [4] Peng CK, Buldyrev SV, Havlin S, Simons M, Stanley HE, Goldberger AL., *Phys Rev E Stat Phys Plasmas Fluids Relat Interdiscip Topics* 49 (1994), 1685-1689.

Calcium signaling in cardiac muscle cells

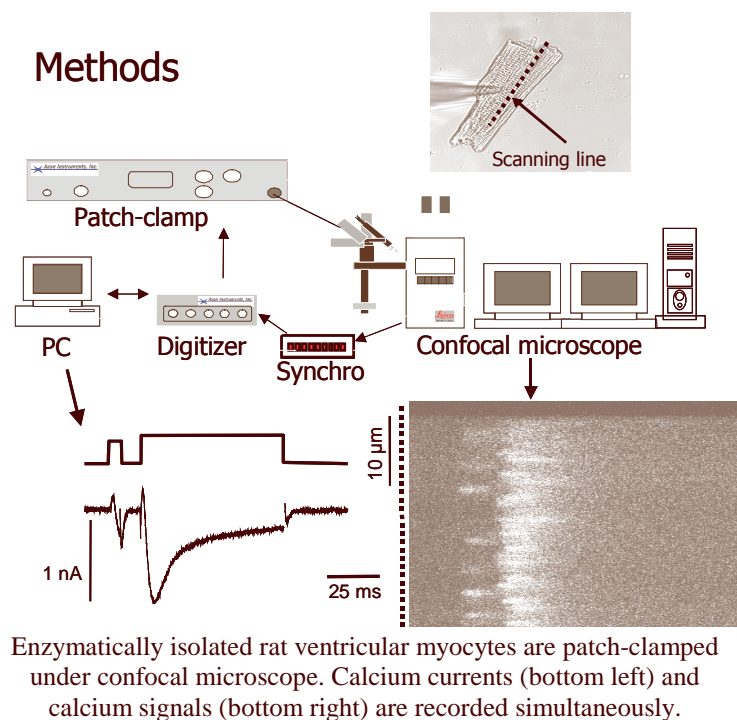
I. ZAHRADNÍK, E. POLÁKOVÁ, A. ZAHRADNÍKOVÁ, JR., AND A. ZAHRADNÍKOVÁ

Institute of Molecular Physiology and Genetics, Slovak Academy of Sciences, Vlárská 5, 833 34 Bratislava, Slovakia

Calcium signaling during excitation-contraction coupling in cardiac myocytes of mammals starts by voltage-dependent activation of plasma membrane calcium channels (DHPRs) that inject Ca^{2+} ions into the cytoplasm and activate massive Ca^{2+} release from the sarcoplasmic reticulum. Before activation of contraction, released Ca^{2+} ions inactivate DHPR channels. The calcium release-dependent inactivation dominates calcium current inactivation during normal physiological function of cardiac myocytes. Nevertheless, this aspect of calcium current kinetics is not yet well understood.

Here we studied the relationship between activation of calcium release by brief depolarizing prepulses and the consequent release-dependent inactivation (RDI) of calcium current. Calcium currents isolated from other membrane currents were measured in isolated rat ventricular myocytes using the whole-cell patch clamp technique under conditions supporting full phosphorylation of calcium channels. Calcium release was measured as spatially resolved calcium transients using confocal microscopy and the calcium indicator fluo-4. Prepulses from a holding potential of -50 mV to positive voltages, lasting 2–12 ms, induced calcium release. At the same time, they induced inactivation of the test peak I_{Ca} and decreased the extent of calcium release during the test pulse to 0 mV that commenced 10 ms after the prepulse. The extent of prepulse-induced calcium release and of I_{Ca} inactivation increased with the amplitude and duration of the prepulse. Calcium release evoked by the prepulse began shortly after the end of the prepulse, while calcium release evoked by the test pulse started around the peak of test I_{Ca} . The prepulse-evoked decrease of calcium release during the test pulse was manifested as a decrease in the number of activated release sites and as an increase in the temporal dispersion of release.

We conclude that direct measurements of spatially resolved calcium release confirm our hypothesis that the relative potencies of Ca^{2+} ions to trigger calcium release and I_{Ca} inactivation depend on the previous history of calcium current (Zahradníková et al. *Am J Physiol Cell Physiol* **286**: C330-C341, 2004). Additionally, when calcium current was partially inactivated, the decreased extent of calcium release was accompanied by a decrease in calcium release synchronization.



Supported by HHMI 55000343, and VEGA 2/4153/24.

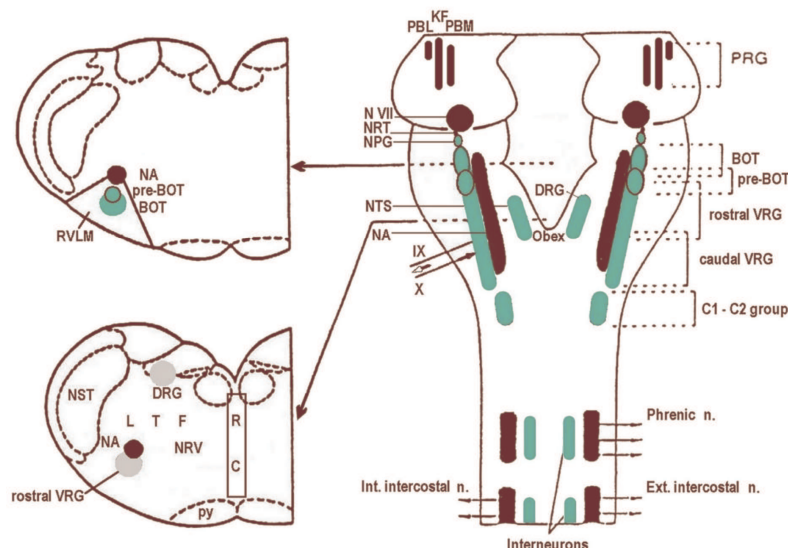
Neuronal control of breathing, coughing and related airway reflexes: novel findings and our experience

J. JAKUŠ

Institute of Medical Biophysics, Comenius University, Jessenius Faculty of Medicine, Malá Hora 4, 037 54 Slovak Republic

e-mail: jakus@jfmmed.uniba.sk

The last ten years of the past millennium known as „the decade of the brain research“ rapidly increased our knowledge in the field of respiratory neurophysiology, too. It is now more than 170 years since the bulbar centre regulating respiration was discovered. Although up-to-date, yet still not fully understood, this fascinating control system offers for further study a variety of novel experimental data about the structures and mechanisms involved in the central and peripheral nervous regulation of breathing. In contrast to that, the brainstem structures and mechanisms involved in production of the cough, sneeze and other reflexes related to breathing, are still poorly understood. Serious interest in these reflex behaviours has been renewed just in recent 10-15 years due to a better understanding of the neurones that produce the quiet breathing pattern. Since the electroneurographic analyses of Richter [1] (1982), it has been generally accepted that the underlying rhythmic pattern of respiratory neural activity consists not of two phases (i.e. inspiratory and expiratory), but of **three phases**: inspiratory, post-inspiratory (also termed stage 1 expiratory, E1), and expiratory (or stage 2 expiratory, E 2). Basically, there are three types of respiratory neurones corresponding to the three neural phases of breathing. One is the **inspiratory (I) neurone**, which fires in the inspiratory phase of the respiratory cycle, the second is the **Post-inspiratory (Post-I) neurone**, which is active during postinspiration, and the third one is the **expiratory (E) neurone**, which fires in the expiratory phase. A number of morphological and electrophysiological experiments (mostly performed in anaesthetized or decerebrate cats) have proved that the respiratory neurones are concentrated in **five main areas** of the brainstem reticular formation, the **dorsal (DRG) and ventral (VRG) respiratory groups**, the **Bötzing (BOT) and pre-Bötzing (pre-BOT) complexes** and finally the **Pontine respiratory group-PRG (Fig. 1)**. Respiratory rhythmogenesis is driven by complex interactions that reflect both **the synaptic interactions** between the synaptic inputs to brainstem neurones as well as **the intrinsic voltage-dependent membrane properties** of those neurones. It is clear, that the respiratory central pattern generator (CPG) is able to produce two characteristic, mutually coupled processes: the **generation of respiratory rhythm** and the **production of a respiratory pattern**.



Cough is the most important defensive airway reflex that protects the lungs against penetration of foreign particles and noxious substances into the lungs. In medical practice cough is a very frequent, serious and sometimes the only presented symptom of many respiratory diseases. However, the central nervous pathways and the brainstem mechanisms of cough are not satisfactorily understood. The older **transection experiments** in cats [2] showed that the neurones in **the rostral pons** may have modulatory effects on the cough reflex. Similarly it was confirmed in our experiments on non-paralyzed cats [3]. Later, we **recorded the single-unit activity** of Inspiratory and/or Expiratory neurones from medullary VRG during quiet breathing and coughing in non-paralyzed cats [4]. We documented, that all **spontaneously active respiratory neurones** (inspiratory and expiratory) recorded during quiet breathing had increased their firing rates in particular phases of coughing. The maximal frequency of single expiratory neurone in TB cough reached 132 ± 13.9 imp/s (as it was evaluated from 17 neurones in 20 tests), while the frequency of inspiratory neurone was 192.0 ± 33.8 imp/s (14 neurones in 20 tests). No recruitment of inspiratory units from VRG during inspiratory phase of cough was found. In addition, „silent“ expiratory units (with the maximal frequency 158.7 ± 16.2 imp/s), were regularly recruited during the expulsive phase of coughing. In order to localize the neurones functionally related to the cough reflex, the expression of **the immediate-early gene c-Fos**, a marker of neuronal activation, was employed in acute experiments on decerebrate, paralyzed and artificially ventilated cats [5]. Also, sophisticated recording experiments have started to be used in neurophysiological research of cough and other airway reflexes, just recently. E.g. in cough and expiration reflex the neurone spike-trains were recorded simultaneously **from multiple brainstem structures** by arrays of 50-60 individually adjustable tungsten microelectrodes [6]. Hence, it was documented: **a)** the cough motor pattern is produced by the same Bötz. complex/VRG medullary neuronal circuits which are involved also in the production of the eupnoeic pattern of breathing, **b)** the same premotor and motor (inspiratory and expiratory) neurones convey the descending drive during coughing and breathing. Our recent studies with kainic acid microinjections (kainic acid is a neurotoxin, which selectively damages the neuronal cells, sparsing the dendrites and neurites) revealed that the cough production is also affected by the medullary **midline raphe nuclei** [7], the **ventral medullary reticular nucleus** of the **lateral tegmental field** [8] (Jakuš et al. 2000), as well as the **pontine respiratory group neurones** [9]. As a result, the cough reflex (also the expiration reflex) were canceled, however the signs of the aspiration reflex still persisted. We concluded that at the level of medulla oblongata, some **multifunctional neurone circuit(s)** may exist. They might be involved in breathing, coughing, sneezing, vomiting, etc., under specific circumstances. Such circuit(s) may be located at only one level, but more probably, at **multiple levels of the brainstem** (medulla oblongata, pons Varoli, mesencephalon). Some findings being obtained during 25 years of author's experimental work on the central control of breathing, coughing and related motor behaviours will be discussed.

References

- [1] DW Richter, *J Exp Biol* 100 (1982), 93-107.
- [2] A. Dubi, *Helv Physiol Pharmacol Acta* 17 (1959), 166-174.
- [3] J.Jakuš, Z.Tomori, L. Bošelová, B. Nagyová, V. Kubinec, *Physiol Bohemoslov* 36 (1987), 329-340.
- [4] J.Jakuš, Z.Tomori, A. Stránsky, *Physiol bohemoslov*, 34 (1985), 127-136.
- [5] C.Gestreau, AL Bianchi, L.Grélot, *J Neurosci* 17 (1997) 9340-9352.
- [6] R. Shannon, DM Baekey, KF Morris, Z. Li, and BG Lindsey, *J Physiol*, 525 (2000), 207-224.
- [7] J. Jakuš, A. Stránsky, I. Poliaček, H. Baráni, L.Bošelová, *Physiol Res* 47 (1998), 203-213.
- [8] J. Jakuš, A. Stránsky, I.Poliaček, H. Baráni, L. Bošelová, *Physiol Res* 49 (2000), 387-398.
- [9] I. Poliaček I, J. Jakuš, A. Stránsky, H. Baráni, E. Halašová, Z. Tomori, *Physiol Res* 53 (2004), 155-163.

Influence of hydration on hydrostatic and hydrodynamic parameters of proteins: MC modelling

M. BÁNÓ¹, J. MAREK¹ AND M. STUPÁK²

¹ Institute of Experimental Physics, Slovak Academy of Sciences, Watsonova 47, 04353 Košice, Slovak Republic.
Fax: +421-55-678 3754; Tel: +421-55-678 2240

² Department of Biochemistry, Faculty of Science P. J. Šafárik University, Košice, Slovak Republic.
e-mail: bano@saske.sk

Hydration of macromolecules has a principal influence on function and stability of proteins, nucleic acids and other biological macromolecules. The effect of hydration is long known, nevertheless it seems, that its description was very vague. During the last decade it is intensively studied theoretically as well as experimentally with the aim to illuminate its effect to different phenomena. The theoretical description uses thermodynamic approach [1], or methods of molecular dynamics [2]. A few papers solve the problem of potential between the water and parts of macromolecules [3-5]. Principal addition of these works was a new point of view to hydration showing that hydration is a dynamic process of capture and unbending of water molecules. During this exchange process molecules of denaturants or osmolytes can replace the water molecules and so influence the stability of macromolecules in solution [1].

We have developed an effective Monte Carlo procedure [6], which simulates the interaction of the particle with water molecules as a surface adsorption process. The hydrogen bonds between the oxygen of the hydration water and charged as well as polar groups of the macromolecule are considered in the calculations. Besides that the hydrogen bonds between the free and the already bounded water molecules are taken into account. Each water molecule is assumed to create only two bonds by means of the own hydrogen protons and at the most two other bonds through outside protons, i.e. four bonds per water molecule - similarly to the pure water conditions. If a water molecule has ability to create more than four bonds at a given place, only the strongest four bonds are active.

Using the MC approach the temporal evolution of capture and unbending of water molecules on the particle surface is simulated. The macromolecules (proteins) were represented by van der Waals spheres of atoms located according to coordinates obtained from Protein Data Bank. In each time step random numbers are used to decide the place on the particle surface, where the next water molecule is attached. The length of time step is inversely proportional to the reachable, unoccupied surface (considering steric restrictions), so the probability of water molecule capture per unit time is proportional to the size of the envelope area created around the macromolecule atoms. In each time step we also check the probability that a bond water molecule leaves its place. This probability per unit time is proportional to $\exp(-\Delta U_{hb}/kT)$, where $\Delta U_{hb}=U_{hb,b}-U_{hb,out}$ is a difference between the bond energy $U_{hb,b}$ in hydrated state and the bond energy $U_{hb,out}$ immediately after leaving it, i.e. when bonds to the macromolecule are broken.

In such a way a dynamic structure is created, with binding and unbinding of water molecules. The process is stopped when equilibrium is achieved. In all the following calculations the created hydration shell is considered as an integral part of the macromolecule.

The next step of our procedure was a calculation of basic hydrostatic as well as hydrodynamic properties of hydrated macromolecule. The apparent density of molecule is calculated in manner compatible with principles presented in [7] with one difference – the solvent non-accessible volume (which includes the volume of complex macromolecule + hydrated water) was calculated also by MC procedure. This volume is calculated in two steps. In the first step are generated random localizations of bulk water molecules and is checked their steric exclusion by the molecules of above-mentioned complex. The generated position

is permitted (not excluded) if it has no intersection with the complex and then it is fixed to the second step. The effective volume of cavity in bulk water is calculated in this second step. This procedure repeats the way applied in the first step with that difference, that molecules are excluded in the case of nonzero intersection with water positions fixed in first step.

The hydrodynamic parameters were calculated in procedure based on hydrodynamic-electrostatic analogy [6, 8, 9]. According to this analogy the translation friction coefficient can be calculated as $\xi = 6\pi\eta_0 C$, where C is the electrostatic capacitance of the “hull” – a conductive closed skin, which is stretched over the fluid-accessible surface of the particle (permittivity $\varepsilon = 1$) and η_0 is viscosity of solvent (water). Then the diffusion coefficient D can be derived from the Stokes-Einstein relation $D = kT/\xi$, where T is temperature and k is Boltzman constant. The intrinsic viscosity was calculated from the equation $[\eta] = K_1 \langle \alpha \rangle + K_2 C^3$, where $\langle \alpha \rangle$ is the mean polarizability of the hull averaged through all orientations between the particle and the electrical field and constants $K_1 = 0,736494$ and $K_2 = 0,969894$ [6]. The electrostatic parameters C and $\langle \alpha \rangle$ were calculated also in MC procedure simulating distribution of charges on surfaces of atoms in the presence of external electric field (calculation of $\langle \alpha \rangle$) or without it (calculation of C).

Calculations of hydrostatic and hydrodynamic parameters of proteins (cytochrome *c*, lysozyme, myoglobin and ribonuclease A) have shown, that the results obtained for hydrated molecules are in good agreement with experimental results. Absence of hydration was simulated by potential of hydrogen bond identically equal to zero for any distances. Then we have obtained differences, which are most significant in the case of intrinsic viscosity, where the hydration causes increasing of (25.3 ÷ 28.8) % of theoretical value. Hydration causes decreasing of diffusion coefficient of (7.2 ÷ 7.7) %. Mean specific volume also decreases as a consequence of hydration – approximately of (10.7 ÷ 11.9) %. This effect is caused by higher density of hydration water then the bulk water.

Acknowledgement

This study was supported by grants from Slovak Scientific Agency No. 4068 and 3198.

References

- [1] S. N. Timasheff, *Biochemistry* 41 (2002), 13473-13482.
- [2] V. Makarov, B. M. Pettitt and M. Feig, *Acc. Chem. Res.* 35 (2002), 376-384.
- [3] F. Fabiola, R. Bertram, A. Korostelev and M. S. Chapman, *Protein Sci.* 11 (2002), 1415-1423.
- [4] S. Scheiner, T. Kar, and Y. Gu, *J. Biol. Chem.* 276,13(2001), 9832-9837.
- [5] M. S. Weiss, M. Brandl, J. Sühnel, D. Pal, and R. Hildenfeld, *TIBS* 26,9 (2001), 521-523.
- [6] M. Bánó, J. Marek and M. Stupák, *Phys. Chem. Chem. Phys.* 6 (2004), 2358-2363.
- [7] T. Chalikian, M. Totrov, R. Abagyan, and K. J. Breslauer, *J. Mol. Biol.* 260(1996), 588-603.
- [8] J. Hubbard and J. F. Douglas, *Phys. Rev. E* 475 (1993), R2983-R2986.
- [9] H.-X. Zhou, *Biophys. J.* 69, 2286-2297

Computational biophysics and bioinformatics – new possibilities and new challenges

J. ULIČNÝ

Katedra biofyziky, PF UPJŠ, Jesenná 5, Košice
e-mail: ulicny@bioflab.upjs.sk

Bioinformatics is new emergent discipline situated on boundaries between informatics, biophysics and molecular and systemic biology, taking advantage of modern high-throughput experiments for obtaining, storage and processing of unprecedented amount of data about living systems at multiple hierarchical levels. High-throughput experiments, results of which are usually commonly available using informatic tools, provide new highly competitive alternative to traditional experimental approaches.

In my contribution I will present some applications of bioinformatics approach to selected problems solved at our department within our computational group.

Spectrally and spatially resolved intrinsic fluorescence of isolated rat left ventricular cardiomyocytes

J. KIRCHNEROVÁ¹, M. CAGALINEC^{1,2}, A. CHORVÁTOVÁ³ AND D. CHORVÁT, JR.^{1,2}

¹ Faculty of Mathematics, Physics and Informatics, Comenius University, Mlynská dolina, Bratislava, Slovakia

² International Laser Centre, Ilkovičova 3, 812 19 Bratislava, Slovakia

³ Research Centre, Sainte-Justine Hospital, Montreal, Canada
e-mail: kirchnerova@ilc.sk

Introduction: Intrinsic fluorescence occurs naturally in isolated cells in the absence of fluorescent markers. One of major problems of its analytical application is that cellular autofluorescence is composed from many components originating from different molecules, only few of which have been well characterised. Visible light with wavelengths ranging around 450 nm is shown to provoke excitation of oxidised flavoproteins [1], based on the presence of tricyclic isoalloxazine ring skeleton in FAD and FMN enzyme cofactors. Mitochondrial α -lipoamide dehydrogenase (LipDH), in close redox equilibrium with the NAD-system and non-NAD-linked electron transfer flavoprotein (ETF) are reported to contribute significantly [2]. On the other hand, red-emission autofluorescence excited by green light is reported to originate from porphyrines [3].

Aim: We questioned use of multi-channel, spectrally resolved confocal fluorescence microscopy to study multi-component autofluorescence spectra in freshly isolated living cardiomyocytes.

Materials and Methods: Cardiac myocytes were isolated from left ventricle of adult male Wistar-Kyoto rats following retrograde perfusion of the heart with proteolytic enzymes [4]. Fluorescence excitation and emission spectra were recorded by spectrofluorimeter Fluorolog 3-11 (SPEX) with Xenon lamp excitation. Spectral imaging of autofluorescence was done using laser scanning confocal microscope LSM 510 Meta (Zeiss) with C-Apochromat 40x/1,2 water immersion objective in response to excitation by 458nm Ar:ion laser line (Lasos Lasertechnik).

Results and Discussion: The excitation/emission characteristics of autofluorescence obtained by steady-state spectrofluorimetry in population of isolated cardiomyocytes (Fig.1) is in accordance with previous findings that high autofluorescence signal is resulting from various components [5]. We have recognized dominant contribution of flavins (excitation/emission maxima at 450/525nm, Fig 1A), and lower-level fluorescence shoulder possibly resulting from lipofuscines/porphyrines visible in the red spectral region (exc/em. 540/630nm, Fig. 1B).

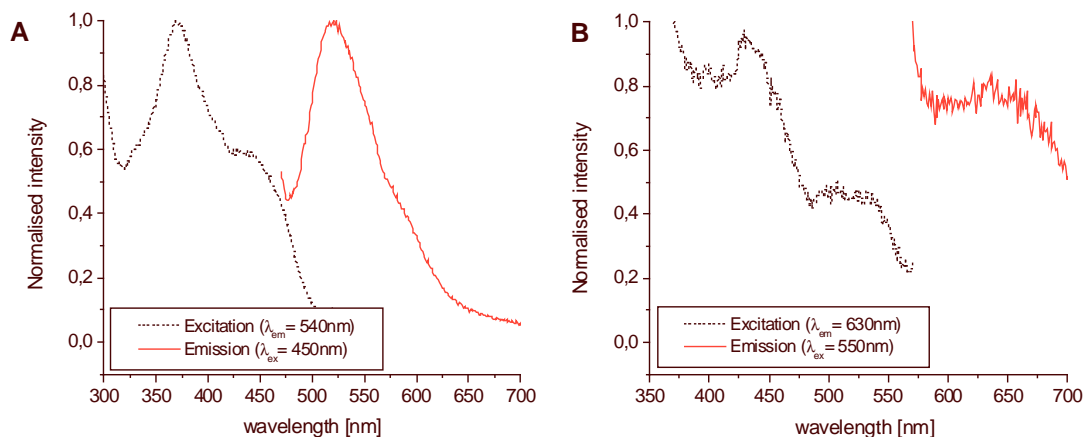


Fig. 1

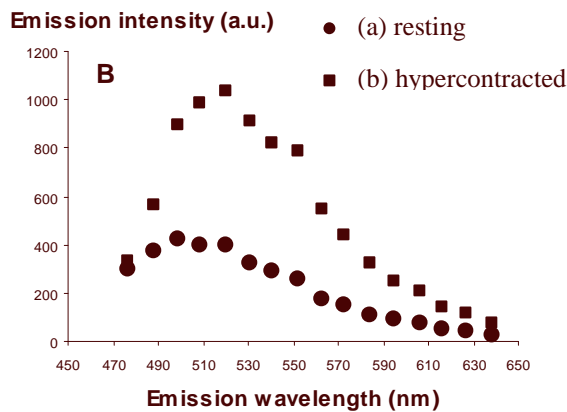
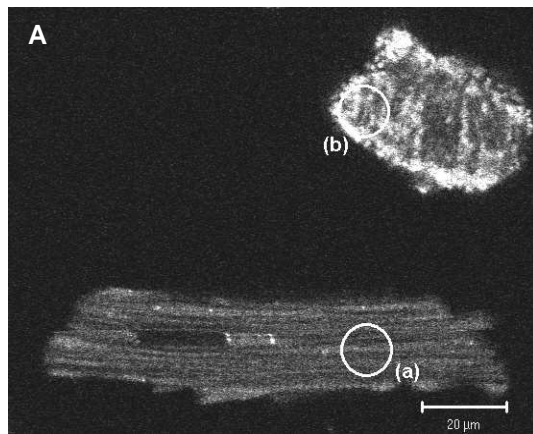


Fig. 2

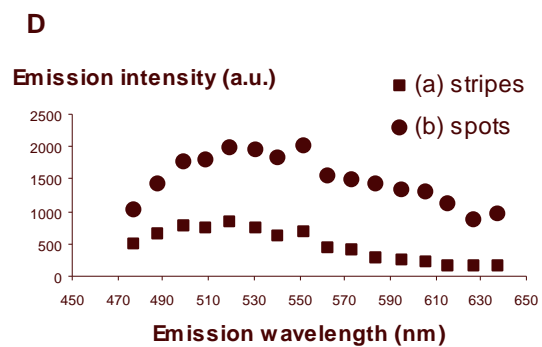
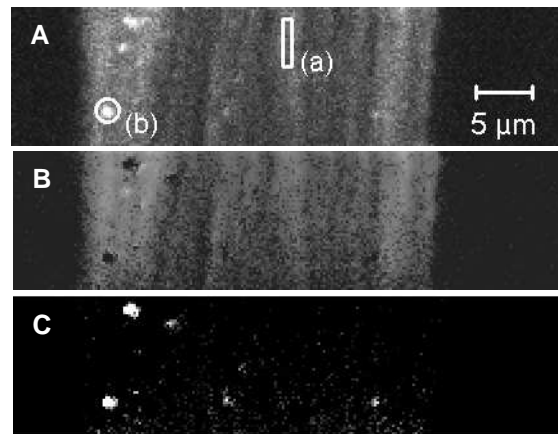


Fig. 3

In contrast to cuvette spectrofluorimetry, confocal fluorescence microscopy allows to gather data directly from living cells with the possibility to assess their metabolic state with sub-micron resolution (Fig.2). We identified spatial distribution pattern of autofluorescence consisting of blue-green stripes, green randomly distributed small spots and yellow-red larger spots that can be assigned to mitochondria (stripes), mitochondrial congregates (green spots) and porphyrin loaded lipofuscine granules (yellow spots). Different position of recorded emission peak maxima in resting (500 nm) and hypercontracted (520 nm) cells suggests changed mitochondrial redox and/or metabolic state after hypercontraction. Based on difference of emission spectra in observed mitochondrial stripes and lipofuscine spots (Fig. 3A, 3D) we have applied linear unmixing algorithm to qualitatively separate the spatial distribution of both signals (Fig. 3B, 3C).

Conclusions: Use of multispectral imaging and linear unmixing in the study of changes in autofluorescence spectra related to morphologically and possibly metabolically distinct regions in single cardiomyocytes can become a valuable tool in mapping of the changes in mitochondrial metabolic activity at a subcellular level in whole cells.

Acknowledgement

This work was supported by Collaborative Linkage Grant LST.CLG.979836 from NATO and and Slovak Grant Agency VEGA No. 1/0507/03.

References

- [1] Duchen MR, Surin A, Jacobson J, *Methods Enzymol* 2003; 361:353-389.
- [2] W. Kunz, *FEBS Lett.* 195 (1986), 92-96.
- [3] Ch. R. Kiefer, J.B. McKenney et al. *AJP* 153 (1998), 703-708.
- [4] A. Chorvatova and M. Hussain *Pflugers Arch.* 446 (2003), 442-42.
- [5] D. Chorvat, Jr., V. Bassien-Capsa et al. *Laser Physics* 14 (2004), 220-230.

Modulation of cellular autofluorescence by cyanide and photobleaching in relation to changes in contractility of single rat cardiomyocytes

M. CAGALINEC^{1,2}, J. KIRCHNEROVÁ², L. BACHÁROVÁ¹, D. CHORVÁT, JR.^{1,2} AND A. CHORVÁTOVÁ³

¹ International Laser Centre, Ilkovičova 3, 812 19 Bratislava, Slovakia

² Department of Biophysics and Chemical Physics, Faculty of Mathematics, Physics and Informatics, Comenius University, Bratislava, Slovakia

³ Research Centre of Sainte Justine Hospital, 3175 Côte Sainte Catherine, Montreal, Québec H3T1C5 Canada
e-mail: misoc@ilc.sk

Introduction: Mitochondria affects cardiomyocyte excitation-contraction coupling by modulation of cytoplasmic calcium [1] and/or regulation of ionic channels [2]. Nevertheless, the interdependence between mitochondrial metabolism and cardiomyocyte contractility is still poorly understood.

Aim: To study the changes in cell shortening and autofluorescence intensity at various wavelengths in field-stimulated rat cardiomyocytes under two conditions: 1) application of sodium cyanide, 2) the effect of autofluorescence photobleaching with 488 nm laser.

Materials and Method: Cardiomyocytes were isolated from left ventricle of adult male Wistar rats [3, 5]. Isolated myocytes were field-stimulated at 0.5 and 2 Hz and perfused with HEPES-Tyrode solution ($35 \pm 1^\circ\text{C}$), where 4 mmol/l sodium cyanide was added. Autofluorescence ($\lambda_{\text{ex}} = 458 \text{ nm}$, $\lambda_{\text{em}} = 477 \pm 5 \text{ nm}$, $509 \pm 5 \text{ nm}$ and $563 \pm 5 \text{ nm}$) and cell length (transmission, $\lambda_{\text{ex}} = 633 \text{ nm}$) were recorded with laser scanning confocal microscope LSM 510 META (ZEISS) with 40x/1.2W C-Apochromat objective.

Cell shortening was defined as a ratio of (maximal cell shortening - resting cell length) / resting cell length, expressed in percentage. Mean value of autofluorescence was recorded from whole cells and expressed in percentage of initial intensity. Data are shown as mean \pm SEM. Comparisons between group means were made using single factor ANOVA, $p < 0.05$ was considered statistically significant.

Results and Discussion: Sodium cyanide - an inhibitor of the complex IV of the mitochondria respiratory chain - induced significant decrease in autofluorescence intensity at all measured wavelengths accompanied by significant increase in the cell contractility (Fig.1). Photobleaching of autofluorescence with 488 nm laser also lead to a significant increase in cell shortening (Fig.2). Inhibition of mitochondrial oxidation in single cells and modulation of the cell autofluorescence by sodium cyanide was recently reported also in Sprague-Dawley rats [3]. In addition, presented experiment confirmed the inverse relationship between flavin autofluorescence intensity and cell shortening. However, observed changes in autofluorescence were not equal at all wavelengths: the intensity was less affected at 563nm by both effects in comparison to shorter wavelengths. This fact could be related to existence of two independent flavin-based molecules, one of which is more prone to selective bleaching.

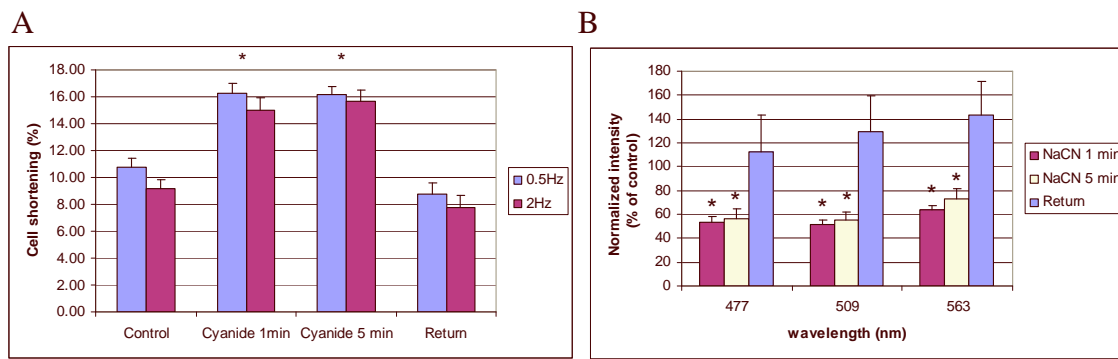


Fig. 1 Changes in cell shortening (A) N=11, and whole-cell autofluorescence intensity (B), N=6 after modulation with sodium cyanide (1min, 5min and washout).

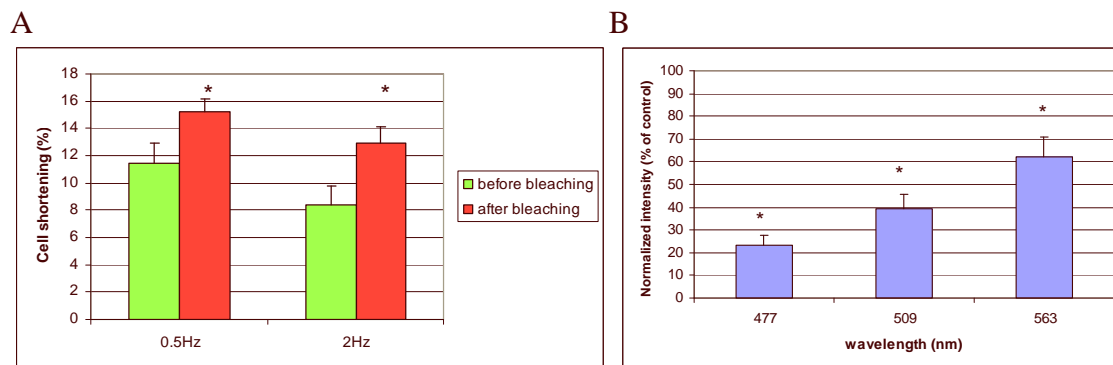


Fig. 2 Increase in cell shortening at different stimulation frequencies (A) and decrease in whole-cell autofluorescence at different wavelengths (B) after photobleaching with 488 nm laser line (N=9).

Conclusions: We observed that modifications in oxidative status of mitochondria affect cardiomyocyte contractility. We assume that this action can have implications in alterations of cellular functioning associated with mitochondrial dysfunction and/or modulations in mitochondrial energy metabolism.

Acknowledgement

This work was supported by the research grants from the Slovak Science and Technology Assistance Agency APVT No.51-013802, Collaborative Linkage Grant No.LST.CLG.979836 from NATO, and Slovak Grant Agency VEGA No. 1/0507/03.

References

- [1] R. C. Benson, R. A. Meyer, et al., *J. Histochem. Cytochem.* 27 (1979), 44-48.
- [2] J. Eng, R. M. Lynch and R. S. Balaban *Biophys. J.* 55 (1989), 621-630.
- [3] D. Chorvat Jr., V. Bassien-Capsa, et al. *Laser Phys.* 14 (2004), 1-11.
- [4] J. R. Koke, W. Wylie and M. Wills *Cytobios.* 32 (1981), 139-145.
- [5] A. Chorvatova and M. Hussain *Pflugers Arch.* 446 (2003), 442-42.

Optical characterization of polyelectrolyte microcapsules used for encapsulation of biological substances

J. PODSKOČOVÁ¹, D. CHORVÁT, JR.^{1,2}, G. KOLLÁRIKOVÁ³ AND I. LACÍK³

¹ Faculty of Mathematics Physics and Informatics, Comenius University, Bratislava, Slovakia

² International Laser Centre, Bratislava, Slovakia

³ Polymer Institute of the Slovak Academy of Sciences, Bratislava, Slovakia

Introduction: Biotechnology and biomedicine fields utilize immobilization technologies to maintain the viability and/or catalytic activity of immobilized biological material. Encapsulation in microcapsules is considered to be the most perspective immobilization technology today [1]. An encapsulation material is made of a polymer and acts as a semipermeable membrane for a controlled transport of species to and from the encapsulated biological material in a desired way. To validate the microcapsule quality it is necessary to know their geometry, surface characteristics and spatial distribution of polymers in microcapsules.

Aim: Optical characterization of polyelectrolyte microcapsules using laser scanning confocal microscopy with non-covalently bound fluorescence probes of different charge.

Material and Methods: A high uniform microcapsules based on polyanions - sodium alginate and cellulose sulfate, and polycation - poly(methylene-co-guanidine) (PMCG) [2] were produced by employing the continuous multiloop reactor [3]. Microcapsules were labelled with cationic (Rhodamine 123) and anionic (Eosin Y) fluorescent labels (dye concentration 10^{-7} mol.l⁻¹). The transmission, reflection and fluorescence emission were measured by laser scanning confocal microscope LSM510 META on Axiovert 200 (Zeiss) using 40x/1.2W C-Apochromat objective, 488nm laser line and emission bands 435-485 nm (reflection) and 535-590 nm (fluorescence). Results in tables were expressed in μm as the average value \pm the standard deviation (N=9, 3 independent scans from 3 capsules).

Results: Geometry of microcapsules was questioned using optical and confocal microscope in transmission and reflection modes (Fig.1). The capsule thickness could be best determined in reflection mode, where we observed also higher reflectance at inner capsule wall. Both parameters derived from the reflection image (L_1 , L_2 - Fig.1C) were quantitatively determined (Tab.1). Images of microcapsules labelled with Eosin Y and Rhodamine 123 signify that anionic Eosin Y was specifically bound to the outer capsule region, whereas cationic Rhodamine 123 was bound primarily at inner capsule region (Fig.2). Moreover, profile of Rhodamine 123 intensity correlate with capsule reflectance profile (Fig. 2D). Quantitative data showing mean FWHM of main peaks in fluorescence profiles are shown in Tab.1.

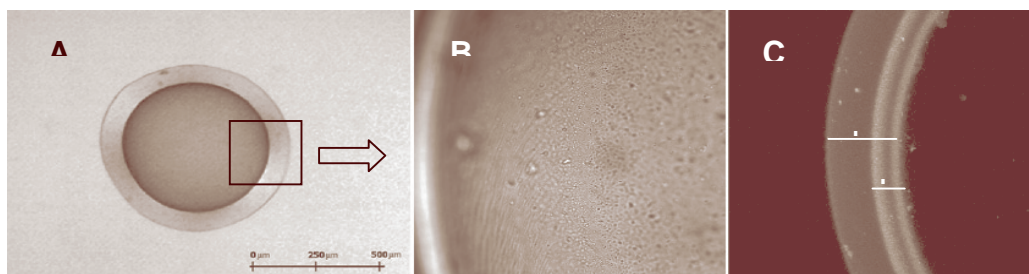


Fig. 1 Image of microcapsule observed with optical microscope (A) and laser scanning confocal microscope in transmission (B) and reflection (C) modes.

Discussion: The results indicate that inner membrane of polyelectrolyte microcapsule has negative charge, whereas outer membrane is charged mostly positively. Polymer distribution in microcapsule wall was recently studied with covalently bind fluorescent probes [4, 5], thus direct comparison with our findings is questionable. We assume, that non-covalent fluorescence labels are attracted to oppositely charged free groups in locally unfixed polymer chains.

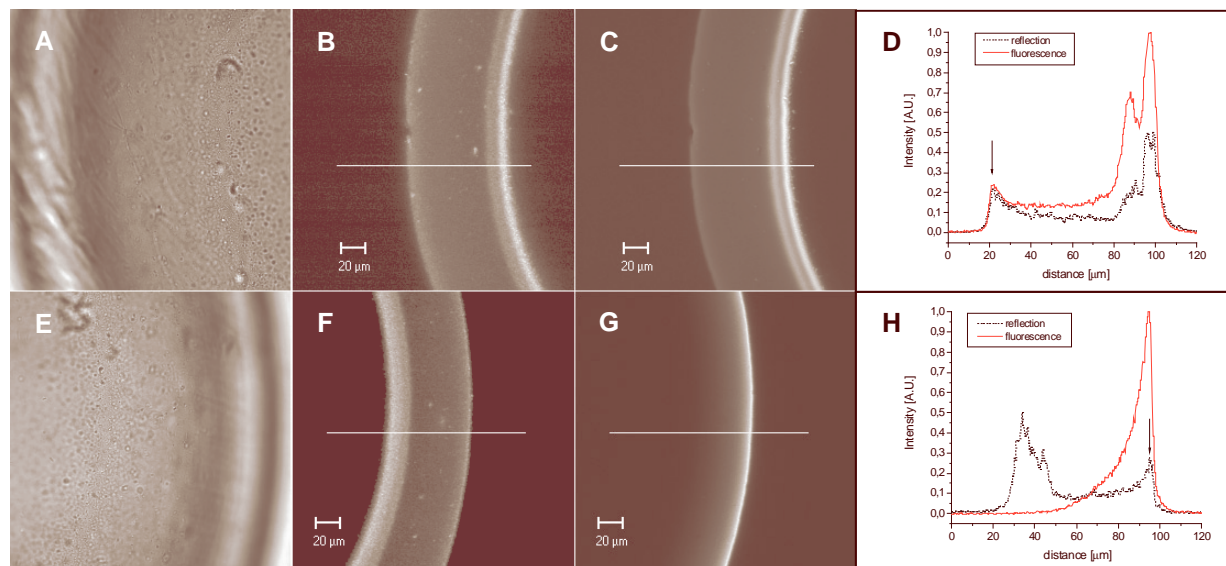


Fig. 2 Microcapsules labeled with Rhodamine 123 (A - transmission, B - reflection, C - fluorescence emission) and Eosin Y (E - transmission, F - reflection, G - fluorescence emission). D,H - Intensity profiles of fluorescence (normalised to 1.0) and reflection (normalised to 0.5), taken along the white lines indicated in B,F. Arrows - position of capsule external boundary.

Tab.1 Mean FWHM (full width in half maximum) of main peaks in fluorescence profiles of Eosin Y and Rhodamine 123, and reflection profile parameters L_1 and L_2 .

Eosin Y	Rhodamine 123	L_2	L_1
$8.4 \pm 1.7 \mu\text{m}$	$22.5 \pm 3.1 \mu\text{m}$	$26.2 \pm 3.0 \mu\text{m}$	$93.9 \pm 12.9 \mu\text{m}$

Conclusions: We observed that non-covalent fluorescent labels were specifically bound to different regions in polyelectrolyte capsules. Anionic label Eosin Y was localised preferably in outer capsule region, whereas cationic Rhodamin 123 in the inner capsule region. Fluorescence profile of Rhodamine 123 correspond to the intensity profile of reflected light, indicating possible presence of non-fluorescent precipitates with spatial distribution similar to that of Rhodamine 123.

Acknowledgement

This work was supported by Slovak Science and Technology Assistance Agency under the contract No. APVT-20-016002, and by Science Grant Agency under contract No. VEGA 1/0509/03.

References

- [1] Q. P. Hou, Y. H. Bae *Adv. Drug. Delivery. Rev.* 35, 1999, 271-287.
- [2] Lacík I., Briššová M., Anilkumar A.V., Powers A.C., Wang T.G. *J. Biomed. Mater. Res.* 1998, 39, 52.
- [3] Anilkumar A.V., Lacík, I. Wang, T.G. *Biotechnol. Bioeng.* 2001, 75, 581.
- [4] A. Lamprecht, U. F. Schäfer, C.-M. Lehr *EJPB* 49 (2000), 1-9.
- [5] Strand B. L., Morch Y. A., Espevik T., Skjak-Braek G. *Biotechnology and Bioeng.* No 4, 2002, 84, 386-394.

Non-contact scanning, reverse engineering and physical modelling of human face

J. ČARNICKÝ¹, D. CHORVÁT² AND D. CHORVÁT, JR.²

¹ Department of Biophysics, Comenius University, Mlynská Dolina, 842 48 Bratislava, Slovakia

² International Laser Centre, Ilkovičova 3, 812 19 Bratislava, Slovakia

e-mail: carnicky@ilc.sk

Introduction: Three-dimensional models of the human face are favourable in comparison to the photographs in many applications like craniofacial surgery, facial recognition, games or telecommunications [1,2,3,4]. Several approaches how to describe the feature points of the human face are known, and a large variety of methods generating the parameters and/or images representing 3-dimensional geometry of the human face have been developed [1,2,4,5]. However, since each method has its inherent limitations, none of them are in common clinical use [2,5]. In the aim of scanning the living and/or moving objects it is important the scanner to be non-invasive and fast. Thus, the main disadvantages of „classic“ contact face-measuring methods are long time of measurement and non-consistent results emerging from the deformability of the facial tissue.

Aim: The objective of this study was to develop a knowledge base for the application of non-contact optical scanning technology in the creation of a virtual human face models from a real data, following by production of their physical replicas by laser stereolithography master-moulding.

1. Scanning and reconstruction

For face scanning we used a structured-light projection based [3], non-contact optical scanning system ShapeCam (Eyetronics). The system comprised of a professional digital camera (Canon EOS D60 with 6 Mpixel CMOS detector) and a computer with the software bundles ShapeSnatcher and ShapeMatcher. The customized Canon Speedlite 550EX flash, ShapeSnatcher grid slide with a fine grain pattern, and a custom objective was used as a structured-light source. The grid structure was projected onto the object and photographed (Fig. 1). Our 3D models were created from the set of photographs taken from different directions. Snapshots were taken from the distance of 2-3 m with a Canon EF 70-200mm zoom lens. The ShapeSnatcher software (Eyetronics) was used to measure the deformations of the grid lines projected on the surface of the object, and to calculate the 3D structure of the visible part of the face. After processing the face form different points of view, and the 3D-patches were stitched together with ShapeMatcher software (Eyetronics) forming a virtual model of the face (Fig. 2.). The models were exported either to VRML or to STL data formats. Thus, in addition to the geometric characterisation of the face, we were able to extract and preserve the full geometry + texture information, forming a complete virtual model of the respective people scanned.

2. Laser stereolithography and moulding

The key idea of laser stereolithography (guided 3D structure formation based on photopolymerisation) is based on decomposition of a 3D computer model into thin cross-sectional layers, followed by physical forming of the layers and stacking them up "layer by layer". In our work we used the LS-250 (NICTL, Shatura) laser stereolithography system for creation of the master moulds of the face. The stereolithograph vat was filled with liquid photopolymer IPLIT-1 (epoxy resin) and laser induced photopolymerisation was induced by He-Cd laser LGK-30 (10 mW / 325 nm). The effective size of structures that can be grown in the vat was 250 mm x 250 mm x 250 mm, the thickness of the layer was set to 0.30mm. After polymerisation of the object on the platform we removed the support structures, and post-cured the parts in UV chamber for about 30 minutes. 3D virtual models were pre-processed

with Magics RP software (Materialise) to define precisely the conditions and way how the real physical prototypes from computer model would be manufactured by LS-250. At this step a set of supports connecting the model to the stereolithographic platform was also generated. In final step we made tangible 3D replicas of selected models by plaster moulding in a negative forms, created by stereolithography (Fig. 3).

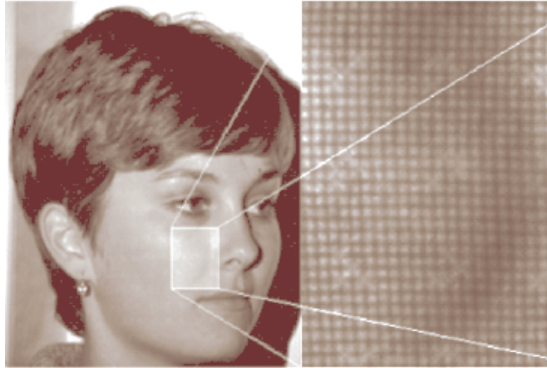


Fig. 1 Representative single snapshot with detail of the gridline mesh projection.



Fig. 2 Computer model created by stitching of scanned patches.



Fig. 3 Physical model made by plaster moulding in stereolithography negative master.

Conclusions: Creation of 3D models of the human face using structured-light scanner ShapeCam was successfully demonstrated on 18 persons. Main advantage of this method in addition to its non-contact nature was very short time needed for complete photographic documentation (several minutes). However, scanning of reflective surfaces (eyes) and hairy structures remains problematic in relation to the virtual face model creation. Quantitative description of obtained 3D models was done by measuring the distance between a subset of 22 Farkas's anthropometric landmarks [1,5].

Acknowledgement

This work was supported by Slovak APVT Grant No. APVT-20-014602.

References

- [1] J.N.Bailenson, A.C.Beall, J.Blasovich, C.Rex, *Teleoperators and Virtual Environments* (2003).
[http://www.psych.ucsb.edu/research/recvb/research_publications.htm]
- [2] N.D'Apuzzo, *Proceedings SPIE*, San Jose, California, Vol.4661, (2002).
- [3] R.Kapusta, *Proceedings CESC*, Slovakia, (2003).
- [4] P. Kubíni, *Proceedings CESC*, Slovakia, (2003).
- [5] R. Enciso, A. Shaw, U. Neumann, J. Mah, *Progress in Biomedical Optics and Imaging*, Vol. 4, No. 20, (2003).

Fusion of DECARTO and cardiac imaging techniques

A. MATEAŠIK¹, L. BACHÁROVÁ¹ AND M. ZIMÁNYI^{2,1}

¹ International Laser Centre, Bratislava, Slovakia

² Faculty of Mathematics, Physics and Informatics, Comenius University, Bratislava, Slovakia
e-mail: mateasik@ilc.sk

Intoduction: Modern imaging methods, such as echocardiography, computerised topography, scintigraphy and magnetic resonance imaging allow visualization of anatomical structures and functional characteristics of the heart from various aspects. In compartative studies, these methods are used mostly as reference methods, as a basis for the evaluation of the validity of ECG results. However, imaging methods provide basically different and complementary information in relation to electrocardiography: the information on structural and functional characteristics of the heart as of the source of cardiac electric field, and the changes of these characteristics can, but need not necessarily change the electrogenetic properties of myocardium.

In current clinical practice, the most frequently used system is the standard 12-lead electrocardiogram, which contains a historic set of scalar electrocardiograms. In spite of accumulated clinical experience during the last century, the information provided by the 12-lead ECG is redundant, and the underlying conceptual model for clinical interpretation is complicated. On other side, physically corrected orthogonal lead systems (the most frequently used Frank and McFee-Parungao systems) are based on biophysical principles to rationalize the electrocardiographic information. The advantage of physically corrected orthogonal leads is the biophysically based approach and a relatively small volume of input data, allowing meaningful mathematical treatment. An important prerequisite for optimal evaluation is their proper mathematical treatment and adequate graphic representation.

Aim: The aim of this contribution was to present a technique allowing the visual comparison and superposition of orthogonal electrocardiograms and MRI and, SPECT cardiac images respectively to study the relations of functional and structural characteristics of the heart.

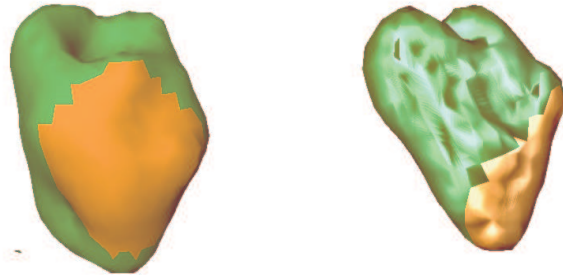
Material and Methods: A method for the topographic presentation of orthogonal electrocardiograms of ventricular depolarization – DECARTO (dipolar electrocardio-topography) was used [1], allowing transformation of orthogonal ECG by means of a mathematical model to represent the equivalent generator of the cardiac electric field as a uniform double layer with time varying size and location on a spherical surface approximating the ventricular wall. Ventricular activation is represented by time series of maps of activated points, or in the form of summary maps of cardiac excitation on the spherical image surface, so-called decartograms [1, 2].

To obtain real structural and functional characteristics of heart, two imaging methods were used in study. Magnetic resonance imaging (MRI) provides data on structural characteristics of the myocardial tissue. Single photon emission tomography (SPECT) provides data on functional characteristics of heart using a perfusion of myocardium by thalium-201. The acquired imaging data from both methods were presented as volumetric data in form of several equidistant cross-sections of the imaged heart.

All data processing and visualization algorithms were developed and tested using IRIS Explorer modular programming environment (Numerical Algorithm Group, UK) for Windows 2000 operating system (Microsoft, USA). Examples of clinical data such as ECG, MRI and SPECT images were used from clinical databases.

Results: The developed set of methods allowed interactive visualization and statistical comparison of orthogonal electrocardiograms in the form of decartograms and MRI and SPECT images of the heart. The visualization of the DECARTO data could be obtained in the form of summary maps of cardiac excitation in the discrete time points or as fluent animations of activated areas on the projection surface during QRS interval (Figure 1).

Fig. 1 Fusion or superimposition of DECARTO data onto 3D reconstructed surface of the heart left ventricle from a set of cross-sectional cardiac SPECT images (A) and MRI images (B). The geometrical surface was extracted from volume data using marching cubes algorithm.



Discussion and conclusion: 12 lead electrocardiography, as well as vectorcardiographic presentation of electrocardiograms has limited possibilities for a direct comparison and merging information between ECG and results of other imaging techniques. However the utilization of mathematical models allows a presentation of electrocardiogram in a way comparable with other imaging techniques. The combined information of these two clinically available methods allows studying the relationship between electrogenesis and the myocardial blood flow and metabolism. The superposition of SPECT and DECARTO data gives the opportunity to study both diagnostic and prognostic importance of agreements and disagreements of findings of both methods. In addition the fusion of these diverse types of information about the heart activity may potentially increase the diagnostic power of both methods.

Acknowledgement

This work was supported by Slovak Science Grant Agency under contract VEGA 1/0509/03.

References

- [1] Titomir, L.I., Ruttkay-Nedecky, I.: Chronotopocardiography: A new method for presentation of orthogonal electrocardiograms and vectorcardiograms. *Int J Bio-Medical Computing*, 1987, 20: 275–282.
- [2] Bacharova L, Chorvat D, Mateasik A, Titomir L.I.: Topographic presentation of the dipolar content of cardiac electric field. *Medizinische Technik* 44, 1999, 156–158.

Photodynamic therapy of cancer in the light of new molecular knowledge: mechanism of antitumor action of naturally occurring hydroxyquinone photosensitizers

P. MIŠKOVSKÝ

ILC, Ilkovičova 3, 812 19 Bratislava, Slovakia

Department of Biophysics, P. J. Šafárik University, Jesenná 5, 041 54 Košice, Slovakia

The main objective of our research is to transfer the knowledge obtained at the molecular and cellular level to the animal models, with the long-term aim to capitalize the knowledge in terms of optimal therapeutic action.

The lecture will describe in general way, the interactions of selected hydroxyquinone photodynamic active agents (hypericin, calphostin, hypocrellin A and their derivatives) with relevant transport (serum albumins and lipoproteins) and regulatory proteins (protein kinase C (PKC)). In addition a study of signaling pathways description influenced by photodynamic action of photosensitizers will be discussed in both *in vitro* and *in vivo* levels.

Acknowledgement

This work was supported by the Slovak Science and Technology Assistance Agency under the contract No. APVT-20-022202, grant No. 1/9040/02 of the Scientific Grant Agency of the Ministry of Education of Slovak Republic.

Serum proteins as delivery systems of photosensitizers for photodynamic therapy

D. JANCURA, G. FABRICIOVÁ, S. KAŠČÁKOVÁ AND P. MIŠKOVSKÝ

Department of Biophysics, P. J. Šafárik University, Jesenná 5, 041 54 Košice, Slovakia
e-mail: dano@seneca.science.upjs.sk

It is well known, that serum proteins are predominantly responsible for the transport of photosensitizers to various areas of the body including tumor tissues [1-4]. The binding of the photosensitizer to the several of serum proteins is mainly governed by the degree of hydrophilicity/lipophilicity of the photosensitizer. In general, moderately hydrophobic photosensitizers are transported in the bloodstream preferentially by albumin, whereas highly hydrophobic photosensitizers interact mainly with lipoproteins, especially with low density lipoproteins (LDL) [4-5]. The knowledge about the mode of transport and mechanism of cellular uptake of drugs is very important from the point of view of selectivity of tumor targeting, because it is very well known, that a low selectivity represents an important drawback in many types of cancer therapies. The understanding of the mode of interaction between several photosensitizers and serum albumin and LDL can lead to enhanced intracellular accumulation of the drug with improved targeting and consequently to more effective photodynamic action to tumor tissues.

Acknowledgement

This work was supported by the Slovak Science and Technology Assistance Agency under the contract No. APVT-20-022202, grant No. 1/9040/02 of the Scientific Grant Agency of the Ministry of Education of Slovak Republic.

References

- [1] W.M. Sharman, J.E. van Lier, and C.M. Allen C.M, *Advanced Drug Delivery Review* **56** (2004), 53-76.
- [2] M.R. Hamblin, E.L. Newman and E. Alleman, *J.Photochem.Photobiol.* **23** (1994), 3-8.
- [3] I. Rosenthal, *Photochem. Photobiol.* **53** (1991), 859-887.
- [4] E. Reddi, *Journal of Photochemistry and Photobiology B: Biology* **37** (1997), 189-195.
- [5] M. Kongsghaug, *Int. J. Biochem.* **24** (1992), 1239-1265.

Raman spectroscopy study of interactions of hypericin and its model compounds with serum albumins

G. FABRICIOVÁ¹, S. SÁNCHEZ-CORTÉS², D. JANCURA¹, J. V. GARCÍA-RAMOS² AND P. MIŠKOVSKÝ^{1,3}

¹ Department of Biophysics, P. J. Šafárik University, Jesenná 5, 04 154 Košice, Slovakia

² Instituto de Estructura de la Materia, CSIC, Serrano 121, 28006 Madrid, Spain

³ International Laser Centrum, Ilkovičova 3, Bratislava, Slovakia
e-mail: fabgabi@yahoo.com

Hypericin (Hyp) is a natural polycyclic aromatic hydroxyquinone which displays antiproliferative and cytotoxic activity on tumour cells as well as virucidal activity against several types of viruses. For these reasons, Hyp is a very promising agent for application in photodynamic therapy (PDT) of cancer and virus diseases.

Serum albumins are the most abundant plasma proteins and contribute significantly to many transport and regulatory processes. The proteins bind a wide variety of substrates such as metals, fatty acids, amino acids, hormones and an impressive spectrum of drugs [1]. Serum albumins are known to contain two specialized drug binding sites located in subdomains IIA and IIIA [1, 2].

The binding of Hyp to HSA helps to overcome difficulties in solubilization and dispersion of Hyp in aqueous physiological solution. The HSA-Hyp interaction results in dissociation into the monomeric form of Hyp, which is aggregated in the aqueous phase. The monomeric form of Hyp appears to be crucial for its biological action [3]. Considering the role of serum albumins in the pharmacokinetics, the detail knowledge of specific interaction of hypericin and its model compounds (emodin, quinizarin, danthron) with serum albumins can contribute to the optimal therapeutical protocol for application of Hyp in PDT.

In this study, by means of surface enhanced Raman (SERS), resonance Raman spectroscopy (RRS), time resolved techniques and molecular modeling, we have identified the Hyp binding site as being in the IIA subdomain of human serum albumin (HSA), where Hyp is rigidly bound very close to Trp214 [4,5]. Further we have shown that the presence of fatty acids in HSA changes the structure of emodin, quinizarin, danthron in the complex with HSA [6, 7]. The primary binding site of these molecules in defatted albumin is located in the subdomain IIIA, where the monoanionic or dianionic form of these molecules interacts via electrostatic interaction with the basic amino acid residues existing at the entrance of the cavity. In the presence of fatty acids, the ligands are displaced from subdomain IIIA to subdomain IIA, where their neutral form interacts with the hydrophobic cavity of this subdomain.

Acknowledgement

This work was supported by the Slovak Science and Technology Assistance Agency under the contract No. APVT-20-022202, grant No. 1/9040/02 of the Scientific Grant Agency of the Ministry of Education of Slovak Republic.

References

- [1] T. Peters, *Adv. Protein Chem.* 37 (1985), 161-245.
- [2] U. Kragh-Hansen, *Mol. Pharmacol.* 34 (1988), 160-171.
- [3] G. Lavie, Y. Mazur, D. Lavie, A. M Prince, D. Pascual, L. Liebes, B. Levin and D. Meruelo, *Transfusion* 35 (1995), 392-400.
- [4] P. Miškovský, D. Jancura, S. Sánchez-Cortés, E. Kočišová and L. Chinsky, *J. Am. Chem. Soc.* 120/25 (1998), 6374-6379.
- [5] K. Das, A. V. Smirnov, J. Wen, P. Miškovský and J. W. Petrich, *Photochem. Photobiol.* 69/6 (1999), 633-645.
- [6] G. Fabriciová, S. Sánchez-Cortés, J. V. García-Ramos and P. Miškovský, *Biopolymers* 74 (2004), 125-130.
- [7] G. Fabriciová, S. Sánchez-Cortés, J.V.García-Ramos and P. Miškovský, *J.Raman Spectr.* 35 (2004) 384-389.

Study of interaction of hypericin with low - density lipoproteins

S. KAŠČÁKOVÁ^{1,2}, M. REFREGIERS², F. SUREAU³, D. JANCURA¹, J.-C. MAURIZOT² AND P. MIŠKOVSKÝ^{1,4}

¹ Department of Biophysics, P.J. Safarik University, Kosice, Slovakia

² Centre de Biophysique Moléculaire, CNRS UPR4301, Orléans, France

³ LPBC, Université Pierre et Marie Curie, 75005 Paris, France

⁴ International Laser Cener, Laboratory of Applied Biophysics and Pharmacology, Bratislava, Slovakia

Low-density lipoproteins (LDL) play a key role in the delivery of hydrophobic photosensitizers to tumor cells in photodynamic therapy (PDT), because of the enhanced expression of specific LDL receptors in many types of transformed cells as compared with non-transformed cells [1,2]. One of the most promising photosensitizer in PDT appears to be hypericin. Hypericin is a natural polycyclic aromatic dione which displays antiproliferative and cytotoxic effect on tumor cells as well as virucidal activity against several type of viruses [3,4]. Thus, the study of interaction of hypericin with LDL could provide useful information about mechanism and physiological relevance of hypericin application in PDT and photodiagnosis.

Our results show that hypericin interacts nonspecifically with LDL, probably with lipid fraction of LDL. The molar ratio of hypericin binding to non-oxidized LDL (25:1) is the same as in the case of interaction with mildly oxidized LDL. We have also demonstrated that photoactivated hypericin can oxidize LDL in the light dose - dependent manner and that oxidation of LDL by hypericin depends on the ratio binding of hypericin with LDL : the maximum of the oxidation of LDL by hypericin using the concrete dose of the light is at the molar ratio hypericin : LDL , 25:1, which is in the good agreement with the saturation binding curve of hypericin with LDL. This observation is very important from the point of view of possible hypericin using in PDT. It is known that oxidized LDL is a potent inducer of apoptosis in vascular cells [5] and also plays an important role in the development of atherosclerosis [6]. Both of these facts should be considered when hypericin is applied as photodynamic agent in PDT.

Acknowledgement

This work was supported by the Slovak Science and Technology Assistance Agency under the contract No. APVT-20-022202, grant No. 1/9040/02 of the Scientific Grant Agency of the Ministry of Education of Slovak Republic. This work is part of the „co-tutelle“ doctoral thesis of S.K. supported by the French Government.

References

- [1] Polo, L., Valduga, G., Jori, G. and Reddi, E. (2002) *Inter. J. Biochem. & Cell Biol.* 34, 10-23.
- [2] Bonneau, S., Vever-Bizet, C., Morliere, P., Maziere, J.C. and Brault, D. *Biophysical Journal* 83 (2002), 3470-3481.
- [3] Miskovsky, P. *Current Drug Targets* 3 (2002), 55-84.
- [4] Agostinis, P., Vantieghe, A., Merlevede, W. and de Witte P. *Inter. J. Biochem. & Cell Biol.* 34 (2002), 221-241.
- [5] Lee, T.S. and Chau, L.Y. *AJP-Cell Physiology* 280 (2001), 709-718.
- [6] Alcouffe, J., Caspar-Bauguil, s., Salvayre, R., Thomsen, M. and Benoist, H. *J.Lipid Research* 40 (1999), 1200-1209.

Effect of hypericin on intracellular localization of PKC and its influence on apoptosis in U-87 MG human malignant glioma cells

S. KOČANOVÁ¹, J. HRITZ¹, A. MATEAŠIK², A. PETRUFOVÁ¹, M. ŠARIŠSKÝ³, J. PLÁŠEK⁴, L. MIROSSAY³ AND P. MIŠKOVSKÝ^{1,2}

¹ Department of Biophysics, University of P. J. Safarik, Jesenna 5, 04154 Kosice, Slovak Republic

² International Laser Center, Ilkovicova 3, 812 19 Bratislava

³ Department of Pharmacology, University of P. J. Safarik, SNP 1, 040 01 Kosice, Slovak Republic

⁴ Institute of Physics, Charles University, Ke Karlovu 5, 121 16 Prague, Czech Republic

Hypericin (Hyp), a natural polycyclic aromatic dione displays antiproliferative and cytotoxic effect on tumor cells as well as virucidal activity against several type of viruses [1, 2]. Protein kinase C (PKC) is a key enzyme involved in cellular differentiation and proliferation, and a potetial target for anticancer and antiviral chemotherapeutic drugs [3]. Some authors have supported an important role of the PKC in regulating glioma growth and have led to the speculation that PKC inhibitors may be used in the therapy of patients with malignant gliomas. Studies of specific PKC inhibitors have shown that Hyp specifically inhibits PKC and it was proposed that Hyp interacts with the regulatory domain of PKC like its structural analog calphostin C [4].

In our results we propose that anticancer activity of naturally occurring photosensitizer hypericin in human malignant U-87 MG glioma cell line is related to its ability to inhibit the PKC. Fluorescence imaging technique was used to monitor intracellular localization of PKC in U-87 MG human glioma cells, which reflects its activity. It is shown that PKC localization is influenced by Hyp and this influence is different from that observed for phorbol-12-myristate-13-acetate (PMA) which acts as PKC activator (Fig.1).

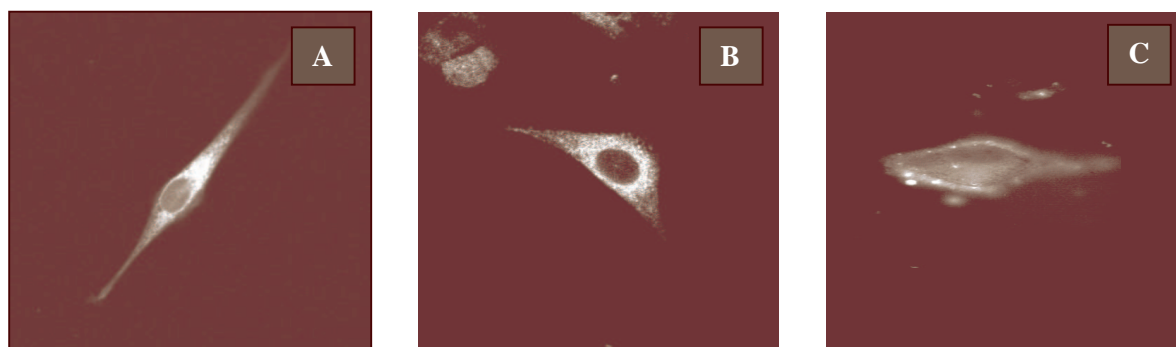


Fig. 1

Sub-cellular localization of PKC (stained by fim-1 fluorescence probe) in U-87 MG cells in response of treatment with Hyp. 488 nm excitation was used and the emission was detected in the region of 500-550 nm. Cells shown are representative of ten independent experiments.

- A) fluorescence of fim-1 in control cells (the image was taken after 30 min of incubation with fim-1-AM)
- B) fluorescence of fim-1 in cells treated with 1 μ M hypericin (the image was taken after 30 min of incubation with Hyp)
- C) fluorescence of fim-1 in cells treated with 1 μ M PMA (the image was taken after 30 min of incubation with PMA)

Fluorescence binding experiments were realized to determine the binding constant of Hyp to PKC which is compared with that already determined for PMA. Finally, molecular modeling

was used to compare structural models of the PKC/Hyp (C1Bdomain/Hyp) and the PKC/PMA (C1Bdomain/PMA) complexes. The influence of Hyp and/or PMA on PKC translocation in U-87 MG cells, co-localization fluorescence pattern of Hyp and PKC (stained by fim-1), the higher binding affinity of Hyp to PKC in comparison with PMA, as well as the binding mode of Hyp to C1B domain of PKC suggested by molecular modeling support the idea, that Hyp competitively binds the same binding site in PKC as PMA.

Flow-cytometry experiments have shown that Hyp phototoxicity induces both, apoptosis and necrosis in a concentration- and light dose-dependent way. Relation between PKC inhibition and induction of apoptosis by Hyp in U-87 MG glioma cells is discussed but some authors show that light dependent inhibition of protein kinase C seems to be caused by Hyp complexation with the regulatory domain of PKC [4, 5] where a covalent bond is formed after illumination and consequently an irreversible, site specific, oxidative modification of PKC is observed [6].

Acknowledgement

This work was supported by the Slovak Science and Technology Assistance Agency under the contract No. APVT-20-022202, grant No. 1/9040/02 of the Scientific Grant Agency of the Ministry of Education of Slovak Republic.

References

- [1] Agostinis, P., Vantieghem, A., Merlevede, W. and de Witte, P. A. M. (2001) *IJBCB* **1200**, 1–21
- [2] Miskovsky, P. (2002) *Current Drug Targets*, **3**, 55-84
- [3] Hofmann, J. (2004) *Cur. Cancer Drug Targets*, **4**, 125-146
- [4] Takahashi, I., Nakanishi, S., Kobayashi, E., Nakano, H., Suzuki, K. and Tamaoki, T. (1989) *Biochem. Biophys. Res. Comm.* **165**, 1207-1212
- [5] Diwu, Z., Zimmermann, T., Meyer, T. and Lown, J.W. (1994) *Biochem. Pharmacol.* **47**, 373-385
- [6] Gopalakrishna, R., Chen, Z. and Gundimeda, U. (1993) *Free Radical Biol. & Med.* **15**, 530

Hypericin in photodynamic therapy of malignant tumours: In vivo experimental study

I. ČAVARGA², P. BREZÁNI¹, P. FEDOROČKO³, P. MIŠKOVSKÝ^{3,4}, N. BOBROV¹, F. LONGAUER¹, S. RYBÁROVÁ¹, L. MIROSSAY¹ AND J. ŠTUBŇA¹

¹Faculty of Medicine, P. J. Šafárik University, Košice, Slovakia

²Medical School Hospital of L.Pasteur, Košice, Slovakia

³Faculty of Sciences, P. J. Šafárik University Košice, Slovakia

⁴International Laser Center, Bratislava, Slovakia

The *in vivo* antitumour activity of the natural photosensitizer hypericin was evaluated. C3H/DiSn mice inoculated with fibrosarcoma G5:1:13 cells were intraperitoneally or intratumourally injected with hypericin (5 mg/kg) and 2 hours later the mice were locally irradiated with laser light (488nm, 150 mW/cm², 180 J/cm²) when the tumour reached volume of 40-80 mm³ (~17 days after inoculation). Tumours treated with hypericin alone as well as those irradiated with laser light alone have similar growth rates and none of these tumours regressed spontaneously. The mean tumour volume in hypericin-PDT treated groups was significantly lower in comparison to that found in the control group 3 – 5 weeks after the therapy. A higher proportion of animals with tumour volume less than 5-fold of the initial volume has been observed in both hypericin-PDT treated groups. Complete response to PDT has been observed for 44.4% of the animals with intraperitoneally administered hypericin and for 33.3% of the animals with intratumourally administered hypericin. Complete remission occurred in treated lesions with 3 mm or less in height. Hypericin-PDT significantly increased survival. However, no statistically significant difference in survival rate of animals has been found between the intratumoural and the intraperitoneal schedule of administration of hypericin.

Our experimental model showed that fractionated administration of hypericin can produce a better therapeutic response than single administration. When the tumour reached a volume of 40-80 mm³ the mice were intraperitoneally injected with hypericin, either in a single dose (5 mg/kg; 1 hour or 6 hours before laser irradiation) or two fractionated doses (2.5 mg/kg; 6 hours and 1 hour before irradiation with laser light; 532nm, 70 mW/cm², 168 J/cm²).

All tumours in control groups treated with hypericin alone as well as those irradiated with laser light alone had similar growth rates and none of these tumours regressed spontaneously. Complete remission of tumour in PDT-treated groups was similar (14-17% single dose vs 33% fractionated dose), but the fractionated schedule of hypericin dosing was found to be more efficient than the single dose, measured by survival assay (p<0.05).

Acknowledgement

This work was supported by Science and Technology Assistance Agency under the contract No. APVT-20-022202, grant No. 1/9211/02 of the Scientific Grant Agency of the Ministry of Education of the Slovak Republic and Institutional grant of Faculty of Medicine, P. J. Šafárik University No. 8/2002/IG4.

Molecular interaction model for the C1B domain of protein kinase C in the complex with its activator phorbol myristate 13-acetate in water solution and lipid bilayer

J. HRITZ¹, J. ULIČNÝ¹, A. LAAKSONEN², D. JANCURA¹ AND P. MIŠKOVSKÝ^{1,3}

¹ Department of Biophysics, P. J. Šafárik University, Jesenná 5, 041 54 Košice, Slovakia

² Division of Physical Chemistry, Arrhenius Laboratory, Stockholm University, SE-106 91 Stockholm, Sweden

³ International Laser Centre, Ilkovičova 3, 812 19 Bratislava, Slovakia
e-mail: hritz@seneca.science.upjs.sk

Detailed molecular models of free C1B domain of PKC and the C1B domain with its activator phorbol-12-myristate-13-acetate (PMA) in water solution and in the presence of dipalmitoylphosphatidylcholine (DPPC) bilayer are presented (Figure 1).

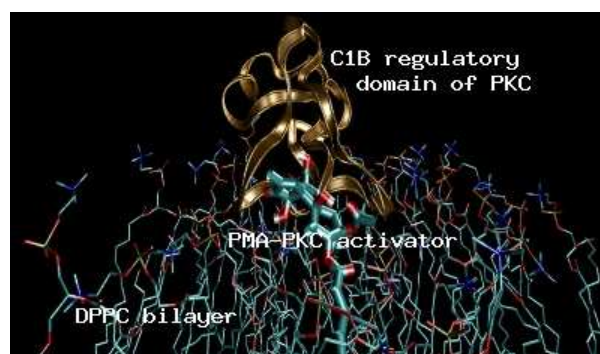


Fig. 1 Schematic figure of molecular model of C1B domain of PKC with its activator phorbol-12-myristate-13-acetate (PMA) in the presence of dipalmitoylphosphatidylcholine (DPPC) bilayer

Analysis of molecular dynamics of free C1B domain shows critical hydrogen bonds constraining the length of the loops forming the diacylglycerols/phorbol esters binding site and indicate an important role of Gln27 for the geometry of the binding site. According to the structural model of the C1B/PMA complex, PMA interacts with C1B domain by hydrophobic interactions with Pro11, Tyr22 and by three persistent hydrogen bonds between the C3 carbonyl group of PMA and Gly23 and between the C20 hydroxyl group of PMA and Leu21, Thr12 residues of C1B domain. The carbonyl oxygen of the ester group at C13 atom of PMA forms a weaker hydrogen bond with the hydroxyl group of Ser10 of C1B domain. The resulting binding mode is very similar to the binding mode observed in the X-ray structure, except of the involvement of the C4 hydroxyl group, which is of minor significance for the binding in our model. Although the C9 hydroxyl group of PMA does not directly interact with C1B domain, it is involved in the interaction with the DPPC bilayer. Two preferential mutual orientations of the C1B/PMA complex towards the DPPC bilayer were observed in our molecular modelling study. These two orientations were found by new effective approach to sample the potential energy surface of the PMA/C1B/DPPC bilayer system in water solution. The involvement of DPPC in the C1B/PMA complex only slightly changed the binding mode between regulatory domain of PKC and phorbol ester. The presented new mechanistic model of PKC-ligand interaction can serve as suitable base for the ligand binding study and rational drug design for this important class of regulatory proteins.

Acknowledgement

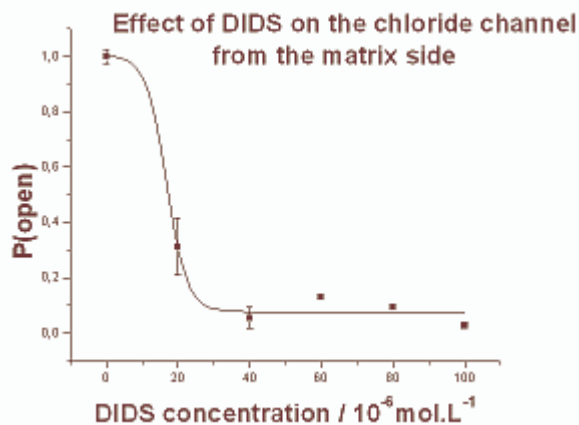
This work was supported by the Slovak Science and Technology Assistance Agency under the contract No. APVT-20-022202, grant No. 1/9040/02 of the Scientific Grant Agency of the Ministry of Education of Slovak Republic and by the Swedish Institute (a stay at Stockholm University for J.H.)

Chloride channels of inner mitochondrial membrane

Z. VAREČKOVÁ, V. KOMÍNKOVÁ AND K. ONDRIŠ

Laboratory of intracellular ion channels, Institut of Molecular Physiology and Genetics, SAS, Vlárská 5, 83334 Bratislava, Slovakia
e-mail: zufanka@yahoo.fr

There are many ion channels and other transporters in the inner mitochondrial membrane. Our attention has been focused on the chloride channels of this membrane. We used the BLM method to explore these channels. Inside-out vesicles of the inner mitochondrial membrane isolated from rat heart (Wistar, 200 – 250 g, males) have been incorporated into artificial planar lipid membrane. Single-channel activities have been measured in asymmetrical KCl solution – 250 mmol.L⁻¹ on the matrix side and 50 mmol.L⁻¹ on the cytosolic side of the membrane. The conductance of measured channels was in range of 50 to 150 picosiemens (pS). We have been interested in the effect of ATP on chloride channels. The effect was not uniform for every channel. We have observed one channel which was completely blocked by 1 mmol.L⁻¹ ATP from matrix side. Similar effect has been observed on 50 pS chloride channel from inner membrane of yeast mitochondria [1]. In other experiments, there was either no change in open probability but a slightly faster gating kinetics of the channel or there was a small decrease of the open probability. Further, we have studied the effect of DIDS (4,4'-diisothiocyanatostilbene-2,2'-disulfonic acid). DIDS is a non-specific blocker of many chloride channels. It was added to the matrix side up to 100 μmol.L⁻¹ concentration when the channels have been completely blocked. K_D for DIDS is around 20 μmol.L⁻¹. The DIDS blockage was irreversible.



On the figure we can see the course of open probability change when concentration of DIDS increased on the matrix side. Open probability in the absence of DIDS was set as 100 %.

Based on our results, we can exclude some types of known chloride channels - the mitochondrial „centum picosiemens“ channels because of the lack of DIDS blockage or the inner membrane anion channels IMAC because of the inhibition by divalent ions. We suppose that some of the observed channels are the uncoupling proteins – UCP channels, though it is not certain because of the diverse effect of ATP in our experiments. Chloride currents has been measured and described previously on UCP isolated from brown adipose tissue mitochondria [2].

Acknowledgement

This work was supported by the research grant from the Slovak Grant Agency APVT-51- 013802 and VEGA 2-3001-23.

References

- [1] C. Ballarin and M. C. Sorgato, *J.Biol.Chem.* 270 (1995), 19262-19268.
- [2] S-G. Huang and M. Klingenberg, *Biochemistry* 35 (1996), 16806-16814.

Diabetes induced changes in biophysical properties of rat heart mitochondrial membranes

D. HABODÁSZOVÁ¹, I. WACZULÍKOVÁ¹, A. MATEAŠIK², M. FERKO³, M. ZVARÍK¹, L. ŠIKUROVÁ¹ AND A. ZIEGELHÖFFER³

¹ Department of Biophysics, FMFI Comenius University, Mlynská dolina, 842 48 Bratislava, Slovakia

² ILC, Ilkovičova 3, 841 04 Bratislava, Slovakia

³ Institute for Heart Research, Slovak Academy of Sciences, Dúbravská cesta 9, 840 05 Bratislava, Slovakia

Introduction: It is generally believed, that the diabetic heart (DH) is exposed to action of reactive oxygen species (ROS) and non-enzymatic glycation. The damage consequently appearing involves perturbances in function of the electron-oxygen chain and oxidative phosphorylation. Our previous results indicated significantly ($p < 0.01-0.001$) decreased state 3 and 4 oxygen consumptions, respiratory control indexes and phosphorylation rates. However, also an unchanged ADP/O ratio. These point to negative modulation of the kinetics, but not the efficacy of ATP production that is also supported by an elevation of mitochondrial Mg-ATPase activity [1]. Structural modification of DH mitochondria involves augmentation of mitochondrial contact site formation with consequent facilitation of transmembrane delivery of energy to the cytoplasm [2]. The aim of the present study is to elucidate the biophysical base for the above functional and structural remodeling of mitochondria.

Methods: Diabetes mellitus was induced to adult male Wistar rats by a single dose of streptozotocin (55 mg/kg, i.p.). After 8 days the hearts were excised and mitochondria were isolated and diluted at the concentration of 0.25 g/ml in buffer solution. Mitochondria were investigated in two weight-matched groups of 7 healthy and 7 diabetic rats. Membrane fluidity was assessed by the degree of fluorescence anisotropy using the fluorescent dye 1,6-diphenyl-1,3,5-hexatriene (DPH) at final concentration of 1 $\mu\text{mol/l}$, measured by a luminescence spectrometer (LS 45, Perkin Elmer). Confocal microscopy (LSM 510 META, Zeiss) was used for characterization of changes in mitochondrial potential before and after applied KCl solution (40 – 320 mmol/l). Mitochondrial potential was monitored by 5,5',6,6'-tetrachloro-1,1',3,3'-tetraethylbenzimidazolylcarbocyanine iodide (JC-1), a cationic dye forming green-fluorescent monomers at low concentrations or at low membrane potentials and red-fluorescent J-aggregates at higher concentrations or higher membrane potentials [3].

Results and discussion: DH mitochondria exhibited significantly decreased fluorescence anisotropy values (increased membrane fluidity) when compared to healthy controls (Fig. 1).

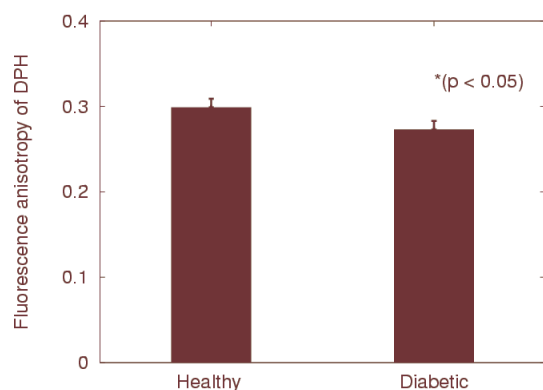


Fig. 1 Fluorescence anisotropy of DPH in heart mitochondrial membrane.

The spectrally resolved image series (lambda stack) of mitochondrial sample was acquired in spectral region from 520 nm to 690 nm with 10.5 nm step. Fluorescent spectrum record was taken from the lambda stack and exhibited two maxima at 680 nm and 570 nm. These maxima correspond to J-aggregates and monomers of the cationic dye JC-1, respectively. The ratio of J-aggregates to monomers was considered as a measure of the mitochondrial membrane potential. In comparison with controls, DH mitochondria exhibited relatively reduced red-fluorescence indicating descendent membrane potential (Fig. 2, 3).

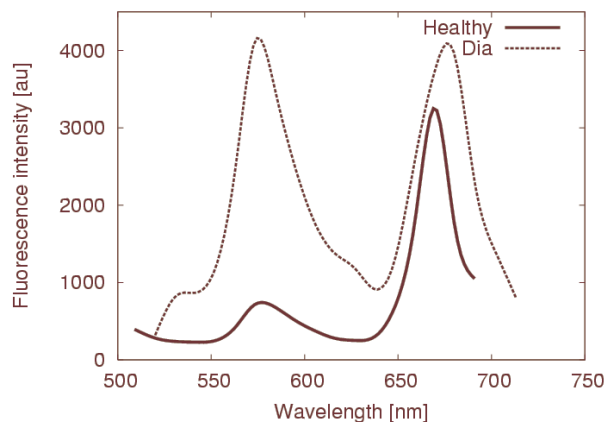


Fig. 2 Fluorescent spectra of JC-1 in heart mitochondrial membrane.

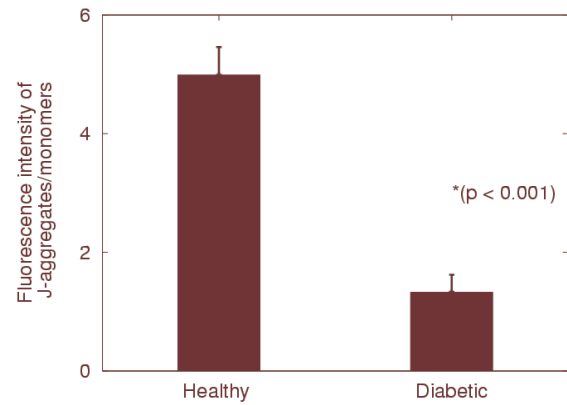


Fig. 3 Heart mitochondrial membrane potential changes.

The difference between fluorescence anisotropy of DPH in mitochondrial membrane and membrane potential explained 46 % of total data variability by linear regression analysis, which revealed that a significant ($p < 0.05$, correlation coefficient is 0.67) association exists between decrease in membrane anisotropy and decrease in membrane potential.

Capability of the inner mitochondrial membrane to keep its membrane potential was tested by application of increasing concentrations of KCl.

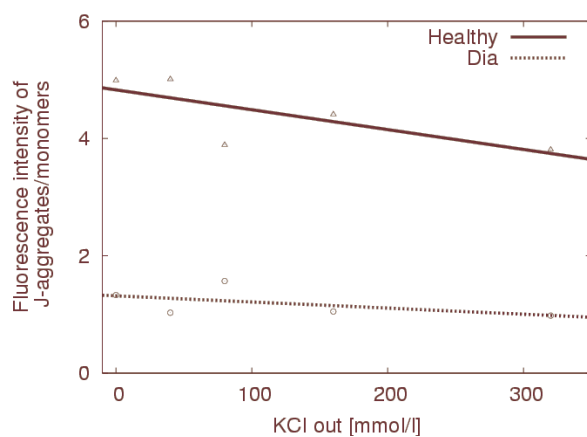


Fig. 4 Effect of KCl on the heart mitochondrial membrane potential.

Fig. 4 demonstrates that the capability of the heart mitochondria from diabetic animals to maintain membrane potential was out-staying that of the healthy ones.

Conclusions:

1) In comparison with control mitochondria, DH mitochondria exhibit tendency for creation of lower membrane potential.

2) The capability of DH mitochondria to keep membrane potential was out-staying the capability of healthy heart mitochondria. Hence, the membrane potential of the DH mitochondria may be more stable.

3) Regression analysis revealed a good correlation between increase in membrane fluidity and the decrease in membrane potential of the DH mitochondria.

Acknowledgement

This work was supported by the research grant from the Slovak Grant Agency Vega No. 1/0253/03 and APVT-51-013802.

References

- [1] A. Ziegelhöffer, T. Ravingerova, I. Waczulikova, M. Barancik, M. Ferko, A. Gvozdjakova, M. Strniskova, P. Simoncikova, *J. Mol. Cell Cardiol.* 36 (2004), 772-773.
- [2] B. Ziegelhöffer-Mihalovicova, I. Waczulikova, L. Sikurova, J. Styk, J. Carsky and A. Ziegelhöffer, *Mol. Cell Biochem* 249 (2003), 175-182.
- [3] S. T. Simley, M. Reers, C. Mottola- Hartshorn, M. Lin, A. Chen, I. W. Smith, G. D. Steele and L. B. Chen, *Proc. Natl. Acad. Sci. USA* 88 (1991), 3671-3675.

Capillary microcirculation in rat mesentery studied by real-time videomicroscopy

P. MUSIL¹, J. KYSELOVIČ² AND L. BACHÁROVÁ³

¹Faculty of mathematics, physics and informatics, Comenius University Bratislava,

²Pharmaceutical faculty, Comenius University Bratislava

³International Laser Center, Bratislava.

e-mail: musil@ilc.sk

Introduction: Microscopy of capillaries (capillaroscopy) is a noninvasive optical technique allowing direct visualization and measurement of structural and functional parameters in capillaries. The presented system is using a real-time conversion of the analog videosegment from microscope to digital form, and consequently allowing its off-line processing on PC. It can be used for dynamic measurement of red blood cell velocity (RBCV), as well as for determination of nutritional blood flow in capillaries of human body (in the nail fold of the fingers and toes and on the dorsa of the hands and feet) and the capillaries of animals (in mesentery [1][2], or in brain cortex [3], or muscle [4]).

AIM: The aim of this study was to adapt a capillaroscope originally used for humans, for examination of experimental animals, to process the obtained image for further analysis and to demonstrate its possibilities in groups of normotensive rats (Wistar) and spontaneous hypertensive rats (SHR).

Material and Methods: The *in vivo* capillaroscopy (made in the Centre of analysis of substances, Joint Strock Company, Moscow 2001- CAS) was performed on 3 groups of rats: Wistar 12 weeks old, body weight 280 ± 16.43 g (Wistar, $n = 6$), SHR 12 weeks old, body weight 245 ± 10.80 g (SHR12, $n = 4$), SHR 20 weeks old, body weight 325 ± 13.23 g (SHR20, $n = 3$). Under total anaesthesia the mesentery was carefully placed into a glass chamber with 0.9% NaCl solution (with temperature 37°C). The chamber was placed on the stage of the reflex microscope for *in vivo* microscopy recording.

The picture were transformed directly to the video card in a PC using CCD camera (JVC TK-C1380), then digitalized and optimized by the mean of the video correction card. The RBCV and morphometric parameters (diameter and length of capillary where RBCV was measured) were calculated using frame-to-frame analysis (Fig. 1). Mann-Whitney U test was used to compare data in 3 groups of experimental animals and $p < 0.05$ was considered significant.

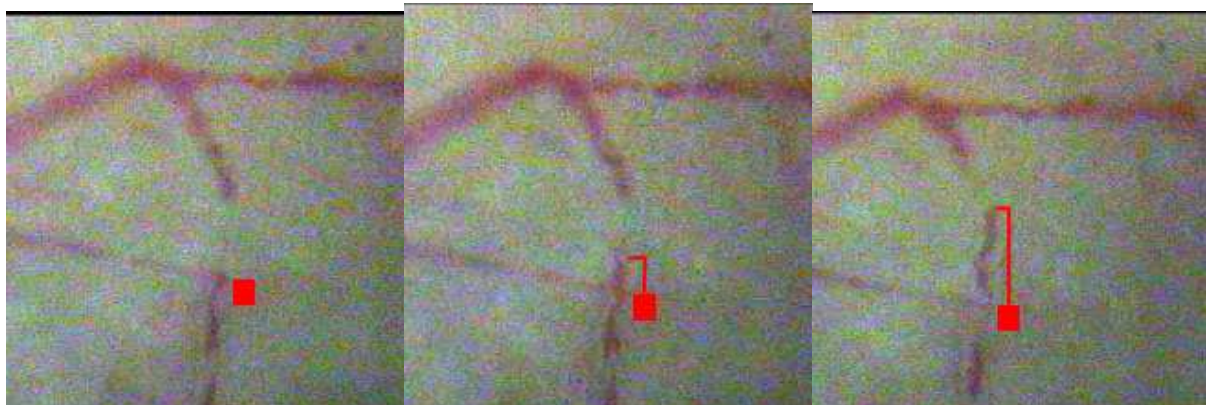


Fig. 1 Three frames of a rat capillary, where the displacement of red blood cell is seen. Rectangular sign represents the starting position of red blood cell.

Results: There were no significant differences in morphometric parameters among study groups (Tab. 1). The capillary blood flow velocity in the venous limb of capillaries was the highest in SHR20, the difference between SHR20 and control Wistar ($302,60 \pm 44,19 \mu\text{m/s}$ and $260,70 \pm 39,57 \mu\text{m/s}$, respectively) was statistically significant ($p < 0.01$). A comparison of SHR20 and SHR12 group ($302,60 \pm 44,19 \mu\text{m/s}$ and $294,75 \pm 53,65 \mu\text{m/s}$, respectively) and comparison of Wistar and SHR12 revealed no significant differences in RBCV (Fig. 2). The highest RBCV in SHR20 group can be probably associated with higher blood pressure and hyperkinetic circulation in SHR rats.

Tab. 1 Morphometric parameters in groups under study.

Wistar: healthy normotensive control, SHR12: spontaneous hypertensive rats 12 weeks old, SHR20: spontaneously hypertensive rats 20 weeks old. Both parameters are in μm .

	Diameter	Length
Wistar	8.33 ± 5.16	92.17 ± 30.69
SHR12	6.13 ± 4.22	81.88 ± 25.38
SHR20	6.8 ± 5.45	89.7 ± 20.24

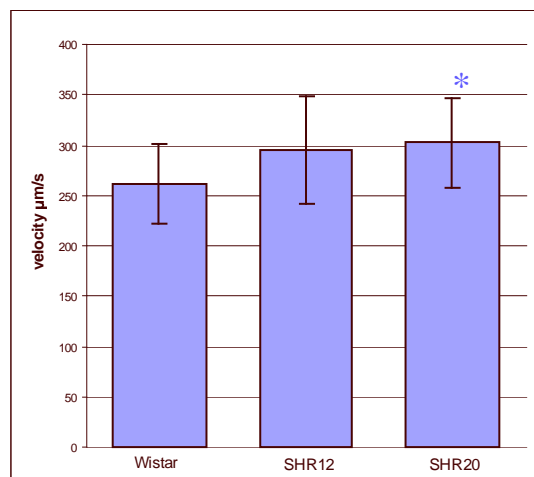


Fig. 2 Red blood cell velocity in groups under study.

*: $p < 0.01$ (Wistar vs. SHR20). Data are presented as mean and standard deviation.

Conclusion: We showed that the capillaroscope (CAS) could be used after adaptation for *in vivo* real-time measurement of red blood cell velocity and selected morphometric parameters in rats. The frame-to-frame method allowed to quantify morphometric parameters of selected microvessels.

Acknowledgement

This work was supported by the research grant from the VEGA 1/0507/03.

References

- [1] H. H. Dietrich, *Microvascular Research*, 1989, 38:125-135.
- [2] A. Bollinger, Butti P, Barras JP, *Vasa*, 1974, 3(2):163-164.
- [3] Villringer A, Them A, Lindauer U, Einhaupl K, Dirnagl U., *Circ Res*. 1994, 75(1):55-62.
- [4] Sugii Y, Nishio S, Okamoto K., *Ann N Y Acad Sci*. 2002, 972:331-6.

Frequent walking downstairs may induce coxarthrosis

M. DANIEL^{1,2}, V. KRALJ-IGLIČ³, A. IGLIČ⁴ AND S. KONVIČKOVÁ¹

¹ Laboratory of Biomechanics, Department of Mechanics, Faculty of Mechanical Engineering, Czech Technical University in Prague, Technická 4, 166 07 Prague, Czech Republic

² Department of Applied Mechanics and Mechatronics, Faculty of Mechanical Engineering, Technical University of Košice, Letná 9, 042 00 Košice, Slovakia

³ Institute of Biophysics, Medical Faculty, Lipičeva 2 and Department of Orthopaedic Surgery, University Medical Center, Zaloška 9, SI-1000Ljubljana, Slovenia

⁴ Laboratory of Applied Physics, Faculty of Electrical Engineering, Tržaška 25, SI-1000 Ljubljana, Slovenia
e-mail: daniel@biomed.fsid.cvut.sk

The values of the the resultant hip force \mathbf{R} , obtained from the measurements with special instrumented endoprosthesis, were used to calculate the stress distribution in the adult human hip joint during walking, walking upstairs and walking downstairs. Walking upstairs increases the peak contact stress p_{max}/W_B by 9% in comparison to its value in normal walking while in walking downstairs, p_{max}/W_B is 24% higher than in normal walking. Increased contact stress in walking downstairs can be associated with higher incidence of osteoarthritis observed in patients which climb stairs frequently.

Long-term excessive loading of the hip joint is considered to be important in the development of osteoarthritis which is a frequent source of functional disability and pain in elderly. Recent epidemiologic studies suggest that people which climb stairs frequently are at higher risk for the development of osteoarthritis [1]. Large differences in size and direction of the hip joint resultant force (\mathbf{R}) with respect to the situation during level walking were observed in staircase walking.

However, from the clinical point of view, it is well known that the clinical status of the hip is affected not only by the factors which influence the hip joint resultant force but also by other factors which change the contact stress distribution in the hip joint, i.e. by the radius of the femoral head or by the lateral coverage of the femoral head. It is widely accepted that increased contact stress in the hip may increase development of coxarthrosis [2].

We have used a three-dimensional mathematical model that has been developed for calculating the contact stress distribution in the hip joint if the resultant hip force is known [2]. Force \mathbf{R} was taken from the measurements by implanted instrumented endoprosthesis by prof. Bergmann [3]. We have tested the hypothesis, whether staircase walking yields an increased hip contact stress.

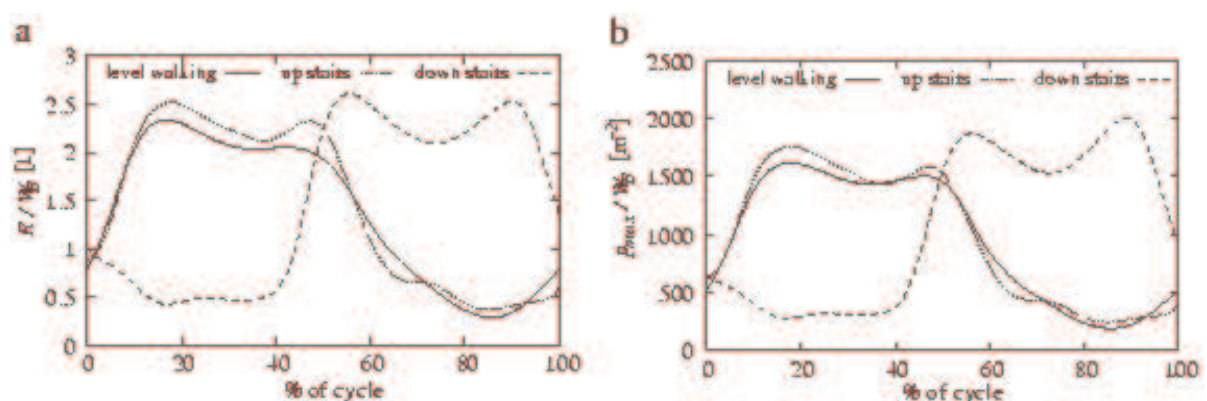


Fig. 1 The time dependencies of the normalized hip joint resultant force R/W_B (a), and normalized peak contact stress (p_{max}/W_B).

Time dependencies of these magnitude of force \mathbf{R} normalized to the body weight of patient (R/W_B) and peak contact stress normalized to the body weight (p_{max}/W_B) during the

level and staircase walking are shown in Fig. 1. It is worth noticing that the difference in R/W_B and p_{max}/W_B between normal walking and walking upstairs is less than 10%. Also the time courses of R/W_B and p_{max}/W_B in normal and staircase walking are very similar both in shape and values. The highest differences with respect to the situation in normal walking was found in walking downstairs where the maximum absolute values of R/W_B and p_{max}/W_B were observed. The maximum value of peak contact stress in walking upstairs is for 24% higher in comparison to the level walking.

The accuracy of the presented results can be influenced by the assumptions of the model for calculation the contact stress distribution. For example in the hip joint the underlying bone was taken to be absolutely rigid while in physiological state deformations of the bone under physiological conditions could change the stress distribution. Also deviations from the spherical shape of the bone surfaces of the femoral head and acetabulum change the cosine stress distribution, and the accuracy of the predicted values of the peak contact stress. It is well acknowledged that elevated peak contact stress acting over a longer period may induce degeneration of the articular cartilage, i.e., development of coxarthrosis.

We have observed that going upstairs and downstairs increase both the joint force and the peak contact stress with respect to the normal walking (Tab. 1). This is in accordance to other studies that report high load of the hip in staircase walking.

From the clinical study it was concluded, that the incidence of coxarthrosis is higher in patients frequently walking upstairs [1]. However, in our study it was shown that peak contact stress during walking upstairs differs only slightly from normal walking (Fig. 1b) and that the peak contact stress is much higher in descending stairs. If the hypothesis of high contact stress induced arthrosis is taken into account, it can be concluded that more than climbing stairs, descending stairs may be a cause of the observed higher incidence of coxarthrosis. Therefore people which would like to preserve their hips should rather use an elevator instead of walking downstairs than use the elevator instead of walking upstairs.

Acknowledgement

The research is supported by the Czech Ministry of Education project: Transdisciplinary research in Biomedical Engineering, No. MSM 210000012.

References

- [1] Lau, E.C et al. Am. J. Epidem, 152: (2000) 855862A.
- [2] Iglič, V. Kralj-Iglič, M. Daniel, and A. Maček-Lebar. Comp. Met Biomech Biomed Eng, 5 (2002), 2002.
- [3] G. Bergmann. Hip98, Loading of the hip joint. Freie Universitat, Berlin, 2001.

Design of the articular cartilage in the human hip joint is optimized to sustain load

M. DANIEL^{1,2}, V. KRALJ-IGLIČ³, A. IGLIČ⁴ AND S. KONVIČKOVÁ¹

¹ Laboratory of Biomechanics, Department of Mechanics, Faculty of Mechanical Engineering, Czech Technical University in Prague, Technická 4, 166 07 Prague, Czech Republic

² Department of Applied Mechanics and Mechatronics, Faculty of Mechanical Engineering, Technical University of Košice, Letná 9, 042 00 Košice, Slovakia,

³ Institute of Biophysics, Medical Faculty, Lipičeva 2 and Department of Orthopaedic Surgery, University Medical Center, Zaloška 9, SI-1000Ljubljana, Slovenia

⁴ Laboratory of Applied Physics, Faculty of Electrical Engineering, Tržaška 25, SI-1000 Ljubljana, Slovenia
e-mail: daniel@biomed.fsid.cvut.sk

Articular cartilage covers the moving surfaces inside the biarticular joints and ensures smooth movement with very low friction. In the hip joint spherical femoral head articulates with the cup-like acetabulum in the hip bone. From the engineering point of view, it seems to be reasonable to expect that the cartilage would cover whole acetabulum to provide large weight-bearing surface. However, in a real hip joint the articular surface of the acetabulum is horseshoe-shaped leaving the non-weight bearing area without cartilage medially. This work is intended to explain the specific shape of the articular cartilage using the mathematical model of the contact stress distribution in the human hip.

An analytical mathematical model of the contact stress distribution in the human hip joint has been developed recently [1]. Within this model the contact stress distribution in the hip was described as the product of the peak value of the stress and a cosine function of the angle between the given point on the articular surface and the point of the peak contact stress. This model assumes that the articular cartilage in the hip joint has a shape of hemisphere.

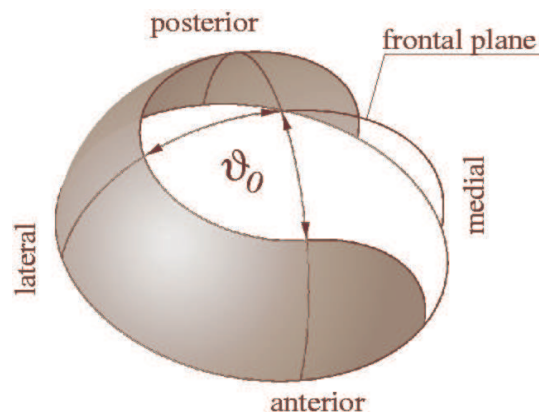


Fig.1 Shape of the hip articular surface

Within this work the position of the acetabulum the geometry of the acetabular cartilage was modified by introducing a non-weight bearing area within the articular cartilage. This non-weight bearing area represents the cartilage-devoid region of the acetabulum the acetabular fossa (Fig. 1). The acetabular fossa was taken to be symmetrical with respect to the frontal plane. Frontal plane of the body is also a plane of symmetry of the acetabular shell and divides acetabulum into anterior and posterior part (Fig. 1). The second plane of the symmetry of the acetabulum is perpendicular to the frontal plane and divides acetabulum into lateral and medial part. In the lateral part acetabular fossa consists of all points that have an angular distance from the axis of symmetry of the acetabulum lower than θ_0 (Fig. 1). In the medial part, the acetabular fossa consists of all points with an angular direction from the frontal plane

lower than \odot_0 (Fig. 1). Such definition allows to change the size the acetabular fossa and size of the cartilage as well by changing one parameter only while remaining cartilage has a typical horseshoe shape [2].

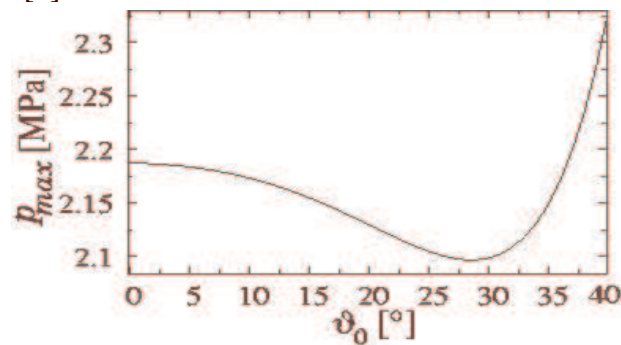


Fig.2 Dependence between the peak contact stress and size of the acetabular fossa

The hip joint is loaded by the hip joint resultant force. From the mathematical simulations [1] and measurements using an implanted instrumented endoprosthesis [3], it follows that the hip joint resultant force acts medially with respect to the axis of symmetry of the acetabular hemisphere.

We have studied dependence between the peak contact stress in the hip joint (p_{max}) and hypothetical size of the acetabular fossa (\odot_0) (Fig. 2). Presence of the acetabular fossa decreases p_{max} until it reaches its minimum at $\odot_0 = 29$. Further increase in the size of the acetabular fossa causes considerable increase in the peak contact stress.

The contact stress distribution in the human hip is considered to be an important factor that influences development of the hip. Therefore it is interesting that a specific shape of the articular cartilage exists that lowers peak contact stress (Fig. 2). The descent of the peak contact stress in the presence of the acetabular fossa can be explained if the load of the hip is considered. The acetabulum is loaded off-center in the one-legged stance, i.e., the hip joint resultant force \mathbf{R} acts close to the lateral acetabular margin [1]. Therefore the contact stress is distributed also asymmetrically with respect to the acetabular shell with the maximum shift towards the lateral acetabular margin (Fig. $\odot_0 = 0$). The acetabular fossa presents an area that could not bear weight and contributes to the symmetry of the articular surface with respect to the loading force \mathbf{R} . The more symmetrical is the articular surface to \mathbf{R} , the more uniform is the stress distribution. For a certain range of sizes of the acetabular fossa (\odot_0), it results to a decrease in the peak contact stress. However, if the acetabular fossa is too large, available contact articular surface is considerably diminished and the peak contact stress is increased (Fig. 2).

The horseshoe shape of the articular cartilage so contributes to the lowering and more uniform hip joint contact stress distribution which may be important in cartilage development and nutrition. In conclusion can be stated that the horseshoe shape of the articular cartilage in the hip joint optimizes the contact stress distribution on the articular surfaces.

Acknowledgement

The research is supported by the Czech Ministry of Education project: Transdisciplinary research in Biomedical Engineering, No. MSM 210000012.

References

- [1] A. Iglič, V. Kralj-Iglič, M. Daniel, and A. Maček-Lebar. *Comp. Met Biomech Biomed Eng*, 5 (2002), 2002.
- [2] A.M.R. Agur, editor. *Grant's Atlas of Anatomy*. Williams & Wilkins, Baltimore (1991).
- [3] G. Bergmann. *Hip98, Loading of the hip joint*. Freie Universitat, Berlin, 2001.

3D visualization of mouse aorta by dual-wavelength optical coherence tomography

J. SMOLKA¹, A. MATEAŠIK² AND D. CHORVÁT, JR.^{1,2}

¹ Faculty of Mathematics Physics and Informatics, Comenius University, Bratislava, Slovakia

² International Laser Centre, Bratislava, Slovakia

e-mail: smolka@ilc.sk

Introduction: Optical coherence tomography (OCT) perform high resolution tomography imaging of the internal structure of materials and biological specimen by measuring back-scattered light [1]. OCT is proven to be sufficient tool for early diagnosis for wide range of diseases accompanied by structural changes in superficial layers of investigated tissue. Despite the fact of very high resolution of OCT and opportunity to perform scanning in vivo and in real-time, OCT technique has specific drawbacks. In general, OCT scans give information only about optical density of tissue and not about the real structures, thus quantitative spatial calibration is impossible and biological interpretation of obtained data is not straightforward. Also some details of tissue structure easily visible by other optical techniques such as optical microscopy could be difficult to identify [2]. There exist several approaches how to overcome these limitations, for example using two different wavelengths for OCT scanning and/or 3D reconstruction of inspected objects from volumetric OCT scans.

Aim: Demonstration of possibility to use OCT system using detection on two different wavelengths simultaneously for 3D visualization of mouse aorta.

Material and Methods: Aortas from sacrificed rats were fixed in 4% buffered formaldehyde and investigated *in vitro*. We used compact, dual wavelength, fiber based OCT scanner from Optimec Ltd. and Institute of Applied Physics of Russian Academy of Sciences (Nizhny Novgorod, Russia) to perform OCT imaging. The scanner operated at wavelengths 833 nm and 1284 nm, generated from the superluminescent light emitting diodes producing 0.5 mW and 1.5 mW respectively. Scans at both wavelegths were recorded simultaneously. Single transverse scans were accomplished in 10 – 13 seconds. The in-depth resolution of the scanner was 13 μm (833 nm) and 17 μm (1284 nm); the lateral resolution was 17 μm (833 nm) and 20 μm (1284 nm). The operation of the scanner was completely controlled by a personal computer. A scanning volume of (2mm x 1mm x 1mm) was used. 3D models were created form series of 100 equidistant cross-sectional OCT scans. The distance between scans was 20 μm , defined by transverse resolution of the OCT equipment. The resulting volumetric datasets were processed and visualized by algorithms developed under Iris Explorer visualization environment (NAG, Oxford, UK). Computations and visualisations were performed on the Sun Ultra 60 Workstation or PentiumIII PC.

Results: The usage of two different wavelengths allowed better recognition of various structures in vessels due to combination of reflectance maps at each wavelength (Fig.1). Merging of scans obtained at different wavelengths provide better contrast in composite images. Volumetric data (Fig. 2A) were reconstructed in the form of 3D surface model (Fig.2B) using marching-cube algorithm. This algorithm is based on surface rendering through voxels with certain threshold value that corresponds to selected structural features in data. In our case, value for surface reconstruction was chosen to represent the boundaries of the vessel wall. The total free lumen volume could be estimated from the 3D dataset by integration of the free lumen volume in individual OCT scans.

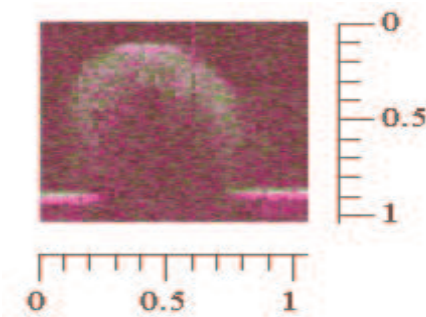


Fig. 1 OCT image of the vessel.
The scale shown is given in mm.

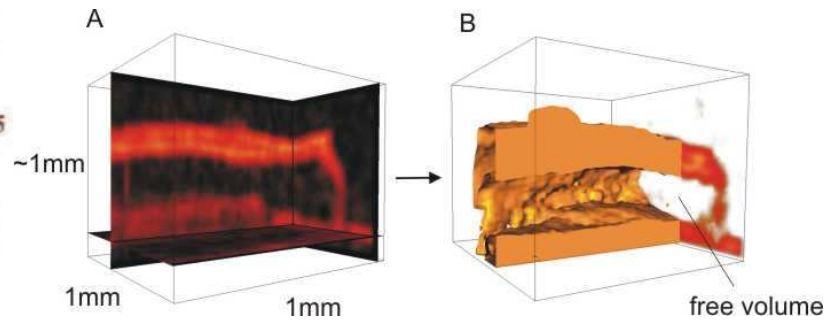


Fig. 2 3D reconstruction of the mouse aorta.
A) scanned volume B) reconstructed surface.

Conclusion: We have shown that OCT imaging is capable to visualize the 3D structure of *in vitro* mouse vessels. It provides sufficient resolution on the near-histological level, with an advantage of fast processing of large number of slices without mechanical and/or chemical treatment. Such approach is impossible to achieve by standard microscopy protocols. It also retained the exact 3-dimensional structure of the vessels, so that the resulting models could be used as a starting point for further modeling of blood circulation etc.

Though the resolution of our scanner did not allow us to identify subtle details of the vessel wall, the 3D model of the reconstructed aorta provided valuable volumetric information. Post-processing of obtained models, such as numerical integration of free lumen volume, can supply set of quantitative attributes which can be used e.g. for characterization of arterosclerotic plaque development in vessels.

Acknowledgement

This work was supported by Slovak Science Grant Agency under contract VEGA 1/0509/03.

References

- [1] B. E. Bouma, G. J. Tearney: Handbook of Optical Coherence Tomography, Marcel Dekker, Inc., New York, USA, 2002.
- [2] L. Thrane: Optical Coherence Tomography: Modeling and Applications, Riso National Laboratory, ISBN 87-550-2771-7, Roskilde, Denmark, 2001.

Structural and functional changes in cytochrome *c* oxidase induced by high hydrostatic pressure

J. STANIČOVÁ¹, A. MUSATOV² AND N.C. ROBINSON²

¹Institute of Chemistry, Biochemistry and Biophysics, The University of Veterinary Medicine, Komenského 73, 041 81 Košice, Slovakia

²Department of Biochemistry, The University of Texas Health Science Center, San Antonio, Texas 78229-3900
e-mail: stanicova@uvm.sk

Structural and functional stability of bovine cytochrome *c* oxidase (CcO) as a function of exposure to high hydrostatic pressure is reported. The pressure affects the stability of monomeric and dimeric enzyme quite differently. Exposure of the monomeric CcO to pressures higher than 2.5 kbar causes dissociation of subunits III, VIa, VIb, VIIa with a 35 – 50 % decrease in electron transport activity. Here we present the evidence that the loss of enzymatic activity of monomeric CcO is associated with the dissociation of subunit VIIa and is not caused by the dissociation of subunits III, VIa, VIb as well as functional important phospholipid cardiolipin. Dimeric CcO is more resistant to high hydrostatic pressure since subunits III and VIIa do not dissociate and the electron transport activity is minimal. This result can contribute to the general assumption that dimeric form of CcO occurs *in vivo*.

Cytochrome *c* oxidase (CcO; Ec 1.9.3.1) is the terminal enzyme of the inner mitochondrial electron transport chain. It is a multisubunit complex that catalyses electron transfer from reduced cytochrome *c* to molecular oxygen. Bovine heart CcO is a protein-phospholipid complex consisting of 13 different subunits [1]. High hydrostatic pressure is a powerful tool for probing protein and enzyme stability, especially for perturbation of enzymatic activity due to protein unfolding, or dissociation of subunits from oligomeric proteins [2].

To give the evidence that decrease in molecular activity of monomeric CcO is caused by the dissociation of subunit VIIa we used HiTrapQ ion exchange chromatography method for a determination of the elution of purified CcO after exposure to 2.5 kbar in dependence of time (Fig. 1). This method allows a separation of intact 13-subunit CcO complex (peak A in Fig. 1) from the forms that are missing subunits (11-subunit form missing subunits VIa, VIb – peak B and 9-subunit form missing subunits III, VIa, VIb, VIIa – peak C in Fig. 1). We used reversed phase C₁₈ HPLC method as a quantitative analytical procedure and calculated content of subunit VIIa in the 9-subunit complex after exposure to 2.5 kbar for 0, 20, 30, 120 min (peaks C in Fig. 1). Areas of C₁₈ HPLC elution peaks corresponding to subunit VIIa (not shown) were measured and compared to pressure-untreated enzyme.

Percent of enzymatic activity as a function of content of subunit VIIa in peak C is plotted in Fig. 2. From figure it can be seen that the decrease in enzymatic activity was caused by the decrease in subunit VIIa content. This result is consistent with the decrease in molecular activity of monomeric CcO (containing intact 13-subunit complex, 11-subunit and 9-subunit complexes) exposed to 2.5 kbar for 0, 20, 30, 120 min, which was taken before HiTrapQ chromatography procedure (Fig. 2 – inset panel).

As expected [3], the molecular activity of 11-subunit complex, which is completely devoid of subunits VIa and VIb is identical to that of the intact enzyme. Therefore, subunits VIa, VIb are not responsible for the loss of activity.

Subunit III is one of the three core subunits of CcO, which does not contain any of the redox centers. Experiments with mutagenized subunit III indicate normal activity of CcO in electron transfer [4]. In coincident with these findings we found that subunit III is not responsible for the loss of enzymatic activity caused by the exposure to high pressure.

Excellent evidence is the correlation between reversibility of subunit III and irreversibility of CcO molecular activity (not shown).

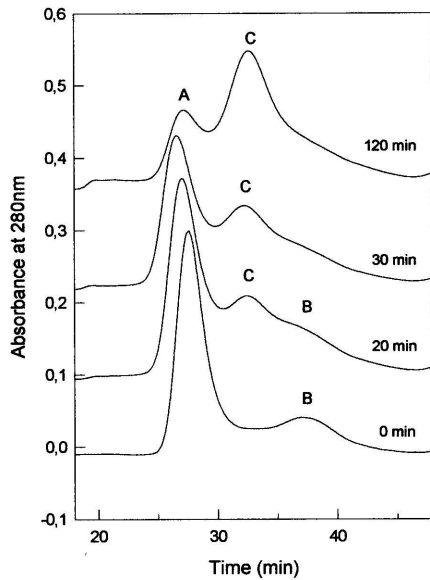


Fig. 1 HiTrapQ ion chromatography elution of monomeric CcO (5 μ M) as measured after exposure to 2.5 kbar hydrostatic pressure for 0, 20, 30, 120 min.

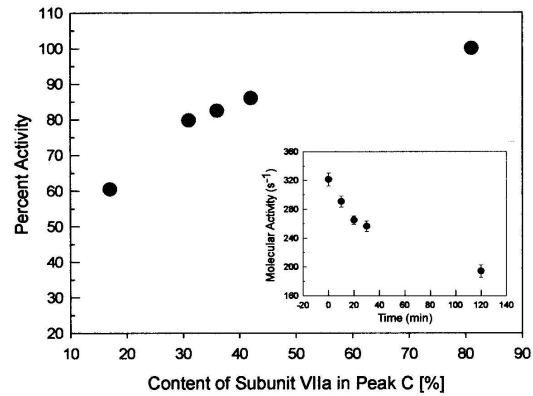


Fig. 2 Percent activity as a function of content of subunit VIIa in peak C. Inset panel: Time dependence of monomeric CcO activity as measured after exposure to 2.5 kbar pressure for 0, 20, 30, 120 min.

In addition, exposure of monomeric CcO to 2.5 kbar hydrostatic pressure does not cause dissociation of two functionally important cardiolipins, therefore, the loss of enzymatic activity is not caused by dissociation of cardiolipin but is clearly caused by dissociation of subunit VIIa.

Acknowledgement

This work was supported by the research grants from NIH (GMS 247955) and The Robert Welch Foundation (AQ 1481) and grant from Slovak Grant Agency Vega No. 1/0640/03. The authors especially wish to thank Mark Panda for his help with pressure experiments and Linda Sowdal for technical assistance.

References

- [1] B. Kadenbach, J. Jaraush, R. Hartmann and P. Merle, *Anal. Biochem.* 129 (1983), 517-521.
- [2] V.V. Mozhaev, K. Heremans, J. Frank, P. Masson and C. Balny, *Proteins: Structure, Function and Genetics* 24 (1996), 81-91.
- [3] E. Sedlák and N.C. Robinson, *Biochemistry* 38 (1999), 14966-14972.
- [4] T. Haltia, M. Saraste and M. Wikström, *EMBO J.* 10 (1991), 2015-2021.

Capillary microscopy of human peripheral microcirculation

M. BITTNEROVÁ¹, P. MUSIL², Z. BAŤOVÁ¹ AND J. KYSELOVIČ¹

¹ Pharmaceutical faculty, UK Bratislava

² Faculty of mathematic, physic and informatic, UK Bratislava
e-mail: bittnerova@fpharm.uniba.sk

Introduction: Our apparatus for nailfold capillary microscopy (capillaroscopy) is the first noninvasive method offering investigation of the human skin capillaries and hemodynamics of capillary blood flow [1] in Slovakia. It consists of optical microscope with CCD camera connected to PC allowing online video recording and offline processing of the examined capillaries. There are known some capillaroscopic data such as red blood cell velocity (CBV), capillary density or capillary width from other laboratories [2, 3, 4, 5], but our system allowing frame to frame analysis of CBV and morphometric parameters of capillaries are not tested and validated.

Aim: To demonstrate the measurement of the CBV and morphometric parameters of nailfold capillary limbs using the capillary microscopy in healthy subjects. Acquired data compare to published ones for testing the reproducibility of this new method.

Material and Methods: In vivo nailfold capillary microscopy (made in Centre of analysis of substances, Joint Strock Company, Moscow 2001) was performed on 15 apparently healthy subjects, 6 males (40%) and 9 females (60%), ranged in age 23 to 32 (mean 26). The subjects were examined in sitting posture at room temperature of 21-25 °C for 30 min. The fourth finger was fastened by plastic holder with temperature 37°C during the whole measurement. To increase transparency a drop of immersion oil was placed on the nailfold before examining the capillaries in the nail bed. CBV in arterial, venous and transition limb (Figure 1) was calculated from 10 s of continuous recording using frame-to-frame analysis. Data concerning CBV of subjects are the mean of three measurements. Morphometric parameters such as length and diameter of capillary limbs were calculated. Mann-Whitney test was used to compare data and $p < 0.05$ was considered to represent a statistically significant difference. The mean and standard deviation (SD) were also calculated.

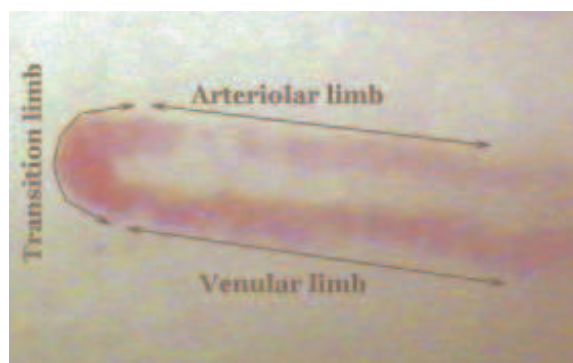


Fig. 1 Capillary limbs

Results: CBV in arterial limb (789 $\mu\text{m/s}$, range 227-2096 $\mu\text{m/s}$) was nonsignificantly higher compare to CBV in venous limb (567 $\mu\text{m/s}$, range 154-1907 $\mu\text{m/s}$). Significant difference was showed between CBV in arterial and transition limb (789 to 298 $\mu\text{m/s}$, $p < 0.01$). CBV in venous limb was significantly higher than in transition limb ($p < 0.05$) (Figure

2). Arteriolar diameter was significantly lower compared with venous and transition limb: 9.8 to 14.3 ($p<0.01$) and 18.9 ($p<0.001$), respectively. Significant difference showed comparing of venular diameter and diameter of transition limb ($p<0.05$).

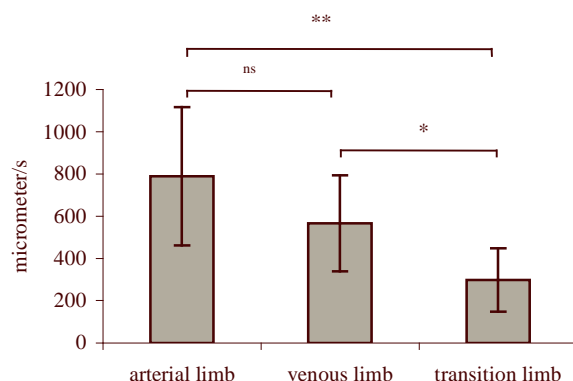


Fig. 2 Red blood cell velocity in arterial, venous and transition limb of total group ns, nonsignificant difference between CBV in arterial limb vs in venous limb
 * $p<0.05$, CBV in venous limb vs in transition limb
 ** $p<0.01$, CBV in arterial limb vs in transition limb

Tab. 1 Morphometric parameters of capillary limbs

parameters [μm]	length [mean \pm SD]	diameter [mean \pm SD]
arterial limb	100 \pm 40,9	9,8 \pm 4,5
venous limb	111,1 \pm 35,9	14,3 \pm 4,2 **
transition limb	36,1 \pm 15,3	18,9 \pm 6,5 ***, †

ns, nonsignificant difference between arteriolar length vs venular length
 ** $p<0.01$, arteriolar diameter vs venular diameter
 *** $p<0.001$, arteriolar diameter vs diameter of transition limb
 † $p<0.05$ venular diameter vs diameter of transition limb

Discussion and Conclusion: We demonstrated using of the nailfold capillaroscopy for investigation of the human nailfold microcirculation. Our values of capillary blood flow velocity are comparable to published physiological data. Differences in capillary morphometric parameters compared with data from other clinical studies could be caused by different magnification of our system. On the other hand further investigation have to be done to test validity of this method.

References

[1] M.J.H.M. Jacobs, I.D. Gregoric and G.J. Reul, *Texas Heart Institute Journal* 19 (1992),123-129.
 [2] CH-H. Chang, R-K. Tsai, W-CH. Wu, S-L. Kuo and H-S Yu, *Microvascular Research* 53 (1997), 121-127.
 [3] M.Maeda, K. Matubara, H. Kachi, S. Mori and Y. Kitajima, *Journal of Dermatological Science* 10 (1995), 35-41.
 [4] E. Bonacci, N. Santacroce, N. D' Amico and R. Mattace, *Arch Gerontol Geriatr.* suppl.5 (1996), 79-83.
 [5] T.F.T. Antonios, D.R.J. Singer, N.D. Markandu, P.S. Mortimer and G.A. MacGregor, *Hypertension* 33 (1999), 998-1001.

Changes in global stability of ferricytochrome c upon adding of polyanions

J. BÁGELOVÁ AND D. FEDUNOVÁ

Department of Biophysics, Institute of Experimental Physics, Watsonova 47, Košice, Slovakia
e-mail: fedunova@saske.sk

The tendency of proteins to spontaneously adopt a well-defined conformation in solution has intrigued investigators for many decades. Thermally induced conformational changes are associated with denaturation processes which can provide an insight into those structural features of the proteins that are functionally important. Increasing attention is being paid to the relationship between protein function and the dynamics of conformational changes that are attendant on these processes. Formation of large “macroscopic” aggregates has been often observed in the course of protein denaturation and has always been considered as a nuisance and source of various artifacts. Protein association appears as a cause or symptom of several diseases such as prion disease, Alzheimer’s, or cataracts [1]. On the other hand, assembly of proteins into large complexes is an important mechanism used to attain greater efficiency and regulatory control of biological processes [2].

Macromolecular and polymolecular structures stabilized by the cooperation of numerous weak forces are important to most biochemical processes. Since such highly cooperative structures undergo conformational or phase transition upon being heated, DSC can provide significant information concerning these structures. The small compact globular proteins represent cooperative system; i.e. they exhibit an extreme cooperativity that integrates the whole of their structure into a single structural unit. Generally, comparison of calorimetric and van’t Hoff enthalpy can provide information about the denaturation process. A necessary, but insufficient, condition for a two-state denaturation process is that the calorimetric and van’t Hoff enthalpies are identical. Protein-protein interactions sharpen the transition, resulting in a larger apparent van’t Hoff enthalpy.

Horse heart cytochrome c (cyt c) has been used as a model protein because its native structure is well known and information on its stability and structural features under different conditions are available [3,4]. In the study presented here the effects of polyglutamate, heparin, SDS and PVS on cytochrome c global stability are discussed and reflections about denaturation cooperativity at different conditions are described. Cyt c as a basic protein (pI 10.1) undergoes the thermal denaturation with relatively high reversibility at condition from acidic to slight alkaline pH. We have shown that thermal transition of cyt c is two-state process as indicates the enthalpy ratio about 1. This system possesses irreversible thermal transition due to aggregation of denatured cyt c molecules. With increasing pH toward isoelectric value (pI 10.1) the overall charge is neutralized and enhanced intermolecular interactions lead to the increase of cyt c molecules number in cooperative unit. The protein oligomerization is manifested by the narrower denaturation curves with increasing enthalpy change ratio and significant decrease of thermal transition reversibility.

Binding of cytochrome c to polyglutamate alters the denaturation properties of the protein. Low concentration of PG or PVS (up to 0.2mg/ml) decreases temperature transition of cyt c and narrows temperature interval where process take place – comparing with free cyt c. We can say, that in certain meaning the process is more cooperative. The shape of calorimetric curve indicates that the denaturation process does not involve association or dissociation. A “cooperative unit “ created by molecules cytochrome c and polyglutamate is preserved during thermal denaturation. On the other hand, at saturated concentrations of PVS the ratio decreases to 1.6 and the reversibility of cyt c denaturation significantly increases to 95 %. Complexation with this flexible polyanion suppresses intermolecular contact among

denatured protein molecules due to the shielding of sticky surfaces by charged part of polyanion chain.

Complexation of cyt c with polyanions is frequently studied especially due to the ability of polyanions to induce similar structural response in cyt c as its physiological redox partners. The aim of this study is to determine the effects of polyanions on global stability of cyt c during the heat denaturation in near-isoelectric pH, and to test the possible aggregate-preventing ability of charged polymers on protein aggregation.

Acknowledgement

This work was supported by the research grant from the Slovak Grant Agency Vega No. 4068.

References

- [1] E. Benditt, A. Cohen, E. Franklin, G. Glenner, G. Husby *Amyloid and Amyloidosis. Int. Congr. Ser. No. 497* (1980), Elsevier, New York.
- [2] P.L. Privalov, *Adv. Protein Chem.* 33, (1979), 167-241.
- [3] Y. Hagihara, Y. Tan, Y. Goto, *J.Mol.Biol.* 237, (1994), 336-348.
- [4] A. Schejter, T.L. Luntz, T.I. Koshy, E. Margoliash, *Biochemistry* 31, (1992), 8336-8343.

Effect of cholesterol on the bilayer thickness in unilamellar 1,2-dimyristoleoyl and 1,2-dierucoyl phosphatidylcholine: SANS contrast variation study

J. GALLOVÁ¹, D. UHRÍKOVÁ¹, M. HANULOVÁ¹, J. TEIXEIRA² AND P. BALGAVÝ¹

¹Faculty of Pharmacy, Comenius University, Odbojárov 10, 832 32 Bratislava, Slovakia

²Laboratoire Léon Brillouin, CEA Saclay, 91999 Gif-sur-Yvette Cedex, France

e-mail: gallova@fpharm.uniba.sk

Cholesterol (CHOL) plays an important role in animal and fungal cell membranes as a modulator of physical and functional properties of lipid bilayers. CHOL is distributed heterogeneously among cellular membranes. It has been suggested that the correlation between the CHOL content of membranes and the hydrophobic sequence lengths of transmembrane proteins could play a role in membrane protein biogenesis due to changes in the membrane bilayer thickness caused by CHOL

Small-angle neutron scattering on extruded unilamellar vesicles in water was used to study bilayer thickness when CHOL was added at 44.4 mol % to 1,2-dimyristoleoylphosphatidylcholine (diC14:1PC) and 1,2-dierucoylphosphatidylcholine (diC22:1PC) bilayers. Using the ¹H₂O/²H₂O contrast variation and the small-angle form of Kratky-Porod approximation, the bilayer gyration radii at infinite contrast $R_{g,\infty}$ and the bilayer thickness parameters $d_{g,\infty}=12^{0.5}R_{g,\infty}$ were obtained at 30°C. Addition of cholesterol to diC14:1PC increased the $d_{g,\infty}$ from 3.72±0.02 nm to 4.27±0.06 nm, while in the diC22:1PC bilayers the $d_{g,\infty}$ change observed was smaller than experimental error: +0.23±0.24 nm.

Acknowledgement

This study was supported by the VEGA 1/0123/03, VEGA 1/9313/02 and APVT 51-013802 grants, and by the European Commission through the Access to Research Infrastructures Action of the Improving Human Potential Programme (contract HPRI-CT-1999-00032).

Study of intercalation effect of chosen anthraquinones into plasmidic DNA

V. HAVRILOVÁ¹, M. REFREGIERS², J.C. MAURIZOT², J. ADAMČÍK³, P. JASEM¹ AND P. MIŠKOVSKÝ^{1,4}

¹ Department of Biophysics, P. J. Safarik University, Jesenna 5, 041 54 Kosice, Slovakia

² Centre of Molecular Biophysics, rue Charles-Sadron, 450 71 Orleans Cedex 2, France

³ Department of Biochemistry, P. J. Safarik University, Moyzesova 11, 041 54 Kosice, Slovakia

⁴ ILC, Ilkovicova 3, 812 19 Bratislava, Slovakia

e-mail: havrilv@kosice.upjs.sk

Anthraquinone is planar, aromatic molecule. It is yellow, orange or light gray to gray-green crystal powder. Anthraquinone is prepared commercially by oxidation of anthracene or condensation of benzene and phthalic anhydride, followed by dehydration of the condensation product. This is the most important quinone derivate of anthracene and the parent substance of large class of dyes and pigments. We studied the conformational changes and intercalation of chosen anthraquinones (Quinizarin, Danthron) into plasmidic DNA by using gel electrophoresis and atomic force microscopy. It is known that planar, aromatic drugs interact with the deoxyribonucleic acid by the intercalation of their chromophores between two stashed base pairs of the double helical DNA molecule [1]. The intercalated molecule is stabilized by hydrophobic stacking interactions with adjacent base pairs [2]. Intercalators change the geometric parameters of supercoil DNA (sc DNA), whereby it varies the topology of plasmid DNA (pDNA), then number of superhelical turns of pDNA is changed.

The intercalation effect of Quinizarin (QUIN) and Danthron (DANTH) into the plasmid DNA was researched at different concentrations of anthraquinone derivates and pDNA, thus at various QUIN : pDNA and DANTH : pDNA ratios. Experiments, for which the concentration of Quinizarin was approximately 10^{-6} M, didn't show the intercalation of QUIN, because the concentration used was very low; we detected only the separation of plasmid DNA (oc and sc forms of pDNA). By using higher concentrations of Quinizarin (10^{-5} M – $9 \cdot 10^{-5}$ M) the gel electrophoresis provided us information about its intercalation into the plasmid DNA. With increasing concentration of QUIN, its intercalation effect advanced until the concentration $9 \cdot 10^{-5}$ M, for which we observed only relatively weakly visible oc forms of pDNA. At the highest concentration of Quinizarin approximately 10^{-4} M we didn't detect pDNA. It is due to the fact, that at high concentrations of QUIN, all binding sites in plasmid DNA are occupied by Quinizarin and Ethidium bromide, whose solution was used to visualize pDNA under UV lamp, have no more sites to bind to, to react with plasmid DNA. Therefore we observed either very weakly visible pDNA or we didn't even see it.

At the lower concentrations of Danthron ($4 \cdot 10^{-6}$ M) we didn't observed any intercalation effect; a little bit higher concentration of DANTH showed faint intercalation, but the oc forms of plasmid DNA were the most visible. In concentration range $8 \cdot 10^{-6}$ M – $9 \cdot 10^{-5}$ M we detected markedly visible intercalation. For the experiments with high concentration of Danthron (10^{-4} M, $2 \cdot 10^{-4}$ M) and higher pDNA concentration we observed still the intercalation bands, but with these high concentrations of anthraquinone problem appears to obtain quality image of gel and also occurs limitation to change the contrast. The measurements with higher concentration of DANTH as $2 \cdot 10^{-4}$ M didn't provide any information about the intercalation effect of DANTH into pDNA. From present measurements we can conclude, that Danthron intercalates into plasmidic DNA and as we detected its intercalation in a wider concentration interval than with Quinizarin and with as we observed more intercalation bands at lower concentrations, we can state, that it is a stronger and better intercalator than Quinizarin.

Acknowledgement

This work was supported by the Slovak Science and Technology Assistance Agency under the contract No. APVT-20-022202, grant No. 1/9040/02 of the Scientific Grant Agency of the Ministry of Education of Slovak Republic. The authors wish to thank Mrs. Françoise Culard from Centre of Molecular Biophysics in Orleans, France, for many stimulating discussions and providing of experimental conditions.

References

- [1] H. Porumb, The solution spectroscopy of drugs and the drug-nucleic acid interactions, *Prog. Biophys. Molec. Biol.*, Vol. 34 (1978), 175 – 195.
- [2] Richard R. Sinden, DNA Structure and Function, *Academic Press* (1994).

UV-VIS absorption and fluorescence investigation of the interactions of hydroxyanthraquinones with serum albumins

Z. JURAŠEKOVÁ, P. GBUR, G. FABRICOVÁ, D. JANCURA AND P. MIŠKOVSKÝ

Department of Biophysics, P. J. Šafárik University, Jesenná 5, 04 154 Košice, Slovakia

Hydroxyanthraquinones belong to an important class of biologically active and commercially valuable compounds. They are of interest as dyes, pesticides and fungicides as well as additives in lubricants. From biological point of view, molecules of this group possess ability to act as cytotoxic and genotoxic agents as well as the parent molecules for anthracycline antitumor drugs [1,2]. The interaction of hydroxyanthraquinones with serum proteins (serum albumin, lipoproteins...) can substantially modify biological activity of these molecules in biological systems.

Serum albumins are the most abundant plasma proteins and contribute significantly to many transport and regulatory processes. The proteins bind a wide variety of substrates such as metals, fatty acids, amino acids, hormones and an impressive spectrum of drugs [3]. Serum albumins are known to contain two specialized drug binding sites located in subdomains IIA and IIIA [3, 4].

In this work, we used UV-VIS absorption and fluorescence spectroscopy to study the interactions of selected hydroxyanthraquinones (emodin, quinizarin, dantron) with human serum albumin (HSA). Based on spectroscopic measurements we determined binding constants and suggested binding sites for individual hydroxyanthraquinones in HSA. Further we examined the influence of the presence of fatty acids in albumin structure on the binding of emodin, quinizarin and danthron with HSA.

Acknowledgement

This work was supported by the Slovak Science and Technology Assistance Agency under the contract No. APVT-20-022202, grant No. 1/9040/02 of the Scientific Grant Agency of the Ministry of Education of Slovak Republic.

References

- [1] I. Gutierrez, S. Bertolotti, M. Biasutti, A. Soltermann and N. Garcia, *Can. J. Chem.* 75 (1996), 423-428.
- [2] J.W. Lown, *Pharm. Ther.* 60 (1993), 185-214.
- [3] T. Peters, *Adv. Protein Chem.* 37 (1985), 161-245.
- [4] U. Kragh-Hansen, *Mol. Pharmacol.* 34 (1988), 160-171.

Solubilization of multilamellar liposomes by N-dodecyl-N,N-dimethylamine N-Oxide

J. KARLOVSKÁ, J. GALLOVÁ AND P. BALGAVÝ

Department of Physical Chemistry of Drugs, Faculty of Pharmacy, Comenius University, Odbojárov 10, 832 32 Bratislava, Slovakia
e-mail: karlovska@fpharm.uniba.sk

The solubilization of multilamellar egg yolk phosphatidylcholine (EYPC) liposomes by *N*-dodecyl-*N,N*-dimethylamine *N*-oxide (C12NO) was studied using turbidimetry. The solubilizing concentration c_S of C12NO was estimated as the C12NO concentration causing the half-maximum decrease in the turbidance. At all EYPC concentrations studied, the solubilizing concentration was lower than the C12NO critical micelle concentration. From the linear c_S dependence on EYPC concentration, the lipid bilayer – aqueous phase molar partition coefficient and the C12NO molar fraction in the C12NO + EYPC aggregates at c_S were obtained: $K_p = 1241 \pm 364$ and $X_{C12NO} = 0.6 \pm 0.1$. Using the concept of effective molecular shape parameter and the small-angle X-ray diffraction and neutron scattering data, the value $X_{C12NO} = 0.7$ is calculated for the onset of bilayer EYPC transformation into mixed micelles, close to the value estimated at c_S .

Acknowledgement

This study was supported by the VEGA No. 1/0123/03 and the APVT No. 51-013802 grants.

Green laser effect on the mitochondria

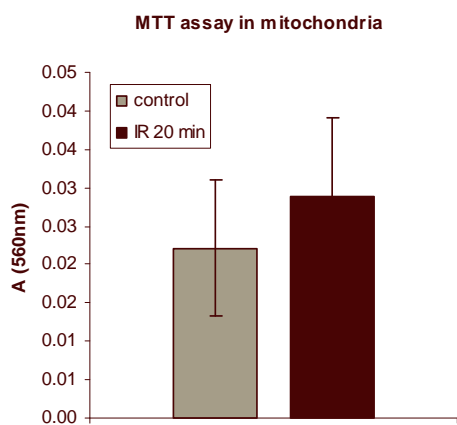
P. KAŠŠÁK, D. HABODÁSZOVÁ AND L. ŠIKUROVÁ

Department of Biophysics, Comenius University, Mlynská dolina, 842 48 Bratislava, Slovak Republic, e-mail: habodaszova@yahoo.com

The first publication about low-level laser therapy (LLLT) appeared more than 30 years ago [1]. Since then, the effectiveness and applicability of a variety of light sources, in the treatment of a wide range of medical conditions has thoroughly been investigated, *in vitro* as well as *in vivo* [for reviews see 2, 3]. In LLLT the question is no longer whether light has biological effects but rather how radiation from therapeutic lasers and LEDs works at the cellular and organism levels and what the optimal light parameters are for different uses of these light sources with various wavelengths [4]. Up today, green wavelengths band was not officially included into LLLT and stands on the edge of research interest in spite of its possible beneficial use. The fact that green light has small penetration depth in the biological tissues does not have to be only disadvantage as often mentioned, but also may be used in the very focused and gentle therapeutical interventions.

In presented work we investigated green laser radiation effect rat mitochondria in the matter of changed redox properties and membrane changes. Experiments were fulfilled on pellet of isolated Wistar rat heart mitochondria. Concentration of the isolated mitochondria was estimated by method of Lowry and pellet diluted by Tris-EDTA-KCl buffer (pH 7.4) to concentration 0.25 g/ml. Nd:YAG laser (30 mW, 532 nm) was used as a source of polarized and coherent light. Time of irradiation was set to obtain fluence 0.107 W/cm² per sample, representing the radiation energy 36 Joules. Controls were maintained in the dark and at the same conditions as irradiated samples.

In the preliminary experiments, survival of the cells after irradiation using Trypan Blue dye exclusion test was examined [5] with no observed differences.



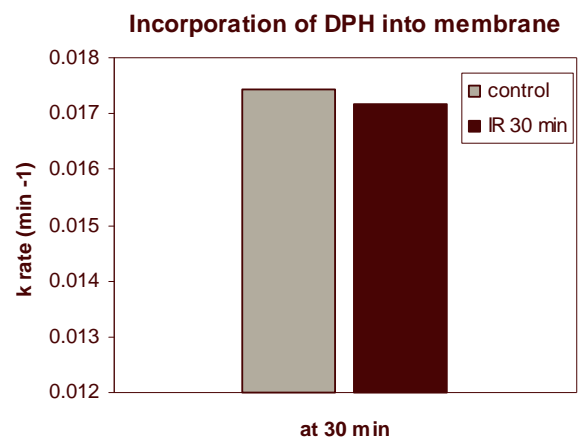
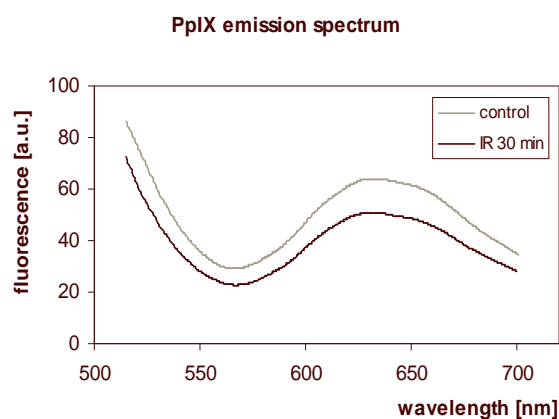
To evaluate the redox properties after irradiation MTT assay was used. The irradiation by green laser significantly increases ($P = 0.0329$) the ability of mitochondria to reduce water-soluble tetrazolium salt MTT which leads to precipitation of colored formazan crystals. Reduction of MTT in isolated cells and tissues is regarded as an indicator of cell redox activity. The reaction is attributed mainly to mitochondrial enzymes and electron carriers [6]. Thus we may suggest that the increase in the degradation is closely related to the positive stimulation of the mitochondrial enzymes and electron carriers. The redox properties alteration hypothesis [4]

postulates that photoexcitation of certain chromophores in the cytochrome c oxidase molecule (like Cu_A and Cu_B or hemes *a* and *a*₃) influences the redox state of these centers and, consequently, the rate of electron flow in the molecule.

We have also investigated whether the green laser irradiation modifies the membrane fluidity, as probed by membrane labelling with fluorescent dyes. We have studied the steady-state fluorescence anisotropy of 1,6-diphenyl-1,3,5-hexatriene (DPH). Stock solution was prepared in acetone ($5 \cdot 10^{-4}$ M) and dissolved in Tris-KCl-EDTA buffer (pH 7.4) to reach final concentration of DPH in sample $1 \cdot 10^{-6}$ M. We observed that 30 minutes long irradiation of the isolated mitochondria suspension decreased (not significantly) the anisotropy of the outer membrane. The fluidity of the outer mitochondrial membrane was thus decreased.

Irradiation also decreased the rate of DPH probe incorporation, which means that the membrane was becoming more rigid after the irradiation. However this decrease is not significant and we may suggest that the changes are not serious to change the functional properties of the membrane and affect the processes of respiratory chain in the mitochondria. As a cause of this observed “damaging” effect we may suggest PpIX photodynamic action. The prosthetic group of heme in cytochromes b, c1 and c is iron protoporphyrin IX, the same heme as in myoglobin and hemoglobin [7]. Also PpIX is initially synthesized from ALA in the mitochondria of the cell, and then diffuses into the cytoplasm of the cell [8], which was convinced by some experimental data [9,10].

Emission fluorescence spectrums of Protoporphyrin IX were collected in the samples without the presence of DPH. We excited sample of isolated mitochondria by light of wavelength 488nm and collected emission data at range 515 – 700nm. The emission of PpIX was examined at 635 nm with observed considerable decrease ($P = 0.02$) in the fluorescence of PpIX in irradiated sample. We suggest that decrease in PpIX fluorescence in irradiated samples is due to PpIX photobleaching during the photodynamic action. However, the concentration of the PpIX in isolated mitochondria is suggested to be very low, and thus the photodynamic effect has limited affection on membrane structure, and does not cause significant dysfunction.



In conclusion we may say, that this study suggests beneficial effects of Nd:YAG laser respective green laser light irradiation at the cellular and subcellular level, assuming potential beneficial clinical results and application in LLLT also for this wavelength light sources.

Acknowledgement

This work was supported by the research grant from the Slovak Grant Agency Vega 1/0253/03 and APVT 1/8310/01.

References

- [1] Kovács I., Mester E., Görög P., *Experientia* 30, (1974), 1275-1276.
- [2] Conlan M.J., Rapley J.W., Cobb C.M., *J Clin Periodontol* 23, (1996), 492-496.
- [3] Kukurova et al., *Obzory matematiky, fyziky a informatiky* 4, (2001), 23-30.
- [4] Karu T.I., *The Science of Low Power Laser Therapy*, Harwood Acad. Publ., London (1998).
- [5] Li K., Wong D., Hiscott P., Stanga P., Groenewald C., McGalliard J., *Br J Ophthalmol* 87, (2003), 216-219.
- [6] Bernas, Dobrucki, *Cytometry* 47, (2002), 236-242.
- [7] J.M. Berg, J.L. Tymoczko, L. Stryer (Eds), *Biochemistry (5th ed.)*, New York (2002).
- [8] Peng Q, Berg K, Moan J, Kongshaug M, Nesland JM., *Photochem Photobiol* 65, (1997), 235-251.
- [9] Zhang RG, Wang XW, Yuan JH, Guo LX, Xie H., *Cell Res.* 10, (2000), 71-77.
- [10] Tabata K, Ogura S, Okura I., *Photochem Photobiol* 66, (1997), 842-846.

Intercalation of N-(9-acridinylthiocarbamoyl)glycine into plasmid DNA

D. SABLOVÁ, M. KOŽURKOVÁ, P. DANKO, J. ADAMČÍK AND D. PODHRADSKÝ

Institute of Chemistry, Department of Biochemistry, Faculty of Sciences UPJŠ, Košice
sabdan@kosice.upjs.sk

Acridine derivatives are one of the oldest and most successful classes of bioactive agents. The reasons for the wide usefulness of the acridines as active chemotherapeutic agents include their ready synthesis [1], biological stability, efficient binding to DNA [2] and an ability to disrupt cellular DNA function.

The concept of interaction with DNA through intercalation was first demonstrated with proflavine [3] and later with other acridines. A number of aspects of the binding of acridine to DNA have been considered relevant to their chemotherapeutic effects and particularly to their anticancer activity [4].

N-(9-acridinylthiocarbamoyl)glycine (TU) was, for the first time, prepared in our laboratory [5].

In the presented work, the effect of N-(9-acridinylthiocarbamoyl)glycine on plasmid DNA has been studied. Optical absorption, fluorescence spectroscopy and TGGE electrophoresis have been used to analyze the molecular intercalation of N-(9-acridinylthiocarbamoyl)glycine into plasmid DNA (pUC 19).

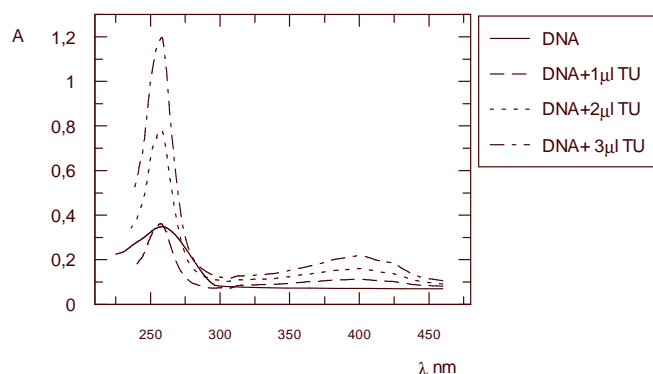


Fig. 1 UV-VIS titration spectra of pUC19 DNA plasmid (22.9 μ l/ml) with N-(9-acridinyl-thiocarbamoyl)glycine (stock solution: $1 \cdot 10^{-2}$ M in DMSO) measured in 0.1 M Tris buffer (pH 7.0) at 24 $^{\circ}$ C. Titration steps : 1 μ l, 2 μ l and 3 μ l.

The absorption spectrum of the thiourea with DNA measured in 0.1 M Tris buffer exhibited a broad absorption of high resolution in the regions 240-300 nm and 320-460 nm. Peaks have been changed in dependence of added amount of thiourea (Figure 1).

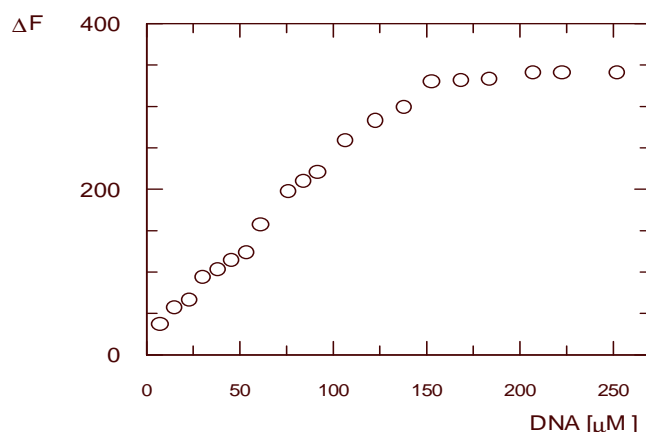


Fig. 2 Spectrofluorimetric analysis of TU ($8.3 \cdot 10^{-8}$ M) with various concentrations of pUC 19 plasmid DNA (22.9 μ l/ml) measured in 0.1 M Tris buffer (pH 7.0) at 24 $^{\circ}$ C. The fluorescence emission spectra were measured at wavelength $\lambda_{ex} = 396$ nm.

TU-DNA complex exhibits two fluorescence peaks at 435 nm and 459 nm depending upon the type of interaction. When TU intercalates into DNA, presumably by forming π - π interaction or stacking complex.

Spectrofluorometric analysis of the TU with pUC19 at $\lambda_{\text{ex}}=396$ nm was performed. The association curve for TU over series of steadily increasing DNA concentration, ranging from 8 to 252 μM of DNA, is shown in Figure 2.

To determine the association constant for the TU-DNA complex, delta absorbance values were taken at $\lambda_{\text{max}}=459$ nm and plotted against the concentration of DNA according to the method of Wyman and Gill [6].

The calculated K_{assoc} for the TU-DNA complex was found to be $1.23 \cdot 10^6 \text{ M}^{-1}$.

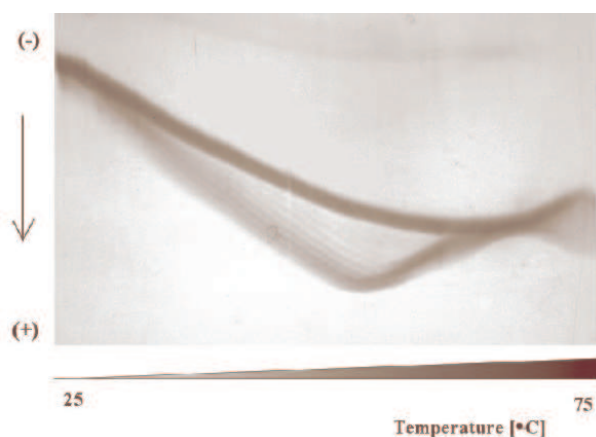


Fig. 3 TGGE of pUC19 in plasmid DNA (22.9 $\mu\text{l/ml}$) of 4 $\mu\text{l/ml}$ TU. The direction of DNA mobility is from the anode/up to cathode/down. Gels were electrophoresed at the indicated temperature gradient in 0.5xTBE (pH 7.8) at 6V/cm for 4 hours.

TGGE experiment presents the intercalating effect of TU into plasmid DNA. Decreasing level of negative supercoiling induced better distribution of negative topoisomers in the gel (Figure 3).

All used methods confirmed that N-(9-acridinylthiocarbamoyl)glycine was intercalated into pUC 19 plasmide DNA.

Acknowledgement

This work was supported by the research grant from the Slovak Grant Agency Vega No.1/1274/04 and 1/043/03. The authors are grateful to Mgr.G.Žoldák for his help.

References

- [1] W.A.Denny et al., In: Molecular aspect of anticancer drug action, Vol.1, S. Neidle and M.J.Waring (Eds.), Macmillan, London (1992).
- [2] D.J. Greenwood, Antimicrob. Chemother., 36 (1995), 857-872.
- [3] M.J. Wainwright, J. Antimicrob. Chemother., 47 (2001), 1-13.
- [4] M.J.Waring, J.Eur.J.Cancer, 12 (1976), 995-1001.
- [5] D.Sabolová at al., Collect.Czech.Comm., 59 (1994), 1682-1690.
- [6] J. Wyman and S.J.Gill, In: Binding and Linkage, University Science Book, Mill Valley, California (1990).

Specific and non specific interactions of proteins with DNA and DNA aptamers

V. OSTATNÁ AND T. HIANIK

Faculty of Mathematics, Physics and Computer Sciences, Comenius University, Mlynska dolina F1, 84248 Bratislava, Slovakia

The mass detection method and a method utilizing the electrochemical indicator methylene blue (MB) was used to study the interaction of human serum albumin (HSA), bovine serum albumin (BSA) and thrombin with either 19-mer single stranded DNA (ssDNA) or double stranded DNA (dsDNA) or with DNA aptamers specific to thrombin. We showed, that HSA interacts both with ssDNA and dsDNA as is revealed from the shift of the reduction potential of the MB. The HSA presumably interacts with both bases and sugar-phosphate backbone of ssDNA, while mostly with sugar-phosphate backbone of dsDNA. The adsorption of HSA to ssDNA determined by the QCM method using a quartz crystal microbalance (QCM) is non-specific and is described by Langmuir isotherm. The binding constant of HSA to ssDNA determined by the mass detection method ($K_c=77.9\pm 11.2 \mu\text{M}^{-1}$) was close to the value determined by electrospray spectrometry and electrophoresis methods [1,2]. We compared also specific and non specific interaction of thrombin and BSA with thrombin specific aptamers immobilized on a amphiphilic film on a gold support. We developed novel method of detection thrombin-aptamer interaction based on measurement the charge consumption from the electrode covered by DNA aptamers to an electrochemical indicator methylene blue (MB), that is bounded to a thrombin. We showed that using MB it is possible to detect thrombin with high sensitivity, which is comparable with QCM and fluorescence detection methods

Acknowledgement

This work has been supported by European Commission within 6 FP (project No. 506579) and by Slovak Grant Agency VEGA (Project No. 1/1015/04).

References

- [1] M.J. Greig, H. Gaus, L.L. Cummins, H. Sasmor, R.H. Griffey, J. Am. Chem. Soc., 117 (1995) 10765.
- [2] T. Hianik, V. Ostatná, Z. Zajacová, J. Electroanal. Chemistry. 564 (2004) 19.

Deformability of multilamellar vesicles

M. RICHTEROVÁ AND V. LISÝ

Department of Biophysics, Institute of Physics, P.J. Šafárik University, Jesenná 5, 041 54 Košice, Slovakia
e-mail: mrichterova@post.sk

It is now widely accepted that the density of the surface energy of a lipid-bilayer membrane of vesicles can be expressed in the Helfrich's form [1]

$$\varepsilon = \sigma + \frac{1}{2} \kappa \left(\frac{1}{R_1} + \frac{1}{R_2} - \frac{2}{R_s} \right)^2 + \frac{\bar{\kappa}}{R_1 R_2}, \quad (1)$$

where σ is the microscopic surface tension, R_i are the local curvature radii, R_s the spontaneous curvature radius, and κ and $\bar{\kappa}$ are the bending and Gaussian rigidities. A free vesicle has no genuine surface tension, i.e. $\sigma = 0$. However, it has been shown in Ref. [2] that multilamellar droplets (“onions”) exhibit an effective surface tension, σ_{eff} , that is nonzero even if the bilayers themselves have zero surface tension. The vesicle was modeled by a system of a large number of concentric membranes of small thickness d . The membranes are separated by water layers of thickness $d_w \gg d$. In a solvent the membranes deform due to the thermal fluctuations in the shape. Another contribution to the deformations of the layers is connected with their mutual interaction. Relating the deformation energy to the energy of deformation as it would be for a layer changing its surface area and having the surface tension σ_{eff} , this quantity has been determined [2],

$$\sigma_{eff} = \left[\frac{l(l+1)}{(l-1)(l+2)} \frac{\kappa B}{d_0} \right]^{1/2}. \quad (2)$$

Here B is a constant of interaction between the layers, $d_0 = d + d_w$, and $l = 2, 3, \dots$ number the deformation modes. At large l Eq. (2) becomes identical with the result for planar symmetry of the lamellar phase [3]. The conclusion that the effective surface tension of the multilamellar vesicle is nonzero even for zero surface tension of the bilayer is true. However, in the present work we have shown, that σ_{eff} considerably differs from the expression (2). This is a consequence of the bending energy contribution to the deformation energy (not considered in Ref. [2]) as it follows from Eq. (1), and a very large number of the deformation modes.

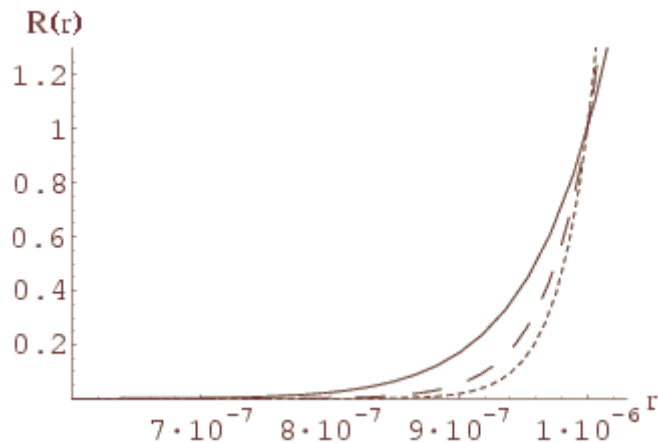
First, we have calculated σ_{eff} for a unilamellar vesicle with the zero microscopic surface tension and the equilibrium radius R_0 . Its surface energy density is given by Eq. (1) with $\sigma = 0$ and $R_s = \infty$. The deviation from the spherical equilibrium shape is described by the multipole expansion in spherical harmonics [1]. Calculating the deformation through the fluctuation amplitudes u_{lm} and the change of the surface area of the droplet, A (keeping its volume constant), we find $\sigma_{eff} = \Delta E_s / \Delta A$. Often only the most dominant ellipsoidal mode (giving the main contribution to the thermodynamic quantities) is considered; then $\sigma_{eff} \approx 6\kappa/R_0^2$. In general, one must sum the contributions from all the modes that gives $\sigma_{eff} \approx \kappa_{max}^2 / (2R_0^2 \ln l_{max})$, where the number of modes l_{max} is assumed to be very large, which holds for vesicles of a typical radius 10^4 \AA [1].

In the case of multilamellar droplets we, as distinct from [1], do not assume $\sigma = 0$ for the layers. This assumption is valid for a free vesicle but not in the case when the membrane is a part of a more complex structure, in particular, when it is stretched between bulky aggregates of membranes. When there is no interaction between the layers, the effective surface tension of the droplet is the same as above since only the outer layer is observed.

When the layers interact, we proceeded similarly as in Ref. [2]. The deformation of the n th layer expressed through spherical harmonics is

$$R_n(\vartheta, \varphi) = r_n \left[1 + \sum_{lm} a_{lm,n} Y_{lm}(\vartheta, \varphi) \right], \quad (3)$$

where r_n is the mean radius of the layer and the expansion coefficients are $a_{lm,n} = R(r_n) a_{lm}^{(0)}$ with $a_{lm}^{(0)}$ corresponding to the absence of interaction. The unknown function $R(r)$ describes the spatial correlation between the layers due to the interaction, i.e. how the deformation of the outer layer is transferred to inner layers. Following [2, 3], we calculated the deformation energy ΔE_{SI} for the l th mode and the interaction energy ΔE_I . $R(r)$ is found minimizing the total change of the energy $\Delta E = \Delta E_{SI} + \Delta E_I$ by using the variational principle. If only the $l = 2$ mode is considered, we find have found that the effective surface tension due to interaction is given by Eq. (2). In a more correct approach contributions of all modes should be summed. The effective surface tension due to the interaction becomes $\sigma_{eff} \sim \sqrt{B\kappa/d_0}$, and is independent of l_{max} . Estimations show that the effective surface tension of multilamellar vesicles is given mainly by the bending energy of the outer layer and not by the interaction energy between the layers, as it is believed in the literature. By the same way, a generalization to the case when the membranes in a lamellar droplet have a nonzero surface tension σ was studied. The solution for $R(r)$ can be expressed through the modified Bessel functions and, as illustrated by the graph ($R(r)$ is normalized to $R(R_0)$ and r is in m), contains the above discussed solutions as limiting cases. The parameters used in the calculations are as for a typical ‘‘onion’’ with $R_0 \sim 10^{-6}$ m, $B \sim 10^2$ Jm $^{-3}$, $\kappa \sim 50 k_B T$, and $d_0 \sim 12$ nm [2]. The dependence on different mode numbers $l = 2$ (full line), 3 (dashed line), and 4 (points) is also shown.



by experiments in which the surface characteristics of vesicles are probed. The theoretical description of one of such experiments, the micropipette technique, is currently in progress.

Acknowledgment

This work was supported by the grant VEGA 1/0429/03 from the Scientific Grant Agency of the Slovak Republic.

References

- [1] U. Seifert, *Adv. Phys.* 46 (1997), 13.
- [2] E. van der Linden and J.H.M. Dröge, *Physica A* 193 (1993), 439.
- [3] P.-G. de Gennes, *The Physics of Liquid Crystals*, Oxford University Press, Oxford (1974).
- [4] E. van der Linden, W.T. Hogervorst, and H.N.W. Lekkerkerker, *Langmuir* 12 (1996), 3127.
- [5] M.G. Berni, C.J. Lawrence, and D. Machin, *Adv. Coll. Interface Sci.* 98 (2002), 217-243.

On the fluorescence spectra of naphthazarin

M. SAVKO¹, S. KAŠČÁKOVÁ¹, D. JANCURA¹ AND J. ULIČNÝ¹

¹Katedra biofyziky, Univerzita P. J. Šafárika, Jesenná 5, 041 54 Košice, Slovensko
e-mail: martin@seneca.science.upjs.sk

The aim of our study was to interpret fluorescence spectra of naphthazarin (5,8-dihydroxy naphthaquinon) [1]. In these spectra unexpected fluorescence band at 530 nm has been observed in alcalic environment (pH>9).

To interpret experimental observations and to find probable explanation of that transition, molecular modeling and set of *ab initio* computations on several levels of theory (HF 3-21G, DFT B3LYP 6-31G*) were performed on neutral form of naphthazarin (NZH₂), both its anionic forms (NZH⁻, NZ²⁻) and on all their possible dimers in vacuum and in water and DMSO using implicit (Polarizable Continuum Model – PCM) model of solvent.

The results of computations shows that fluorescence transition at 530 nm is probably due to dimeric form of naphthazarin (its agregates).

References

- [1] J. Danielsson, J. Uličný, A. Laaksonen, *J. Am. Chem. Soc.*, 123 (2000), 9817-9821.
- [2] A. Szabo, N.S. Ostlund, *Modern Quantum Chemistry*, McGraw-Hill, New York(1989)

Antioxidant activity of different natural materials against liposome peroxidation

M. BABINCOVÁ¹, K. SCHRONEROVÁ¹, E. MACHOVÁ² AND P. SOURIVONG³

¹ Department of Biophysics and Chemical Physics, Comenius University, Mlynská dolina F1, 842 48 Bratislava, Slovakia

² Institute of Chemistry, Slovak Academy of Science, Dúbravská cesta 9, 842 38 Bratislava, Slovakia

³ Physics Department, North Dakota University, Grand Fork, USA

The aim of our study was to find out and compare antioxidant capabilities of different natural materials. Sulphoethyl β -(1 \rightarrow 3)-D glucan, biological response modifier isolated from baker's yeast *Saccharomyces cerevisiae* is effective in the therapy of experimental neoplasie, immunosuppressive states and infectious diseases of bacterial, fungal and viral origin. Glucan also revealed free radical scavenging activity [1,2]. For comparison, we also studied scavenging capabilities of α -tocopherol (vitamin E) [3].

In the recent years, considerable interest has been given to study of antioxidant properties of plant materials such as *Scoparia dulcis*. *Scoparia dulcis* (Scrophulariaceae) is a weed widespread in Laos and Vietnam and it is widely used by indigenous people to reduce aches, pains, fever and for detoxication of organism [4]. We also monitored the free radical scavenging capabilities of well-known Chinese plant extract from Ginseng.

We used ultraviolet radiation UVA (320nm-400nm) as a source of free radicals. Liposomes, with certain antioxidant encapsulated, were exposed to UVA which produces mainly singlet oxygen $^1\text{O}_2$ [5]. Lipid peroxidation was monitored by measurement of absorption spectra of conjugated dienes in the wavelength range 215nm – 320nm using UV VIS spectrophotometer. The increase of the absorption at 233 nm was considered as the evidence of the formation of conjugated dienes. Oxidation index was calculated from the ratio of the absorbances $I=A_{233}/A_{215}$ [6].

It was shown that glucan is a possible antioxidant, effective at higher concentrations. In the comparison with α -tocopherol, glucan exhibits lower antioxidant activity, but due to its immunomodulatory properties glucan may be important in the cancer therapy [7].

Significant decrease in the oxidation degree was observed in α -tocopherol within the whole concentration range. This antioxidant ability of tocopherol is determined by its polyfunctional activity caused by two different fragments of its molecule.

Antioxidant capabilities of *Scoparia dulcis* extract are comparable to Ginseng extract. Both plant extracts exhibit strong dose-dependent antioxidant activity, therefore they represent a promising material for biomedical applications.

Acknowledgement

This work was supported by the research grant from the Slovak Grant Agency Vega No 1/9179/02 and by the Grant of Comenius University No. UK/70/2004

References

- [1] M. Babincová, E. Machová, G. Kogan, *Zeitschrift fur Naturforschung*, 54c (1999), 1084-1089.
- [2] E. Tsiapali, S. Whaley, J. Kalbfleisch, H. E. Ensley, I. W. Browder, D. L. Williams, *Free Radicals in Biology and Medicine*, 30 (2001), 393-402.
- [3] M. Babincová, Z. Bačová, E. Machová, G. Kogan, *Journal of Medicinal Food*, 5 (2002), 79-83.
- [4] L. M. Perry, *Medicinal Plants of East and Southeast Asia*, MIT Press, Cambridge 1989.
- [5] Hagen Trommer, Jens Wagner, Heinrich Graener, Reinhard H.M. Neubert, *European Journal of Pharmaceutics and Biopharmaceutics*, 51 (2001), 207-214.
- [6] R. A. Klein, *Biochem. Biophys. Acta*, 210 (1970), 486-489.
- [7] M. Babincová, K. Schronerová, E. Machová, G. Kogan, *10th Bratislava Symposium on saccharides*, Smolenice, 1.9-6.9.2002.

Mathematical analysis of contact stress in a human hip joint

S. KONVIČKOVÁ, M. SOCHOR, J. SÝKORA, M. DANIEL AND T. GOLDMANN

Laboratory of Biomechanics, CTU in Prague, Technická 4, 166 07 Praha 6, Czech republic
e-mail: J.Sykora@sh.cvut.cz

Total replacement of a hip joint is used for substitution of a dysfunctional hip joint. The development of this substitution has been already resolved for many years and nowadays there are a lot of different constructions on the market.

Our target was to compare the mathematical models of the contact pressure with a numerical one and to evaluate the possibility of using the finite element method for modelling the non-bearing parts of the hip joint from the results.

The analytical models are used for determination of the distribution of contact pressures in a physiognomic joint. These models are easier and the determination of distribution of contact pressure is faster. We used these models for getting the contact pressures in the total replacement of hip joint. We were comparing them with a numerical model of total replacement, which creation and calculation is more complicated and difficult, than the analytical one.

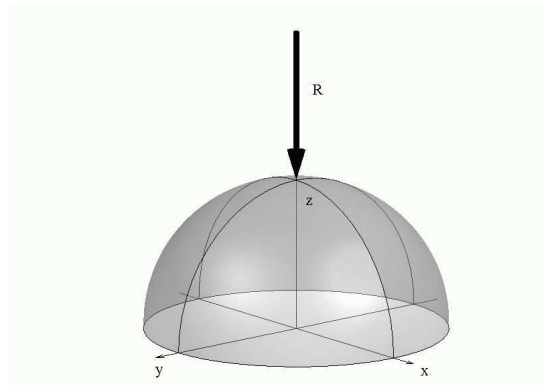


Fig. 1 Model with uniform pressure distribution

Three analytical mathematical models of distribution of contact pressure were compared: a model with uniform pressure distribution (Fig. 1), a model with linear descent pressure in the plane perpendicular to the resultant hip force (Fig. 2) and a model with cosine distribution of contact pressure (Fig. 3) [1, 2, 3].

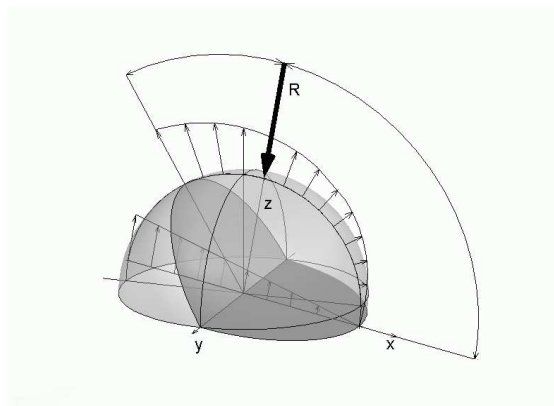


Fig. 2 Model with linear descent pressure in the plane perpendicular to the resultant hip force

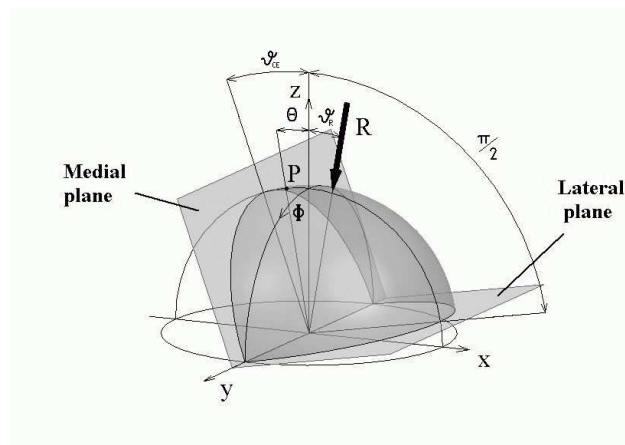


Fig. 3 Model with cosine distribution of contact pressure

These models came out of hemispherical shape of a cup and were weighted by the resulting force in a hip joint. We defined the distribution of a contact pressure from given boundary conditions for each models. On the basis of acquired results we compared all these models to the FEM model of the total hip replacement (Fig. 4).

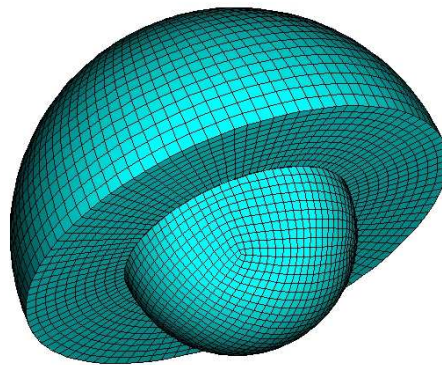


Fig. 4 FEM model

The hemispherical cup and a head in a globe shape created the finite element model. The cup was modelling from the UHMWPE material and for the heads was modelling out of ceramics.

On the basis of acquired values of the distribution of pressure and maximal pressure we analysed the mathematical model with uniform pressure distribution and model with linear descent pressure in the plane perpendicular to the resultant hip force as unsuitable. From the comparison of the FEM models of distribution of the contact pressure on the articular surface with the mathematical model with cosine distribution of contact pressure on the articular surface we found out that both of them are very similar.

From this fact we concluded, that it is possible to use the finite element method for modelling the non-weight bearing part of total replacement of the hip joint.

References

- [1] A. Iglič, V. Kralj-Iglič, M. Daniel, in *Computer methods in biomechanics and biomedical engineering* 5, (2002), 185–192.
- [2] M. Daniel, *Gradient of contact stress as a parameter determining biomechanical status of human hip*, Univerzita Komenského, Fakulta matematiky, fyziky a informatiky, Bratislava (2001), 22 – 46.
- [3] J. Sýkora, *Mathematical analysis of contact stress in a human hip point*, CVUT, Fakulta strojní, Praha (2004), 32 – 60.

Single monomer dynamics in DNA polymers

J. TÓTHOVÁ, B. BRUTOVSKÝ AND V. LISÝ

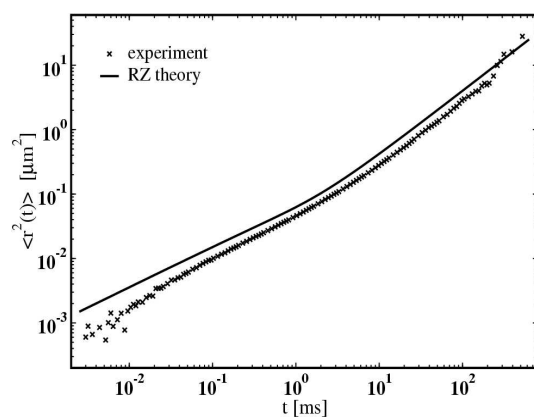
Department of Biophysics, Institute of Physics, P.J. Šafárik University, Jesenná 5, 041 54 Košice, Slovakia
e-mail: tothova@upjs.sk

Fluorescence correlation spectroscopy (FCS) measures the diffusion kinetics of fluorescent species by monitoring the fluctuations in emission intensity in a confocal illumination beam. As fluorescent molecules move in and out of the sampling volume, their fluorescence excitation and thus emission fluctuate: therefore the shape of the autocorrelation function of the fluorescence fluctuations reflects the kinetics of diffusion. Recently, a significant progress has been achieved in the use of the FCS to the study of the dynamics of macromolecules in solution. In the experiments [1], the general features of the internal dynamics of single randomly labeled DNA in aqueous solution were assessed. The work [2] reports the first measurements of the stochastic motion of individual monomers within isolated polymer coils. Single and double stranded DNA (ssDNA and dsDNA) were used as model polymers. A fluorescent label was specifically attached to a single base on the DNA molecules and the motion of the labeled monomer was monitored with the FCS technique. The distinct advantages of FCS over more classical techniques such as the dynamic light and neutron scattering are evident. From the point of view of the interpretation of the experiments, the motion of one specifically tagged monomer is, in theory, much easier to describe than the complex motions of the whole polymer coil. It is also not necessary to calculate the dynamic structure factor depending by a complicated manner on the scattering wave vector. FCS is thus very suitable for testing the theories of polymer dynamics. In [2], the time dependence of the mean square displacement (MSD) of the end monomer has been measured and compared to the Rouse and Zimm models [3]. A good but rather puzzling agreement with the prediction of the Rouse model for the internal dynamics of polymers, $\langle r^2(t) \rangle \sim \sqrt{t}$, has been observed for dsDNA for a wide range of time scales, while in the case of ssDNA the monomer followed the Zimm-type $\sim t^{3/2}$ kinetics, independent on any polymer parameters. The latter regime corresponds to the common view on the dynamics of flexible polymers. The observation of the Rouse behavior for dsDNA was qualitatively related to the semiflexible nature of the macromolecule but appears to be in disagreement with current theories of polymer dynamics. In the present work the FCS experiments [2] are analyzed in detail. We come from the idea that the description of the polymer dynamics necessarily contains model-dependent quantities that should be carefully determined from experiments. Within the Rouse model of flexible polymers, the hydrodynamic radius of the coil ($= Nb$, where N is the number of beads and b the bead radius) is such an unknown parameter. The second phenomenological quantity entering the model is Na^2 (or the gyration radius $R_G = (Na^2/6)^{1/2}$ that can be determined from static scattering experiments). Here, a is the mean square distance between the neighboring beads along the chain, assuming that the equilibrium distribution of the beads is Gaussian. The behavior of the Zimm polymer is governed by only one phenomenological parameter, R_G . The mentioned parameters determine the relaxation times of the polymer internal normal modes, τ_p , $p = 1, 2, \dots$, and the diffusion coefficient of the motion of the coil as a whole, D . An important quantity is the “draining parameter” h that indicates whether the hydrodynamic interaction in solution is strong or not, i.e. whether the dynamics is of the Zimm ($h = 2\sqrt{3N}/\pi b/a \gg 1$) or Rouse type ($h \ll 1$), respectively. We have found that for the parameters used in [2] in the description of the data the parameter h does not obey any of the above conditions, e.g. for dsDNA $h \approx 2.2$ so that the Rouse dynamics cannot be expected for flexible polymers. For this reason we have analyzed the experimental data with no

preliminary assumption concerning the applicability of a specific, Rouse or Zimm, dynamics. In such a “combined” Rouse-Zimm (RZ) description the MSD of the end monomer is

$$\langle r^2(t) \rangle = 6Dt + 4\pi^{-2} Na^2 \sum_{p=1}^{\infty} p^{-2} [1 - \exp(-t/\tau_p)],$$

where $D = D_R + D_Z$ and $1/\tau_p = 1/\tau_{pR} + 1/\tau_{pZ}$ (the indices R and Z stay for the corresponding model) [4, 5]. This equation for the MSD was fitted to the experimental data [2] on dsDNA and ssDNA of various lengths. As distinct from the original treatment [2], the diffusion term is kept in the consideration. Leaving the parameters a and b free (except the natural limitations $Na < L$ and $a > 2b$, where L is the DNA length), it was confirmed by the numerical optimization that the dsDNA data are essentially described by the Rouse model ($h < 1$), however, with model parameters that differ from those used in [2]. We shall not dwell on this case since one cannot assume the studied relatively short dsDNA chains (2400 and 23100 base pairs) to be flexible polymers. An example of the optimization of the MSD to ssDNA data is shown on the figure (6700 bases, $T = 310$ K, the solvent viscosity $\eta = 0.69$ Pa·s, the distance between the bases 0.58 nm). The length of such a DNA is $L = 3886$ nm. If l is the



Kuhn length, by its definition one has to require $Na^2 = Ll$, $N < L/l$, $a > l$, and $b < a/2$. The optimization then yields the following ssDNA parameters for the RZ model: $a \approx 9.15$ nm, $b \approx 4.56$ nm, and $N = 422$. This corresponds to $h \approx 20$ so that the polymer follows essentially the Zimm dynamics (if the pure Zimm regime is assumed from the beginning, the optimization gives slightly different values $N = 414$ and $a \approx 9$ nm). Note that for any set of the model parameters the experimental MSD values are lower than the theoretical ones; this resembles the well-known

long lasting “puzzle” between the Zimm theory and dynamic scattering experiments. At the shortest time scales (several μ s) the discrepancy with the data can be explained by processes related to the internal dynamics of the fluorophore only [2]. A small difference between the theory and experiment that occurs at longer times, up to about 0.1 ms, could be probably attributed to the effects of hydrodynamic memory [5]. This question is currently under consideration.

In conclusion, the two key parameters for the statistical-mechanical description of the universal behavior of polymers in solution are the radius and the persistence length. In this work both the parameters have been determined from the FCS experiments [2]. For the presented results on ssDNA we have found the Kuhn length to be about 9 nm, a surprisingly large value if compared to the values cited in the literature (to our knowledge, from 0.8 to 4 nm). Complementary experiments, such as the static light scattering measurements of R_G , seem to be highly desirable to resolve this problem.

Acknowledgment

We are greatly indebted to O. Krichevsky for providing us with the experimental data. This work was supported by the Marie Curie European Reintegration Grant MERG-CT-2004-506291 within the EC Sixth Framework Programme, and by the grant VEGA 1/0429/03 from the Scientific Grant Agency of the Slovak Republic.

References

- [1] D. Lumma, S. Keller, T. Vilgis, and J.O. Rädler, *Phys. Rev. Lett.* 90 (2003), 218301.
- [2] R. Schusterman, S. Alon, T. Gavrinov, and O. Krichevsky, *Phys. Rev. Lett.* 92 (2004), 048303.
- [3] M. Doi and S.F. Edwards, *The Theory of Polymer Dynamics*, Clarendon Press, Oxford (1986).
- [4] E. Dubois-Violette and P.-G. de Gennes, *Physics* 3 (1967), 181.
- [5] V. Lisy, J. Tothova, and A.V. Zatovsky, *arXiv: cond-mat 0403200* (2004).



**LIST
OF PARTICIPANTS**

LJUBA BACHÁROVÁ
International Laser Centre, Bratislava
bacharova@ilc.sk

MIKULÁŠ BÁNÓ
Department of Biophysics, Institute of Experimental Physics, Slovak Academy of Sciences, Košice
bano@saske.sk

MIRIAM BITTNEROVÁ
Pharmaceutical faculty, Comenius University, Bratislava
bittnerova@fpharm.uniba.sk

BRANISLAV BRUTOVSKÝ
Department of Biophysics, Institute of Physics, Faculty of Science, P.J. Šafárik University, Košice
bru@seneca.science.upjs.sk

MICHAL ČAGALINEC
Department of Biophysics, Faculty of Mathematics, Physics and Informatics, Comenius University, Bratislava
misoc@ilc.sk

JÁN ČARNICKÝ
Department of Biophysics, Faculty of Mathematics, Physics and Informatics, Comenius University, Bratislava
carnicky@ilc.sk

IVAN ČAVARGA
Medical School Hospital of L. Pasteur, Košice

MATEJ DANIEL
Department of Applied Mechanics and Mechatronics, Faculty of Mechanical Engineering, Technical University, Košice
daniel@biomed.fsid.cvut.sk

GABRIELA FABRICOVÁ
Department of Biophysics, Institute of Physics, Faculty of Science, P.J. Šafárik University, Košice
gfabrici@seneca.science.upjs.sk

DIANA FEDUNOVÁ
Department of Biophysics, Institute of Experimental Physics, Slovak Academy of Sciences, Košice
fedunova@saske.sk

JANA GALLOVÁ
Faculty of Pharmacy, Comenius University, Bratislava
gallova@fpharm.uniba.sk

DANA HABODÁSZOVÁ
Department of Biophysics, Faculty of Mathematics, Physics and Informatics, Comenius University, Bratislava
habodaszova@yahoo.com

LIST OF PARTICIPANTS

VALÉRIA HAVRILOVÁ

Department of Biophysics, Institute of Physics, Faculty of Science, P.J. Šafárik University, Košice
havrilv@kosice.upjs.sk

JOZEF HRITZ

Department of Biophysics, Institute of Physics, Faculty of Science, P.J. Šafárik University, Košice
hritz@seneca.science.upjs.sk

DUŠAN CHORVÁT

International Laser Centre, Bratislava
chorvat@ilc.sk

DUŠAN CHORVÁT, JR.

International Laser Centre, Bratislava
dusan@ilc.sk

JÁN JAKUŠ

Institute of Medical Biophysics, Jessenius Faculty of Medicine, Comenius University, Martin
jakus@jfmmed.uniba.sk

DANIEL JANCURA

Department of Biophysics, Institute of Physics, Faculty of Science, P.J. Šafárik University, Košice
djancura@yahoo.com

ZUZANA JURAŠEKOVÁ

Department of Biophysics, Institute of Physics, Faculty of Science, P.J. Šafárik University, Košice
zuzanajpo@pobox.sk

JANKA KARLOVSKÁ

Department of Physical Chemistry of Drugs, Faculty of Pharmacy, Comenius University, Bratislava
karlovska@fpharm.uniba.sk

SLÁVKA KAŠČÁKOVÁ

Department of Biophysics, Institute of Physics, Faculty of Science, P.J. Šafárik University, Košice
kassla00@pobox.sk

PETER KAŠŠÁK

Department of Biophysics, Faculty of Mathematics, Physics and Informatics, Comenius University, Bratislava
p.kassak@bioch.unimaas.nl

JANA KIRCHNEROVÁ

Faculty of Mathematics, Physics and Informatics, Comenius University, Bratislava
kirchnerova@ilc.sk

SILVIA KOČANOVÁ

Department of Biophysics, Institute of Physics, Faculty of Science, P.J. Šafárik University, Košice
kocanova@yahoo.com

MÁRIA KOŽURKOVÁ

Department of Biochemistry, Institute of Chemistry, Faculty of Sciences, P.J. Šafárik University, Košice
kozurkom@kosice.upjs.sk

VLADIMÍR LISÝ

Department of Biophysics, Institute of Physics, Faculty of Science, P.J. Šafárik University, Košice
lisy@upjs.sk

ANTON MATEAŠIK

International Laser Centre, Bratislava
tono@ilc.sk

PAVOL MIŠKOVSKÝ

Department of Biophysics, Institute of Physics, Faculty of Science, P.J. Šafárik University, Košice
misko@kosice.upjs.sk

PETER MUSIL

Faculty of mathematics, physics and informatics, Comenius University, Bratislava
musil@ilc.sk

PAVEL NOVÁK

Institute of Molecular Physiology and Genetics, Slovak Academy of Sciences, Bratislava
pavel.novak@savba.sk

VERONIKA OSTATNÁ

Faculty of Mathematics, Physics and Computer Sciences, Comenius University, Bratislava
ostatna@dmpc.dbp.fmph.uniba.sk

JARMILA PODSKOČOVÁ

Faculty of Mathematics Physics and Informatics, Comenius University, Bratislava
podskocova@ilc.sk

MÁRIA RICHTEROVÁ

Department of Biophysics, Institute of Physics, Faculty of Science, P.J. Šafárik University, Košice
mrichterova@post.sk

MARTIN SAVKO

Department of Biophysics, Institute of Physics, Faculty of Science, P.J. Šafárik University, Košice
martin.savko@post.sk

KRISTÍNA SCHRONEROVÁ

Department of Biophysics and Chemical Physics, Comenius University, Bratislava
schronerova@fmph.uniba.sk.sk

JOZEF SMOLKA

Faculty of Mathematics Physics and Informatics, Comenius University, Bratislava
smolka@ilc.sk

JANA STANIČOVÁ

Department of Chemistry, Biology and Biochemistry, University of Veterinary Medicine, Košice
stanicova@uvm.sk

JAN SÝKORA

Laboratory of Biomechanics, Czech Technical University, Prague, Czech Republic
J.Sykora@sh.cvut.cz

LIST OF PARTICIPANTS

JANA TÓTHOVÁ

Department of Biophysics, Institute of Physics, Faculty of Science, P.J. Šafárik University, Košice
tothova@upjs.sk

JOZEF ULIČNÝ

Department of Biophysics, Institute of Physics, Faculty of Science, P.J. Šafárik University, Košice
ulicny@seneca.science.upjs.sk

ZUZANA VAREČKOVÁ

Institute of Molecular Physiology and Genetics, Slovak Academy of Sciences, Bratislava
zufanka@yahoo.fr

IVAN ZAHRADNÍK

Institute of Molecular Physiology and Genetics, Slovak Academy of Sciences, Bratislava
ivan.zahradnik@savba.sk



AUTHOR INDEX

Adamčík J.	61, 67	Jakuš J.	20
Babincová M.	73	Jancura D.	36, 37, 38, 42, 63, 72
Bachárová L.	27, 33, 46	Jasem P.	61
Bágeřová J.	58	Jurašková Z.	63
Balgavý P.	60, 64	Karlovská J.	64
Bánó M.	22	Kaščáková S.	36, 38, 72
Baťová Z.	56	Kaššák P.	65
Bittnerová M.	56	Kirchnerová J.	25, 27
Bobrov N.	41	Kočanová S.	39
Brezáni P.	41	Kolláriková G.	29
Brutovský B.	76	Komínková V.	43
Cagalinec M.	25, 27	Konvičková S.	48, 50, 74
Čarnický J.	31	Kožurková M.	67
Čavarga I.	41	Kralj-Iglič V.	48, 50
Daniel M.	48, 50, 74	Kyselovič J.	46, 56
Danko P.	67	Laaksonen A.	42
Fabriciová G.	36, 37, 63	Lacík I.	29
Fedoročko P.	41	Lisý V.	70, 76
Fedunová D.	58	Longauer F.	41
Ferko M.	44	Machová E.	73
Gallová J.	60, 64	Marek J.	22
García-Ramos J. V.	37	Mateašik A.	15, 33, 39, 44, 52
Gbur P.	63	Maurizot J. C.	38, 61
Goldmann T.	74	Mirossay L.	39, 41
Habodászová D.	44, 65	Miškovský P.	35, 36, 37, 38, 39, 41, 42, 61, 63
Hanulová M.	60	Musatov A.	54
Havrilová V.	61	Musil P.	46, 56
Hianik T.	69	Novák P.	17
Hritz J.	39, 42	Ondriaš K.	43
Chorvát D.	31	Ostatná V.	69
Chorvát D., Jr.	15, 25, 27, 29, 31, 52	Petrufová A.	39
Chorvátová A.	15, 25, 27	Plášek J.	39
Iglič A.	48, 50	Podhradský D.	67
		Podskočová J.	29
		Poláková E.	19

AUTHOR INDEX

Refregiers M.	38, 61	Štubňa J.	41
Richterová M.	70	Teixeira J.	60
Robinson N.C.	54	Tóthová J.	76
Rybárová S.	41		
		Uhríková D.	60
Sabolová D.	67	Uličný J.	24, 42, 72
Sánchez-Cortés S.	37	Varečková Z.	43
Savko M.	72	Waczulíková I.	44
Schronerová K.	73		
Smolka J.	52	Zahradník I.	17, 19
Sochor M.	74	Zahradníková A.	19
Sourivong P.	73	Zahradníková A., Jr.	19
Staničová J.	54	Ziegelhöffer A.	44
Stupák M.	22	Zimányi M.	33
Sureau F.	38	Zvarík M.	44
Sýkora J.	74		
Šarišský M.	39		
Šikurová L.	44, 65		